



# Saturn's Nightside Dynamics During Cassini's F Ring and Proximal Orbits: Response to Solar Wind and Planetary Period Oscillation Modulations

T. Bradley, S. Cowley, E. Bunce, H. Melin, G. Provan, J. Nichols, M. Dougherty, E. Roussos, N. Krupp, C. Tao, et al.

## ► To cite this version:

T. Bradley, S. Cowley, E. Bunce, H. Melin, G. Provan, et al.. Saturn's Nightside Dynamics During Cassini's F Ring and Proximal Orbits: Response to Solar Wind and Planetary Period Oscillation Modulations. *Journal of Geophysical Research Space Physics*, 2020, 125 (9), 10.1029/2020JA027907 . hal-03238645

**HAL Id: hal-03238645**

**<https://hal.science/hal-03238645>**

Submitted on 3 Jun 2021

**HAL** is a multi-disciplinary open access archive for the deposit and dissemination of scientific research documents, whether they are published or not. The documents may come from teaching and research institutions in France or abroad, or from public or private research centers.

L'archive ouverte pluridisciplinaire **HAL**, est destinée au dépôt et à la diffusion de documents scientifiques de niveau recherche, publiés ou non, émanant des établissements d'enseignement et de recherche français ou étrangers, des laboratoires publics ou privés.



Distributed under a Creative Commons Attribution 4.0 International License

# JGR Space Physics

## RESEARCH ARTICLE

10.1029/2020JA027907

### Key Points:

- We examine data from the final 44 Cassini orbits to investigate the response of Saturn's magnetosphere to concurrent heliospheric conditions
- Compression-related intervals of storm activity and rarefaction-related intervals of quiet are mostly associated with recurrent heliospheric CIRs
- Storm responses are also modulated by the relative phase of the two planetary period oscillation systems with major responses for antiphase

### Supporting Information:

- Supporting Information S1
- Figure S1
- Figure S2
- Figure S3
- Figure S4

### Correspondence to:

T. J. Bradley,  
tb252@le.ac.uk

### Citation:

Bradley, T. J., Cowley, S. W. H., Bunce, E. J., Melin, H., Provan, G., Nichols, J. D., et al. (2020). Saturn's nightside dynamics during Cassini's F ring and proximal orbits: Response to solar wind and planetary period oscillation modulations. *Journal of Geophysical Research: Space Physics*, 125, e2020JA027907. <https://doi.org/10.1029/2020JA027907>

Received 11 FEB 2020





Accepted 3 JUL 2020

Accepted article online 15 JULY 2020

©2020. The Authors.

This is an open access article under the terms of the Creative Commons Attribution License, which permits use, distribution and reproduction in any medium, provided the original work is properly cited.

## Saturn's Nightside Dynamics During Cassini's F Ring and Proximal Orbits: Response to Solar Wind and Planetary Period Oscillation Modulations

T. J. Bradley<sup>1</sup> , S. W. H. Cowley<sup>1</sup> , E. J. Bunce<sup>1</sup> , H. Melin<sup>1</sup> , G. Provan<sup>1</sup> , J. D. Nichols<sup>1</sup> , M. K. Dougherty<sup>2</sup> , E. Roussos<sup>3</sup> , N. Krupp<sup>3</sup> , C. Tao<sup>4,5</sup> , L. Lamy<sup>6</sup> , W. R. Pryor<sup>7</sup> , and G. J. Hunt<sup>2</sup> 

<sup>1</sup>School of Physics and Astronomy, University of Leicester, Leicester, UK, <sup>2</sup>Blackett Laboratory, Imperial College London, London, UK, <sup>3</sup>Max Planck Institute for Solar System Research, Göttingen, Germany, <sup>4</sup>National Institute of Information and Communications Technology, Tokyo, Japan, <sup>5</sup>Department of Geophysics, Tohoku University, Sendai, Japan, <sup>6</sup>LESIA, Observatoire de Paris, Université PSL, CNRS, Sorbonne Université, Université de Paris, Meudon, France, <sup>7</sup>Science Department, Central Arizona College, Coolidge, AZ, USA

**Abstract** We examine the final 44 orbits of the Cassini spacecraft traversing the midnight sector of Saturn's magnetosphere to distances of  $\sim 21$  Saturn radii, to investigate responses to heliospheric conditions inferred from model solar wind and Cassini galactic cosmic ray flux data. Clear storm responses to anticipated magnetospheric compressions are observed in magnetic field and energetic particle data, together with Saturn kilometric radiation (SKR), auroral hiss, and ultraviolet auroral emissions. Most compression events are associated with corotating interaction regions, producing  $\sim 2$ – $3.5$  day intervals of magnetospheric activity that are recurrent with the  $\sim 26$  day solar rotation period (one or two such events per rotation), though one on the final pass is related to a nonrecurrent interplanetary shock possibly associated with an earlier X-class solar flare. The response to compressions is modulated by the concurrent relative phasing of the northern and southern planetary period oscillation (PPO) systems, with long ( $>1$  planetary rotation) SKR low-frequency extension (LFE) intervals associated with strong field-aligned coupling currents being favored when the two PPO systems act together to thin and thicken the tail plasma sheet during each PPO cycle. LFE onsets/intensifications are then favored at thin plasma sheet phases most unstable to reconnection, producing energetic nightside particle injections and poleward contractions of dawn-brightened auroras. Correspondingly, solar rotation recurrent intervals of magnetospheric quiet conditions also occur with weak energetic particle fluxes and auroral emissions, associated with extended solar wind rarefactions. Overall, the results emphasize how strongly activity in Saturn's magnetosphere is modulated by concurrent heliospheric conditions.

## 1. Introduction

This paper is principally concerned with the dynamics in Saturn's magnetic tail observed by the Cassini spacecraft during the final set of Grand Finale F ring and proximal orbits, between December 2016 and September 2017. Research using Cassini data over the past  $\sim 15$  years, together with auroral observations from the Hubble Space Telescope (HST), have shown that dynamical events can broadly be divided into two types. One is driven internally to the magnetosphere and modulated near the planetary rotation period. The other is driven by interaction with the solar wind and modulated at periods related to the solar rotation period, and at sporadic intervals by interplanetary coronal mass ejections (ICMEs). Here we begin by briefly reviewing present understanding of these related topics.

### 1.1. Internally Generated Dynamics in Saturn's Magnetosphere

While it has long been appreciated that the flow in Saturn's magnetosphere is dominated by rotation with the planet driven by coupling to the ionosphere and upper atmosphere (e.g., Badman & Cowley, 2007), results from the Cassini mission have transformed understanding of the consequent dynamics in two major respects. The first is the discovery of a  $\sim 100$  kg s<sup>-1</sup> source of water plasma from the moon Enceladus located deep within the equatorial magnetosphere at a radial distance of  $\sim 4 R_S$  (e.g., Bagenal & Delamere, 2011) ( $R_S$  is Saturn's 1 bar equatorial radius equal to 60,268 km). Associated dynamics are consequently dominated by



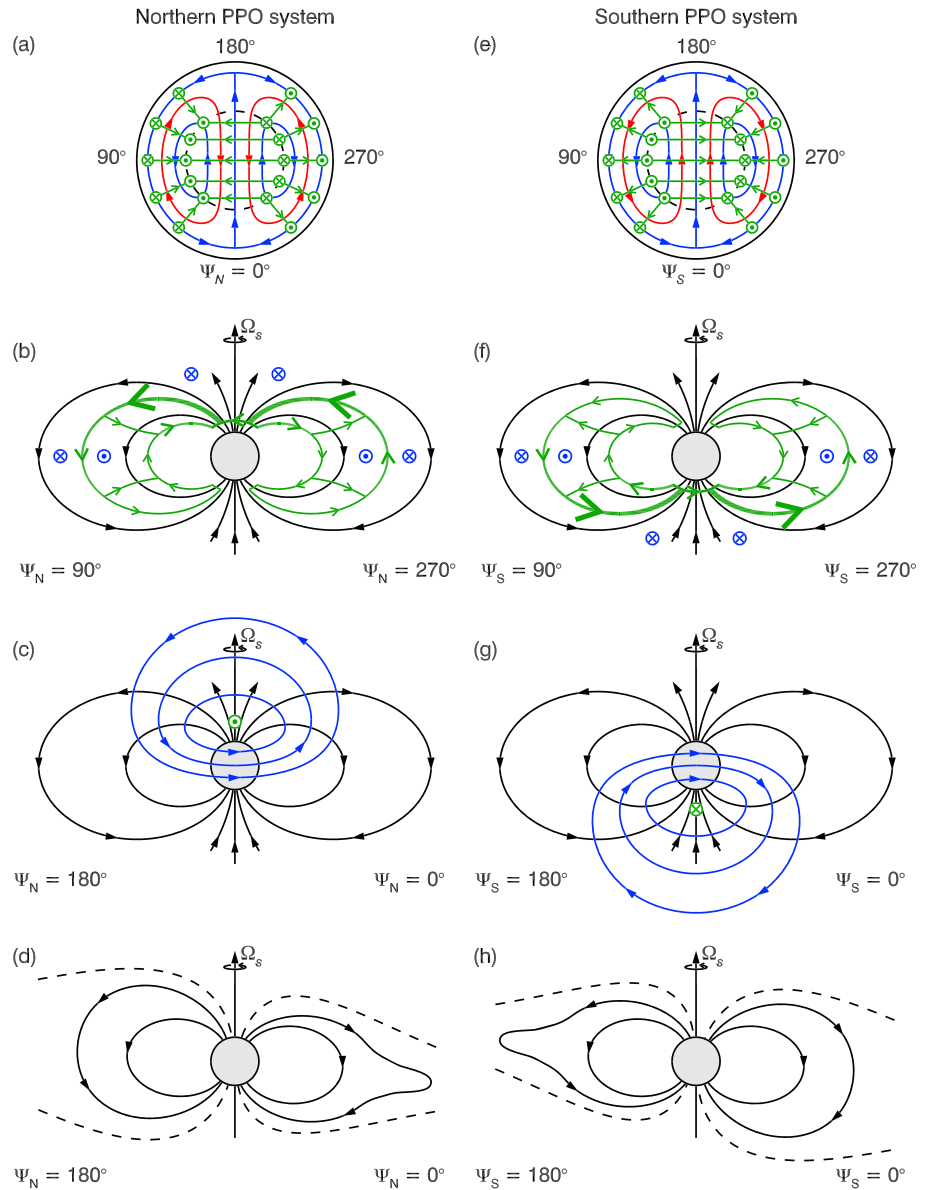


**Figure 1.** Sketches of the magnetic fields and currents associated with the northern (Figures 1a–1d) and southern (Figures 1e–1h) PPO systems, where green arrowed lines and symbols represent electric currents, and blue arrowed lines and symbols the associated perturbation fields. Circled dots and crosses indicate vectors pointing out of and into the plane of the diagram, respectively. Figures 1a and 1e show views of the ionosphere looking down from the north “through” the planet for the southern ionosphere, where the arrowed red lines also indicate the associated ionospheric/atmospheric flow streamlines. Also shown are the phase quantities  $\Psi_{N,S}$  employed to define azimuth with respect to the rotating PPO systems. Figures 1b and 1f show the currents and field perturbations in the  $\Psi_{N,S} = 90 - 270^\circ$  meridian, while Figures 1c and 1g show the field perturbations in the  $\Psi_{N,S} = 0 - 180^\circ$  meridian, where the arrowed black lines indicate the quasi-axisymmetric planetary field on which these perturbations are superposed. Figures 1d and 1h indicate the effect of the PPO field perturbations on the magnetic field in the  $\Psi_{N,S} = 0 - 180^\circ$  meridian plane, where the effects at  $\Psi_{N,S} = 0^\circ$  and  $180^\circ$  drawn for convenience on opposite sides of the planet are intended principally to show the effects at those phases on tail field lines. The arrowed black lines show the perturbed field lines, while the dashed lines indicate the outer boundary of the plasma/current sheet. Adapted from Andrews et al. (2010), Provan et al. (2012), Hunt et al. (2015), and Cowley et al. (2017).

outward radial transport via centrifugally driven flux tube interchange motions (e.g., Azari et al., 2019; Chen et al., 2010; Liu et al., 2010; Liu & Hill, 2012), with subsequent outflow and mass loss occurring downtail via reconnection and plasmoid formation (Cowley et al., 2015; Thomsen et al., 2013; Vasyliunas, 1983).

Frequent downtail propagation of ~5–10 min duration plasmoids have been observed (Hill et al., 2008; Jackman et al., 2008, 2011, 2014; Smith et al., 2016), as well as field dipolarizations with plasma energization and planetward flow lasting for several tens of minutes (Jackman et al., 2015; Smith et al., 2018; Thomsen et al., 2013; Yao et al., 2017), resulting from such “Vasyliunas cycle” reconnection events. Irrespective of whether these events take place in a quasi-steady or time-dependent manner (e.g., Kivelson & Southwood, 2005), however, the basic magnetospheric structure to which this scenario gives rise consists of an inner region where the rotating flux tubes are mass loaded with cool outflowing Enceladus plasma, surrounded by an outer mass-depleted region of residual cool plasma combined with hot plasma energized by the recurrent reconnection events in the tail (Cowley et al., 2004; Thomsen & Coates, 2019). Empirically, this division occurs at a radial distance of ~10  $R_S$  in the equatorial plane (e.g., Kellett et al., 2011), across which the primary flux tube interchange motions are excited (e.g., Thomsen & Coates, 2019).

The second important finding is that the down tail plasma loss by plasmoid release is strongly modulated by the rotating planetary period oscillation (PPOs) systems that are separately driven from the northern and southern polar ionospheres, whose effects are ubiquitously observed in Saturn’s magnetosphere (e.g., Carbary et al., 2018). As discussed in some detail below, these systems give rise to intervals of thickening and thinning of the nightside plasma/current sheet during their rotational cycles, as well as to north-south oscillations (Cowley & Provan, 2017; Cowley et al., 2017; Morooka et al., 2009; Provan et al., 2012), with plasmoids being released preferentially when rotation phases associated with current sheet thinning sweep across the tail (Bradley et al., 2018; Jackman et al., 2016). Correspondingly, PPO-modulated injections of hot plasma into the outer region occur on the nightside, followed by rotation around the planet via dawn, as observed remotely both in energetic neutral atom (ENA) images and auroral emissions at various (ultraviolet (UV), infrared, and radio) wavelengths (Bader, Badman, Cowley et al., 2019; Kinrade et al., 2020; Lamy et al., 2013; Mitchell et al., 2005, 2009).

These injection events are also associated with few-hour enhancements in Saturn kilometric radiation (SKR), an electromagnetic emission usually peaking in the frequency range ~100–400 kHz, generated by the cyclotron maser instability of accelerated auroral electrons (Lamy et al., 2011). In addition to an increase in power, the emission in such events also typically extends to lower frequencies ~10 kHz, forming a “low-frequency extension” (LFE) event (Jackman et al., 2009; Reed et al., 2018). Since SKR is generated in its source region at frequencies very close to the electron cyclotron frequency, proportional to the field strength, an LFE event implies an extension of the source region to higher altitudes along auroral field lines, likely resulting from an intensification of the associated upward directed auroral field-aligned currents. The thinned plasma/current sheet condition for preferential plasmoid release down-tail occurs when the primary PPO-related upward directed field-aligned currents for both northern and southern PPO systems are centered in the dusk/premidnight sector (see Figure 1 introduced in section 1.3 below). This is also the condition for near-minimum SKR emitted power from the primary dawn/prenoon SKR sources in the usual PPO modulation cycle. Maximum power occurs when the PPO-related upward field-aligned currents rotate through half a cycle into the postdawn sector (e.g., Provan et al., 2019). Consequently, these few-hour LFE events, together with their ENA and UV auroral counterparts, generally start and develop during the rising phase of the usual SKR modulation cycle (Jackman et al., 2009; Reed et al., 2018). We note, however, that while clearly modulated by the PPO systems, such dynamic events do not occur during every PPO cycle. The number of independent reconnection episodes in the Smith et al. (2016) catalog of plasmoid and dipolarization events observed in Saturn’s tail, for example, corresponds to one event for every ~1.5 PPO cycles of 10.7 hr (Bradley et al., 2018). However, each such reconnection episode may consist of a sequence (typically ~5) of individual ~5–10 min duration plasmoid/dipolarization events over an interval of ~3 hr.

## 1.2. Solar Wind Generated Dynamics in Saturn’s Magnetosphere

Though most of the dynamical events observed in Saturn’s magnetosphere are thus internally generated and modulated at the planetary (PPO) rotation period as described above, more infrequent but longer-lasting events also occur which are related to the magnetospheric interaction with the solar wind. These were first detected via enhancements in SKR power correlated with the solar wind dynamic pressure observed during approach to Saturn by the Voyager spacecraft in 1980/1981 (Desch, 1982; Desch & Rucker, 1983), thus being modulated on ~26 day solar rotation timescales by the structure of the interplanetary medium. Related

observations made by the Cassini spacecraft during its approach in 2004, combined with UV auroral imaging by the HST, showed that the impact of a recurrent corotating interaction region (CIR) was associated with a brightening and poleward expansion of the dawn auroras reaching almost to the planetary pole (Clarke et al., 2005; Grodent et al., 2005; Kurth et al., 2005). The impact of an ICME was implicated in a related auroral event observed in earlier HST images (Prangé et al., 2004). Subsequent “auroral storm” events have been discussed extensively (e.g., Badman et al., 2016; Clarke et al., 2009; Kurth et al., 2015; Lamy et al., 2018; Meredith et al., 2014; Nichols et al., 2014), while Bunce et al. (2010) have reported Cassini in situ observations of intense field-aligned currents and hot plasma extending near to the planetary pole in the midnight-dawn sector, with further discussion on the same event by Lamy et al. (2010) showing its solar wind-driven nature. Such observations are indicative of compression-induced closure of significant open magnetic flux in Saturn’s tail (Badman et al., 2005; Bunce et al., 2006; Cowley et al., 2005), as is sometimes also observed to occur at Earth (e.g., Boudouridis et al., 2004). Though it is possible that reconnection events associated principally with recurrent Vasyliunas-cycle downtail mass loss continue for some interval after plasmoid release to close some surrounding open tail lobe flux (Jackman et al., 2011), the overall closure of open flux in these events appears to be modest (Jackman et al., 2013; Radioti et al., 2016). The appropriate comparator is the total amount of open flux within the system, typically  $\sim 30$  GWb as determined from the dark area poleward of the typical quiet auroral oval (e.g., Badman et al., 2005), as well as from studies of the poleward limit of hot trapped plasma (Jasinski et al., 2019). The “Dungey cycle” (Dungey, 1961) of open flux production and closure at Saturn then appears broadly divided into two types of interval (Jackman et al., 2004; Badman et al., 2005). During intervals of solar wind rarefaction when the interplanetary magnetic field (IMF) is weak ( $\sim 0.1$  nT or less), open flux is accumulated and lost at low rates, corresponding to reconnection voltages of order tens of kilovolts (flux rates of order tens of kWb per second), though possibly integrating to significant amounts over rarefaction intervals lasting several days. During few-day intervals of solar wind compression associated with CIRs or ICMEs when the IMF is strong ( $\sim 1$  nT), however, open flux may be lost and also accumulated at much greater rates, corresponding to hundreds of kilovolts (hundreds of kWb per second). It is clearly the latter intervals that correspond to the observed auroral storms with longer-lived SKR LFE events, typically lasting for a few Saturn rotations (e.g., Meredith et al., 2014b; Reed et al., 2018). We note that unlike the recurrent shorter-lived (few hour) LFE events, Reed et al. (2018) found no PPO-dependence of the onset of such longer-lived events. As previously reported by Badman et al. (2008), however, they also note that SKR emissions during such intervals may continue to be modulated by the ongoing PPO cycle, possibly indicative of multiple PPO-related activations of enhanced tail reconnection. Although estimates of open flux production rates at Saturn based on interplanetary parameters are somewhat uncertain, considerable evidence has been gathered during the Cassini mission, both from in situ and auroral data, for its frequent occurrence at the dayside magnetopause (Badman et al., 2013, 2014; Fuselier et al., 2014; Jasinski et al., 2014, 2016; Meredith et al., 2014; Radioti et al., 2011; 2013; Sawyer et al., 2019).

By comparison, in situ observations of Saturn’s magnetotail dynamics associated with such solar wind-driven storm intervals have been less well studied to date, one particular reason being that without an upstream monitor, it is difficult to be clear about concurrent solar wind conditions when Cassini is located in the magnetic tail. One such event, however, was observed during the first Cassini outbound pass through Saturn’s magnetotail following orbit insertion in July 2004, Jackman et al. (2005) having shown from inbound and outbound observations outside of the magnetosphere that a recurrent CIR had impinged upon the system while the spacecraft was inside. Observations within the tail included a major enhancement in SKR power with a LFE, an associated injection of hot plasma with ion energies extending to  $>100$  keV, and a dipolarization in the field observed at a radial distance of  $\sim 16.5 R_S$  in the postmidnight sector (Bunce et al., 2005). Thomsen et al. (2015) also presented observations of a  $\sim 5$  hr interval of open tail field reconnection, judged from the relative lack of water ion content in the planetward streaming plasma, that was likely associated with a solar wind compression. Similar water ion-poor conditions indicative of open field reconnection were also found in dipolarization events studied by Smith et al. (2018). No auroral imagery was available for any of these intervals. Another example involving an SKR burst and field dipolarization observed during an auroral storm on the final inbound Cassini pass in September 2017 has, however, been briefly described by Palmaerts et al. (2018). This event also forms part of the present study.

The lack of upstream monitoring may be ameliorated in two ways. The first, as employed by Thomsen et al. (2015), is to use solar wind data obtained from near-Earth orbit to initialize an MHD calculation of

the plasma outflow propagated to Saturn (e.g., Tao et al., 2005; Zieger & Hansen, 2008). Such modeled parameters can be effective in accounting for major structures in the flow and field to within a day or so, provided that the data source and Saturn are in sufficient radial alignment. Second, it has been shown by Roussos, Jackman, et al. (2018) and Roussos, Krupp, et al. (2018) that contemporaneous if relatively low temporal resolution solar wind conditions can be near-continuously discerned from Cassini energetic particle measurements that are sensitive to solar energetic particle (SEP) and galactic cosmic ray (GCRs) fluxes that penetrate deep within Saturn's magnetosphere. Forbush decreases in the GCR flux (Lockwood, 1971) are indicative of the arrival at Saturn of CIR- or ICME-related high field compression regions in the solar wind, while increases in SEPs are indicative of connection to approaching related interplanetary shocks where these particles are energized before streaming out ahead of the shock.

Here we employ both techniques to study the solar wind dependence of dynamical events in Saturn's nightside magnetosphere observed on the final set of F ring and proximal orbits. These data are well-adapted to this study since the orbits lie near continuously on the nightside in the midnight and postmidnight sector, apart from relatively brief periapsis passes on the dayside, consisting of 20 F ring orbits that are closely similar to each other, followed by 23 proximal orbits (including the final inbound half orbit prior to atmospheric entry) that are likewise closely similar to each other. Pass-to-pass differences in the data within each set thus relate specifically to temporal variations in the magnetospheric system associated with dynamics, which we compare with inferred heliospheric conditions. The interval is also reasonably well supported by auroral imagery obtained both by Cassini and by the HST. We also examine these events for PPO-related dependencies. To this end we conclude this introduction with a brief discussion of nightside plasma/current sheet modulations associated with the PPO phenomenon.

### 1.3. PPO Modulations of Saturn's Nightside Plasma/Current Sheet

The physical picture of PPO modulations in Saturn's magnetospheric tail, to which we refer extensively in subsequent sections, is shown in Figure 1, based on observations and modeling presented by Morooka et al. (2009), Carbary et al. (2008), Andrews et al. (2010), Arridge et al. (2011), Provan et al. (2012), Jackman et al. (2016), Thomsen et al. (2017), Cowley et al. (2017), Cowley and Provan (2017), Hunt et al. (2015), and Agiwal et al. (2020). Figures 1a–1d in the left column refer to modulations due to the northern (N) PPO system driven from the northern polar ionosphere, while Figures 1e–1h in the right column refer to modulations due to the southern (S) PPO system driven from the southern polar ionosphere. Figures 1a and 1e show views of the ionosphere looking down from the north, “through” the planet for the southern ionosphere in Figure 1e. These figures also show the phase quantities  $\Psi_{N,S}$  employed to define azimuthal position with respect to these rotating systems. Figures 1b and 1f show the current flows (green) and field perturbations (blue) in the  $\Psi_{N,S} = 90 - 270^\circ$  meridian plane, while Figures 1c and 1g show the field perturbations in the  $\Psi_{N,S} = 0 - 180^\circ$  meridian plane. Red arrowed lines show the sense of the atmospheric/ionospheric flow associated with each current system (Hunt et al., 2014; Jia et al., 2012), while black arrowed lines indicate the near-axisymmetric planetary background magnetic field. We note that the PPO  $\Psi_{N,S} = 0^\circ$  meridians are defined to be those where the near-equatorial quasi-uniform perturbation field in the near-planet region points directly radially outward from the planet.

The black arrowed lines in Figures 1d and 1h show the overall effect of the perturbation fields in the  $\Psi_{N,S} = 0 - 180^\circ$  meridian plane, where the effects represented at  $\Psi_{N,S} = 0^\circ$  and  $180^\circ$  on opposite sides of the planet are principally intended to indicate the PPO-related modulations at those phases on tail field lines. These diagrams first show the displacement of the plasma/current sheet center to the south for  $\Psi_N, S = 0^\circ$  and to the north for  $\Psi_{N,S} = 180^\circ$ , associated with the effect of the radial field components, which vary as  $\cos\Psi_{N,S}$  for both systems. The figures also show thickening of the plasma/current sheet for  $\Psi_N = 180^\circ$  and  $\Psi_S = 0^\circ$ , and thinning of the plasma/current sheet for  $\Psi_N = 0^\circ$  and  $\Psi_S = 180^\circ$ , associated with the effect of the colatitudinal field (positive toward the south near the equator), which varies as  $\cos\Psi_S$  for the southern system (Figure 1g), but as  $-\cos\Psi_N$  for the northern system (Figure 1c). Thickening of the plasma/current sheet is associated with phases for which the PPO fields augment the southward planetary field at the equator, while thinning is associated with phases for which the PPO fields reduce the southward planetary field in this region. In addition, the PPO systems are also associated with radial transport of field and plasma within the magnetosphere, indicated by the associated ionospheric flow streamlines shown by the arrowed red dashed lines in Figures 1a and 1e. Consideration of the meridional flows imposed as these systems rotate

anticlockwise relative to the subcorotating magnetospheric plasma shows that, for example, the largest outward radial displacements occur at  $\Psi_N = 270^\circ$  for the northern system, and at  $\Psi_S = 90^\circ$  for the southern system.

The effects of the two systems are in general simultaneously present in the nightside plasma/current sheet, with comparable amplitudes during the interval examined here, though with modest northern dominance as outlined in section 2.3.1. The resulting overall modulation thus depends on the relative rotation phase of the two PPO systems (the “beat phase”). Figures 1d and 1h show that the north-south oscillations will be maximized when the two systems are in phase (beat phase  $0^\circ/360^\circ$ ), while the thickening-thinning effect will then be minimized, since the radial perturbation fields of the two systems will be in phase while the colatitudinal fields will be in antiphase. Conversely, the thickening-thinning effect (and the radial displacement effect) will be maximized when the two systems are in antiphase (beat phase  $180^\circ$ ), while the north-south oscillations will be minimized, since the colatitudinal perturbation fields of the two systems will then be in phase while the radial fields will be in antiphase. Since we may expect reconnection to be favored at phases corresponding to thin current sheets with weakened southward directed fields, it is under the latter antiphase conditions that we may expect the greatest PPO modulation of reconnection in the tail current sheet, that is, at phases of  $\sim 0^\circ/360^\circ$  for the northern system and  $\sim 180^\circ$  for the southern system, consistent with the results of Bradley et al. (2018) for the dominantly short-lived plasmoid/dipolarization events in the tail.

## 2. Data Set

In this study we combine examination of magnetic field, charged particle, radio emission, auroral UV, and model data to identify intervals of solar wind-related tail dynamics at Saturn, observed during the final set of Cassini orbits. In section 2.1 we introduce the interval employed and the properties of the Cassini orbit that determine the nature of the in situ data. In section 2.2 we then describe the instrument data sets and the purpose for which they are employed, while in section 2.3 we similarly describe the model data sets. Section 2.4 then discusses the concurrent heliospheric conditions inferred from the model solar wind/IMF data combined with the Cassini GCR/SEP data.

### 2.1. Interval of Study

Data from two main intervals are studied here. The first corresponds to the Cassini F ring orbits, revolutions (Revs) 251–270, starting on 1 December 2016 (Day 336 of 2016 or Day 4,718 in doy2004) and ending on 23 April 2017 (Day 113 of 2017 or Day 4,861 in doy2004), though we also examine data from Rev 250, similar to the F ring orbits, occurring immediately prior to this interval. The second corresponds to the proximal orbits (Revs 271–293), starting on 23 April 2017, and ending on 15 September 2017 (Day 258 of 2017 or Day 5,006 in doy2004). Doy2004 is employed as a convenient time parameter for multiyear data sets and is defined such that  $t = 0$  corresponds to 00 UT on 1 January 2004, effectively the start of the Cassini science mission. The trajectories of these Revs are plotted in Figure 2 in Krono-Graphic Stationary (KGS) coordinates, in which  $Z$  is Saturn’s spin/magnetic axis positive to the north, the  $X$ - $Z$  plane contains the Sun (toward positive  $X$ ), and  $Y$  completes the right-hand triad pointing toward dusk. Figure 2a shows the  $Y$ - $X$  plane viewed from the north, Figure 2b the  $Z$ - $X$  plane viewed from dawn, and Figure 2c the  $Z$ - $Y$  plane viewed from the Sun. The trajectories are color coded by Rev as shown at the top of the figure, with Rev numbers employed here following the usual Cassini mission scheme defined from apoapsis to apoapsis.

The F ring Revs consist of 20 highly inclined orbits of Saturn (inclination  $\sim 63.5^\circ$ ) with periods of  $\sim 7.1$  days, that dive at periapsis past the outer edge of Saturn’s rings at  $\sim 2.5 R_S$  on the dayside of the planet, with apoapsis at  $\sim 21 R_S$  on the nightside (Figures 2a and 2b). Apoapsides are confined in local time (LT) to near  $\sim 2$  hr LT in the postmidnight sector, located  $\sim 3 R_S$  north of the equatorial plane. The proximal Revs consist of 22.5 similarly highly inclined orbits (inclination  $\sim 61.8^\circ$ ) with a period of  $\sim 6.7$  days, though with the orbit near periapsis now crossing between the inner edge of the D-ring and Saturn’s upper atmosphere at a radial distance of a little over  $1 R_S$ , culminating with the end of the Cassini mission in Saturn’s dayside upper atmosphere on Rev 293. The proximal orbits are thus similar to the F ring orbits, though with a few differences. Most importantly, while the apoapsides are nearly at the same radial distance throughout, and with a similar northward displacement from the equatorial plane, the orbit ellipse is more eccentric for the proximal orbits



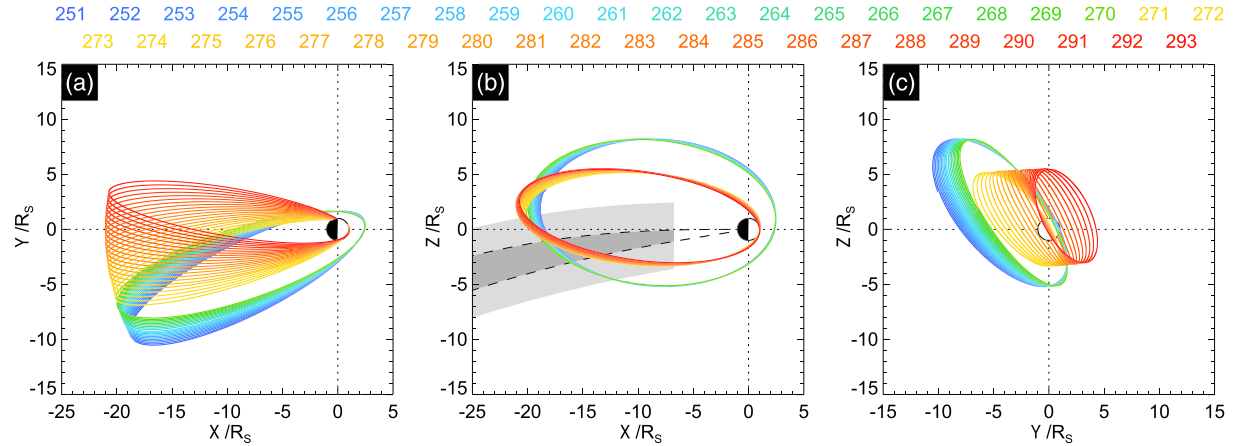


**Figure 2.** Plot of the Cassini trajectory during the F ring and proximal orbits (1 December 2016 to 15 September 2017) in KGS coordinates. Figure 2a shows the trajectory projected into the X-Y plane looking along Saturn's spin/magnetic axis from the north, Figure 2b shows the X-Z plane viewed from dawn toward dusk, while Figure 2c shows the Y-Z plane viewed from the Sun toward Saturn. Unit distances in each figure are given in  $R_S$ . Individual revs are color coded according to the scheme shown above the panels, with the F ring orbits (Revs 251–270) colored blue to green, and the proximal orbits (Revs 271–293) colored yellow to red. In Figure 2b the dark-gray-shaded region bordered by black dashed lines shows the expected location of the center of the tail current sheet according to the Arridge et al. (2008) model, where the southern and northern dashed lines correspond to limiting model hinging distances of 20 and 30  $R_S$ , respectively. The lighter-gray-shaded regions extend 2.5  $R_S$  either side of these central locations, giving an indication of the thickness of the current sheet.

than for the F ring orbits, such that Cassini is in general located closer to the nightside equatorial plane where it is more sensitive to variations in the thickness of the plasma/current sheet. We also note the greater rate of change of the LT of apoapsis during the proximal orbits, with that for Rev 271 being at  $\sim 2$  hr LT in the morning sector, similar to the F ring orbits, decreasing over successive orbits to a final apoapsis LT of  $\sim 23$  hr premidnight for Rev 293.

In Figure 2b the Arridge et al. (2008) bowl model of the center of Saturn's current sheet is plotted for the noon-midnight meridian using the equation

$$Z_{CS} = \left[ \rho - r_H \tanh\left(\frac{\rho}{r_H}\right) \right] \tan\theta_{SUN}, \quad (1)$$

in which  $Z_{CS}$  is the position of the center of the current sheet (where  $B_r$  changes sign) northward of the equatorial plane (for  $Z_{CS}$  positive),  $\rho$  is the cylindrical radial distance from Saturn's spin/magnetic axis,  $r_H$  is the characteristic hinging distance of the current sheet, and  $\theta_{SUN}$  is the latitude of the solar wind flow, taken to be the negative of the latitude of the Sun. All units of distance are given in  $R_S$ . Northern solstice occurred on 24 May 2017 during our study interval (Day 114 of 2017 or Day 4,862 doy2004), such that the latitude of the Sun is nearly fixed at its maximum value  $\sim 26.5^\circ$  throughout the interval considered here (taken to be constant in the plot). Fits to data in prior studies have provided varying estimates of the hinging distance of 16 and 29  $R_S$  in Arridge et al. (2008) and  $\sim 27 \pm 6 R_S$  in Carbary et al. (2015). Here we take illustrative  $r_H$  values of 20  $R_S$ , shown by the southernmost black dashed line in Figure 2b, and 30  $R_S$  shown by the northernmost black dashed line, with the region between being shaded dark gray. The lighter-gray-shaded regions extend 2.5  $R_S$  north and south of the darker-shaded region, giving an initial indication of the region where Cassini may be expected to encounter the tail plasma/current sheet. Due to the northward displacement of apoapsis, combined with the southward seasonal displacement of the plasma/current sheet, in all cases the spacecraft is expected to be located closer to the center of the plasma sheet on its southern outbound passes than on its northern inbound passes, crossing through the sheet center outbound  $\sim 2 R_S$  southward of the planetary equatorial plane at a radial distance from Saturn of  $\sim 17 R_S$ . Of course, this picture of the current sheet and its location should be considered only as a rough guide, given the PPO-related north-south oscillations and thickening and thinning effect discussed in section 1 (Figure 1).

Overall, we thus examine data from 43.5 Cassini Revs over an interval of  $\sim 9.5$  months. As will be discussed in section 2.3, during this interval the northern PPO period was near fixed at  $\sim 10.79$  hr while the southern



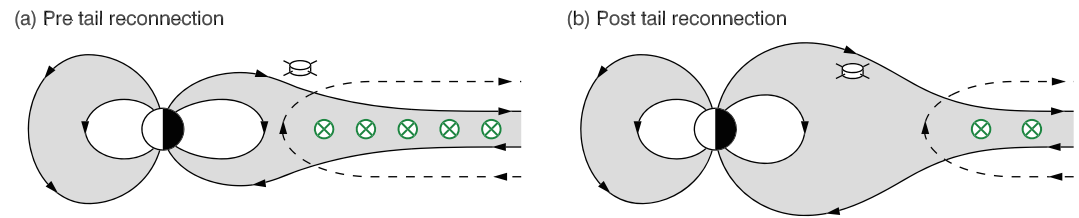


**Figure 3.** Diagram (not to scale) of the expected response of Saturn's magnetic field close to the planet following tail reconnection. Figure 3a shows a meridional cross section of Saturn's magnetosphere near the noon-midnight meridian, with noon on the left and midnight on the right. The total magnetic field is shown by black arrowed lines with gray-shaded areas indicating regions of hot plasma. The circled green crosses indicate Saturn's tail current sheet, flowing into the page, with the associated magnetic perturbation field shown via arrowed black dashed lines. Following tail reconnection the current sheet and perturbation field effectively contracts tailward as shown in Figure 3b, such that the field assumes a more dipolar form in the inner part of the system, while the hot plasma region expands outward.

period was likewise near fixed at  $\sim 10.68$  hr (Provan et al., 2018). These periods imply a PPO beat period of  $\sim 42.5$  days, such that the overall interval corresponds to  $\sim 7$  cycles of beat phase. Similarly, at the solar rotation period of  $\sim 26$  days the interval also corresponds to  $\sim 11$  cycles of periodic solar wind conditions, to which additional nonrecurrent (e.g., ICME) events may be added. Brief examination then shows that the difference between the beat period and the solar rotation period, or near multiples thereof, is such that a broad range of relative phase conditions occurs between the PPO beat cycle and the solar rotation cycle over the data set as a whole, upon which the natural variability of the heliospheric medium is also superposed. Consequently, the interval allows the study of the response to a significant number of solar wind compression events over a range of PPO conditions, thus allowing examination of the influences of both.

## 2.2. Instrument Data Sets

In this section we provide relevant details of each of the data sets used in this study, together with the purpose for which they are employed.

### 2.2.1. MAG

Magnetic field data from the Cassini MAG instrument (Dougherty et al., 2004) are first employed to detect the onset of solar wind compressions in Saturn's magnetic tail through rapid enhancements in the field strength, combined with deflections in the field direction away from the planetary equatorial plane toward the direction of the solar wind flow. In effect, increases in solar wind dynamic pressure result in decreases in the hinging distance  $r_H$  in Equation 1, such that the tail field deflects toward the solar wind direction at increasingly small radial distances downtail (Figure 2b).

Second, previous studies discussed in section 1 (e.g., Smith et al., 2016, 2018; Thomsen et al., 2013, 2015) have shown that in situ signatures of tail reconnection may be also be identified, usually combined with hot plasma signatures (section 2.2.2 below). Dipolarizations are marked by a southward deflection of the field, associated with an increase in the colatitudinal component, generally combined with a reduction in the radial component. By contrast, plasmoids are marked by small southward deflections of the field followed by larger northward deflections. The associated tail X-line has been suggested to be formed at highly variable radial distances between  $\sim 20$  and  $\sim 70 R_S$ . Thus, with the apoapsis of Cassini being at  $\sim 21 R_S$  during the interval (Figure 2), close to the minimum value, the principal signatures of reconnection are expected to be dipolarization events rather than plasmoids.

In Figure 3 we show a diagram of the near-planet magnetic field response to dipolarizations, where Figure 3a shows a meridional cross section of Saturn's nightside magnetotail before reconnection, while Figure 3b) shows the same region after reconnection. Following tail reconnection occurring at larger distances, tail field lines collapse toward the planet, reducing the tail current and perturbation field such that the field in the inner tail becomes more dipolar in form. For a spacecraft located northward of the current sheet in Figure 3a, and near stationary in position on the timescale of the field reconfiguration, the dipolarization will be seen as an increase in the colatitudinal field ( $B_\theta$ ), positive southward, and a reduction in the radial field ( $B_r$ ). In addition, if the spacecraft is sufficiently close to the equatorial plane it may also become

engulfed in hot plasma as shown in Figure 3b, as the plasma sheet expands north-south away from the equatorial region. This will cause further reduction in the radial field as the spacecraft enters the current sheet, together with the appearance of high-frequency field fluctuations, absent in the tail lobes, associated with the presence of hot plasma.

### 2.2.2. MIMI/LEMMS

Following tail reconnection, hot plasma is accelerated inward toward Saturn forming a dipolarization front as sketched in Figure 3, causing the plasma sheet to expand away from the equator in the near-planet tail. Given an appropriate spacecraft location, such plasma injections are readily observed using the energetic particle detection capabilities of the Cassini Low Energy Magnetospheric Measuring System (LEMMS) of the Magnetospheric Imaging Instrument (MIMI), full details of which are presented by Krimigis et al. (2004) and Armstrong et al. (2009). Here we use LEMMS channels A1–A5 which detect protons of energy 35–56 keV (A1), 56–106 keV (A2), 106–255 keV (A3), 255–506 keV (A4), and 506–805 keV (A5). We note that although these channels also detect heavier ions at energy ranges given by Armstrong et al. (2009), they are typically dominated by protons in the energy ranges specified above (Kotova et al., 2015). We also use channels E0–E4 which detect electrons with energies of 110–365 keV (E0), 220–485 keV (E1), 340–1,350 keV (E2), 600–4,950 keV (E3), and 790–4,750 keV (E4). The typical time resolution of these data is ~5.3 s, though this can increase or decrease during some specific intervals. The fluxes in these channels in general correspond to the high-energy tail of the thermal distribution (observations of which are not available due to prior malfunction of the Cassini low-energy plasma instrument), showing significant increases on entering the plasma sheet from near background levels in the open tail lobes. Dynamical events are thus detected, while the relative flux observed from Rev to Rev also gives an overall indication of the magnetospheric state in terms of its hot plasma population.

As indicated in section 1.2, data from MIMI/LEMMS can also be used to provide an indication of solar wind conditions external to Saturn's magnetosphere even when the spacecraft is located inside (Roussos, Jackman, et al., 2018). Background noise in various LEMMS channels can be used, under appropriate conditions and with appropriate filtering, to provide a measure of the GCR flux. These GCRs are predominantly protons with energies in the range from several hundred MeV to 1 GeV, from sources external to the heliosphere. Regions of compressed magnetic field in the heliosphere repel the GCRs, such that the passing of both CIRs and ICMEs cause sharp decreases in flux followed by a slow recovery over several days. Such Forbush decreases thus provide evidence of the passage of high-field compression regions in the solar wind. Here we use 6-hr averaged counts from channel E6, which while designed to detect 1.6–21 MeV electrons, also has a response to >120 MeV protons. By filtering the data, removing the significant enhancements observed during the short intervals when Cassini crosses Saturn's radiation belts and other instrument effects, these high-energy protons can be isolated to provide a measure of the GCR proton flux (Roussos et al., 2019).

The LEMMS instrument can also observe SEPs in its P2–P9 channels, which detect ~2 to >60 MeV protons that readily penetrate Saturn's magnetosphere. As indicated in section 1, SEPs are shock-accelerated particles magnetically connected with a CIR or ICME (e.g., Cane et al., 1988), and when observed together with a Forbush decrease can also provide evidence of the passage of a compression region in the solar wind. The P2–P8 channels are also found to exhibit a weak response to GCRs, onto which profile transient SEP events are superposed. Here we employ data from the P2 channel sensitive to ~2.3–4.5 MeV protons, which have again been 6-hr averaged and filtered following the same procedure as for channel E6.

### 2.2.3. RPWS

The Cassini Radio and Plasma Wave Science (RPWS) electric field instrument (Gurnett et al., 2004) allows measurement of radio emissions over a wide frequency range in the vicinity of Saturn, which include the spectral ranges of SKR and auroral hiss. SKR is generated via cyclotron maser instability on field lines above the aurora, forming beamed radio emissions excited by energetic auroral electrons (Treumann, 2006; Lamy et al., 2010, 2011). It is emitted close to the local electron cyclotron frequency, with a typical frequency range overall between ~3 kHz and ~1.2 MHz, peaking in intensity roughly between 100 and 400 kHz (Kaiser & Desch, 1984; Lamy, 2017). Northern sources of SKR are observable from latitudes typically northward of  $-20^\circ$ , while southern sources of SKR are observable from latitudes southward of  $+20^\circ$ . Both northern and southern sources are thus simultaneously observable in the equatorial region between  $-20^\circ$  and  $+20^\circ$ . On the F ring orbits the northern sources will thus be observable everywhere except within  $\sim 12 R_S$  of Saturn during the southern outbound portion of the orbit, while southern sources will be observable everywhere except

within  $\sim 18 R_S$  of Saturn during the northern inbound portion of the orbit. Thus, sources of SKR from both hemispheres will be observable through much of the  $\sim 7.1$  day F ring orbits, except for  $\sim 40$  hr prior to periapsis during which only northern sources will be observable, and  $\sim 20$  hr after periapsis during which only southern sources will be observable. For the proximal orbits northern sources will be observable everywhere except within  $\sim 10 R_S$  during the outbound portion of the orbit, while southern sources will be observable everywhere except within  $\sim 15 R_S$  during the inbound portion of the orbit. Thus, both sources will again be visible over most of the  $\sim 6.7$  day orbits, except for  $\sim 30$  hr prior to periapsis during which only northern sources will be observable, and  $\sim 15$  hr after periapsis during which only southern sources will be observable.

With their connection to auroral field-aligned currents and associated electron acceleration, SKR emissions are intimately connected with Saturn's magnetospheric dynamics. On the longest timescales the intensity of the northern and southern emissions vary with Saturn's seasons, with brighter emissions occurring in the summer hemisphere (Nakamura et al., 2019), while on shorter timescales they are modulated at the same periods as their magnetic PPO and auroral UV counterparts (e.g., Gurnett et al., 2009; Provan, Cowley, et al., 2019; Provan et al., 2019), associated with the rotation of the PPO field-aligned current systems shown in Figure 1. As outlined in section 1, these emissions also exhibit sudden intensifications and LFEs indicative of enhancements in auroral field-aligned current intensity that are related to tail dynamics and reconnection (e.g., Jackman et al., 2009; Reed et al., 2018). These may be divided into shorter few-hour LFE events that are PPO-modulated and related to Vasyliunas-cycle reconnection and downtail mass loss, and longer typically few Saturn rotation events, observed following the arrival of dynamic pressure fronts at Saturn's orbit, that are related to Dungey cycle tail reconnection and open flux closure. Here we employ such longer-lived SKR LFE events as indicators of Dungey cycle tail dynamics at Saturn, which will be employed together with in situ field and particle measurements as described above, as well as with UV auroral images when available.

Auroral hiss is a whistler mode emission frequently observed in Saturn's magnetosphere, which is generated by upward moving field-aligned electron beams, that is, downward FAC (Kopf et al., 2010). The emissions occur at frequencies  $\sim 10$ – $100$  Hz, cut off at the electron plasma frequency. The presence of auroral hiss is commonly found on high latitude magnetic field lines (Gurnett et al., 2010; Menietti et al., 2020), generated in the downward current region associated with subcorotating flow poleward of the auroral oval (e.g., Cowley et al., 2004; Hunt et al., 2015). It has thus been found to be a suitable indicator of the open-closed field line boundary, with weaker emissions occurring on closed field lines (Jinks et al., 2014). Immersion in dipolarized newly closed field lines as depicted in Figure 3b, for example, is then expected to be accompanied by a decrease in auroral hiss emission power, indicative of recent tail reconnection.

#### 2.2.4. UVIS

The Ultraviolet Imaging Spectrograph (UVIS) data set employed here uses the far ultraviolet (FUV) channel of the instrument consisting of  $64$  spatial  $\times$   $1,024$  spectral pixels, providing observing in the range  $110$ – $190$  nm. The detector slews over portions of Saturn with the rotation of the spacecraft, providing a two-dimensional pseudo-image of the area covered. Depending on the distance of Cassini from Saturn's poles, multiple sweeps are occasionally necessary to complete a fully mapped image of Saturn's aurora. Mapping of the information from each pixel is achieved using Cassini SPICE pointing information from the NAIF Planetary Data System by projecting the data onto an ellipsoid  $1,100$  km above Saturn's 1 bar level, the altitude at which auroral emissions peak in intensity (Gérard et al., 2009). To obtain the total intensity of the unabsorbed  $H_2$  spectrum over the whole UV wavelength range, intensities over the unabsorbed range  $155$ – $162$  nm are multiplied by a factor of  $8.1$  (Gustin et al., 2016; Gustin et al., 2017).

To remove dayglow we follow the approach of Bader, Badman, Yao et al. (2019), where for each pseudo-image the solar zenith angle (SZA) is determined for each pixel in the mapping grid with a colatitude greater than  $23^\circ$  (away from the main auroral oval). The brightness values and SZAs are also taken for pseudo-images  $3$  hr either side of the original image where available. All brightness values are then median averaged as a function of SZA across  $10^\circ$  wide bins to determine a smoothed SZA-dependent dayglow profile, and this profile is then subtracted from the image, leaving only the auroral emissions.

#### 2.2.5. HST

During this interval of study, the HST obtained 24 time-tagged  $\sim 44$  min exposures of Saturn's northern hemisphere FUV auroras using the Space Telescope Imaging Spectrograph (STIS) instrument, scheduled to match intervals when Cassini was expected to probe the auroral regions (Lamy et al., 2018). The STIS

F25SrF<sub>2</sub> filter employed has a central wavelength of 145.2 nm with a full width at half maximum of 28 nm, rejecting the hydrogen Lyman- $\alpha$  line, though including the H<sub>2</sub> Lyman and Werner bands. The time-tag mode enables tracking of dynamics at shorter timescales than the exposure, though all images shown here have been integrated over the full exposure duration to reduce noise. The dynamics considered here are expected to evolve over timescales of typically a few hours, such that we do not expect to lose significant information by integrating over the full exposures ( $\sim 7\%$  of a planetary/PPO rotation period). Processing of the images follows the usual pipeline, including flat-fielding and geometric correction (e.g., Clarke et al., 2009; Nichols et al., 2009), after which nonauroral emissions are removed following methods outlined by Clarke et al. (2009). As for the UVIS pseudo-images (section 2.2.4), the auroral emissions are then projected onto a latitude/longitude grid at an altitude of 1,100 km.

### 2.3. Model Data Sets

#### 2.3.1. PPO Phase Data

As discussed in section 1.3 and illustrated in Figure 1, PPO phase is a significant factor when considering Saturn's tail dynamics. The global phases  $\Phi_{N,S}$  give the orientation of each PPO system relative to the noon meridian, taken positive in the sense of planetary rotation, while the local phases  $\Psi_{N,S}$  refer to the azimuthal position relative to the northern and southern PPO systems, derived from the global phases and the azimuth of the spacecraft. The local phases in the near-planet regime are thus given by

$$\Psi_{N,S}(t, \varphi) = \Phi_{N,S}(t) - \varphi, \quad (2a)$$

where  $\varphi$  is the azimuth of the spacecraft similarly measured from noon, positive in the sense of planetary rotation. Beyond a radial distance of 12  $R_S$ , however, we also introduce a radial propagation delay of the PPO phase away from the planet, so that

$$\Psi_{N,S}(t, r, \varphi) = \Phi_{N,S}(t) - \varphi - G(r - 12), \quad (2b)$$

with  $r$  in  $R_S$  and gradient  $G$  in  $\text{deg } R_S^{-1}$ . Following the studies of Arridge et al. (2011), Provan et al. (2012), and Bradley et al. (2018), here we take  $G$  equal to  $3^\circ R_S^{-1}$ . We note that because the data employed here were obtained predominantly near the midnight meridian, or a little later in LT (Figure 2a), the local and global PPO phases are generally connected by  $\Psi_{N,S} \approx \Phi_{N,S} - 180^\circ$ . In principle we could therefore discuss the PPO dependency of the data in terms of either the local or global phases. However, it seems most fruitful physically to discuss the data in terms of the local phases determining local conditions in the plasma sheet as the rotating PPO systems sweep across the tail, such that we employ the local phases for purposes of such discussion throughout this paper. We note in particular that Bradley et al. (2018) have shown that observations of reconnection signatures in Saturn's tail are best organized by the local rather than the global PPO phases, it being recalled from section 1.3 and Figure 1 that the optimum conditions for local thinning of the plasma sheet conducive to reconnection are  $\Psi_N \approx 0^\circ$  and  $\Psi_S \approx 180^\circ$ .

As also discussed in section 1.3, the relative phases of the two systems, that is, the beat phase, is also important for tail dynamics, particularly during intervals such as this where the amplitudes are similar (see below), determining whether the two PPO systems act together constructively or destructively. The beat phase, which of course does not depend on the position of the spacecraft, is defined as

$$\Delta\Phi = \Psi_N - \Psi_S = \Phi_N - \Phi_S, \quad (3)$$

where values  $\Delta\Phi = 0^\circ$  (modulo  $360^\circ$ ) correspond to PPO in phase conditions, and  $\Delta\Phi = 180^\circ$  to antiphase. As indicated above, with regard to plasma sheet thickening and thinning related to reconnection, the two systems act in concert for antiphase conditions, and oppositely for in phase conditions.

The global phases  $\Phi_{N,S}$  employed here, from which the local phases are calculated using spacecraft position data, are those derived by Provan et al. (2018) from analysis of oscillations observed in near-apoapsis F ring and proximal orbit data north and south of the equator. The PPO rotation periods were shown to be near-constant over the interval, with a period of 10.792 hr for the northern system and 10.679 hr for the southern system. The global phases  $\Phi_{N,S}$  thus increase linearly with time at a rate given by these periods, with the southern phase increasing more rapidly than the northern phase, such that the beat phase

defined by Equation 3 decreases linearly with time with a beat period of  $\sim 42.5$  days ( $\sim 6$  Cassini Revs), with  $\sim 6.9$  beat cycles over the study interval.

The ratio of the amplitudes of the two PPO systems is also relevant (section 1.3), denoted by  $k$ , the northern amplitude divided by the southern amplitude. This ratio is variable over the Cassini mission, from southern dominance ( $k < 1$ ) early in the mission during late southern summer (equinox in August 2009), to northern dominance ( $k > 1$ ) during the northern summer interval studied here. During the F ring orbits Hunt et al. (2018) found  $k$  to be  $\sim 1.3$ , while Provan et al. (2018) and Provan, Lamy, et al. (2019) found values of  $\sim 1.4$  and  $\sim 1.25$  from analysis of near-apoapsis and near-periapsis proximal orbit data, respectively. These results thus indicate relatively weak northern dominance in the near-equatorial plasma sheet region, with northern system modulations more important than southern, but not by a large factor. The  $k \sim 1$  condition also implies that beat phase modulation of the plasma sheet will be strong during the interval, with large modulations occurring when the two systems act in concert, and near-cancellation when they act oppositely.

### 2.3.2. Model Solar Wind Parameters

In addition to the information obtained from GCR and SEP fluxes, solar wind conditions can also be estimated from magnetohydrodynamic (MHD) modeling using upstream data as input. Solar wind parameters are numerically propagated to Saturn as an ideal MHD fluid affected by solar gravity in a one-dimensional spherically symmetric coordinate system (Tao et al., 2005). Inputs during the interval are given by near-Earth in situ solar wind observations provided by the Operating Missions as a Node on the Internet (OMNI) data set, and by Stereo-A measurements near 1 AU but widely separated from Earth, with a separation angle of  $\sim 150^\circ$  at the start of our interval and  $\sim 128^\circ$  at the end. Uncertainties principally depend on the angular separation relative to the Sun between the source of data and Saturn, and have been investigated in some detail using results from a similar 1-D MHD model by Zieger and Hansen (2008). This study showed that prediction is significantly better during intervals with larger solar wind recurrence indices, these being the correlation coefficients between hourly solar wind speed data over successive solar rotation periods. High recurrence indices are typically found in the late declining phase of the solar cycle, such as the interval studied here. For such data significant prediction efficiencies, for example, the solar wind velocity extend to separation angles of at least  $\sim 90^\circ$  either side of opposition, with uncertainties in the timing of dynamic pressure fronts then being typically less than  $\pm 35$  hr (see further discussion by Lamy et al. (2018)).

### 2.4. Overview of Heliospheric Conditions

Figure 4 provides an overview of the heliospheric conditions during our study interval, as indicated both by the model solar wind/IMF and GCR/SEP data introduced in sections 2.2.2 and 2.3.2, respectively. Solar wind/IMF data sourced from Stereo-A (blue) and OMNI (red) derived using the Tao et al. (2005) model are shown in Figures 4a–4e. GCR/SEPs data from LEMMS channels E6 and P2 are shown in Figures 4f and 4g, respectively. Tick marks at the top of the figure show the time of apoapsis at the start of each Cassini Rev, numbered every other Rev, with alternating vertical white/light-gray-shaded regions indicating individual Revs from apoapsis to apoapsis. Arrows in Figure 4f indicate the 4-Rev sequences whose data are discussed in Text S3 and in the supporting information.

Figure 4a shows the model data source-Sun-Saturn separation angle corresponding to the solar wind plasma arriving at Saturn at that time, with horizontal black dotted lines being plotted at  $90^\circ$  intervals. We recall from section 2.3.2 that the  $\pm 90^\circ$  separation angle range shown centrally in the panel is a reasonable indicator of approximate validity of these data. The Stereo-A separation angle at the start of the interval was  $-20^\circ$ , increasing at a rate of  $\sim 1^\circ$  per day via  $0^\circ/360^\circ$  to  $\sim 280^\circ$ , equivalent to  $\sim -80^\circ$  modulo  $360^\circ$ , at the end of the Cassini mission. The OMNI data separation angle at the start of the interval was  $\sim 140^\circ$ , increasing at a similar rate via  $0^\circ/360^\circ$  to  $\sim 60^\circ$  at the end of the mission. Considering the  $\pm 90^\circ$  range for expected approximate validity, we note that from the start of the interval until Day 55 of 2017 Stereo-A lay within this angular range while OMNI did not, such that only the Stereo-A data (blue) are shown as the more reliable source during this interval. The same is true of the OMNI data (red) shown exclusively over the interval from Day 121 of 2017 to the end of the Cassini mission, except for the last  $\sim 10$  days of the mission when the Stereo-A separation angle again lay within the  $\pm 90^\circ$  range such that both data sets are then shown. For the interval between Days 55 and 121 of 2017, however, shown shaded dark gray in Figure 4a, neither separation angle lay within the  $\pm 90^\circ$  limit, such that we again plot both data sets due to the likely uncertainties of each.



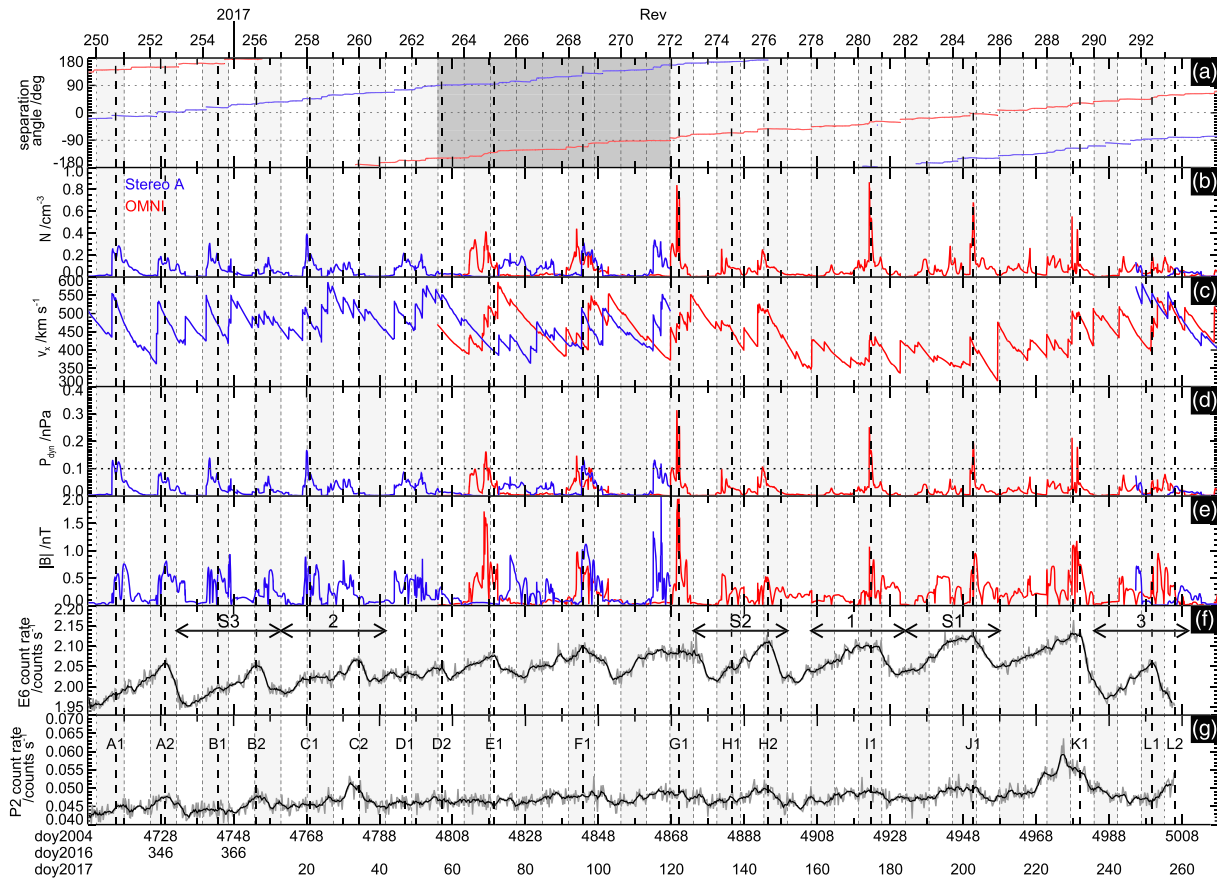


**Figure 4.** Plot indicating heliospheric conditions at Saturn from Day 326 of 2016 to Day 270 of 2017, spanning the Cassini F ring and proximal orbit interval (plus Rev 250). The 2016/2017 boundary is marked at the top of the figure. Also marked at the top are the times of apoapsides at the start of each Rev, labeled every other Rev, with vertical alternate white/light-gray striping across all panels marking full Cassini Revs. Figures 4a–4e show solar wind/IMF parameters derived from the Tao et al. (2006) propagation model, using data from Stereo-A (blue) and OMNI (red). Figure 4a shows the data source–Sun–Saturn separation angle for each data set, where the dark-gray-shaded region between Days 55 and 121 of 2017 corresponds to the interval where the separation angles of both data sets lie outside the  $\pm 90^\circ$  range of expected approximate validity. Both (less certain) model data sets are shown in this interval. Outside this range, only those data that lie within the  $\pm 90^\circ$  uncertainty limit are plotted (both of them for a short time near the end of the interval shown). Figures 4b–4e show the model solar wind density, velocity, dynamic pressure, and IMF magnitude, respectively. In Figure 4d the horizontal dotted line at 0.1 nPa gives a rough indication of dynamic pressures producing a significant compression of Saturn’s magnetosphere. Figure 4f shows a profile of  $>120$  MeV proton GCRs at Saturn determined from 6 hr averages of LEMMS channel E6 count rates (gray line), together with a seven-point (1.75 day) centered running average (black line). Four-Rev data intervals discussed in section 3 and the supporting information are indicated with the relevant section numbers by the horizontal arrows. Figure 4g shows 6 hr averaged and seven-point smoothed values of LEMMS channel P2 count rates presented in the same format, showing a weak response to energetic GCR protons, as for channel E6 in Figure 4f, onto which SEP proton fluxes in the energy range 2.3–4.5 MeV are superposed (see section 2.4). Assessment of the times of solar wind compressions of Saturn’s magnetosphere, to within a day or two in either direction, are shown by vertical black dashed lines. These are labeled in Figure 4g, where letters indicate events within a given solar rotation, with further information on the choice of times being given in Table 1.

Figures 4b–4e show the model solar wind particle density, velocity, dynamic pressure, and total IMF strength, respectively, limited as indicated above. We recall that the interval concerned corresponds to the late declining phase of the solar cycle when ICMEs are expected to occur infrequently, such that interplanetary disturbances are dominated by CIRs, often with two compression regions per solar rotation related to a modestly tilted solar magnetic dipole (e.g., Jackman et al., 2004). Examination of the model data clearly indicates the presence of modulations governed by the  $\sim 26$  day solar rotation period, as observed in the recurrent sudden increases in both the number density and flow speed across outwardly propagating shocks, both increases leading to sudden increases in solar wind dynamic pressure typically by more than an order of magnitude. Under usual conditions at Saturn the solar wind dynamic pressure lies between  $\sim 0.01$  and  $\sim 0.03$  nPa, corresponding to subsolar magnetopause distances between  $\sim 26$  and  $\sim 21 R_S$  according to the Kanani et al. (2010) magnetopause model. We may then consider dynamic pressure values of  $\sim 0.1$  nPa



**Table 1**

*Expected Solar Wind Compression Events During the Cassini F Ring and Proximal Orbit Interval, Based on LEMMS GCR/SEP Data and Tao et al. (2005) model solar wind/IMF values shown in Figure 4*

Event	Time doy2004	Time year/doy	Cassini rev	Timing indicators
A1	4715.7	2016/333.7	250	Stereo-A
A2	4729.3	2016/347.3	252	GCRs/Stereo-A
B1	4743.7	2016/361.7	254	Stereo-A/GCRs
B2	4754.3	2017/006.3	256	GCRs/Stereo-A
C1	4768.9	2017/020.9	258	Stereo-A/GCRs
C2	4782.3	2017/034.3	259	GCRs
D1	4795.0	2017/047.0	261	Stereo-A/solar period
D2	4805.0	2017/057.0	263	GCRs/solar period
E1	4819.5	2017/071.5	265	GCRs/OMNI
F1	4843.8	2017/095.8	268	GCRs/Stereo-A/OMNI
G1	4870.1	2017/122.1	272	GCRs/OMNI/Stereo-A
H1	4882.0	2017/134.0	274	OMNI/solar period
H2	4894.5	2017/146.5	276	GCRs/OMNI
I1	4922.8	2017/174.8	280	GCRs/OMNI
J1	4950.8	2017/202.8	284	GCRs/OMNI
K1	4980.0	2017/232.0	289	GCRs/OMNI/SEPs
L1	4999.8	2017/251.8	292	GCRs/solar period/OMNI
L2	5006.0	2017/258.0	293	SEPs

and above, a near order of magnitude increase, to be indicative of significant solar wind-driven compressions of the magnetosphere, resulting in the subsolar magnetopause being displaced inward to  $\sim 16 R_S$  or less. This indicative value is plotted as a horizontal dotted line in Figure 4d. The model data then generally indicate the presence of two significant compressions per solar rotation in the early interval sourced from Stereo-A, and generally one compression region per solar rotation in the later interval sourced from OMNI. These findings are in accord with solar coronal field measurements from the Wilcox Solar Observatory (<http://wso.stanford.edu/synsourcel.html>). Early in the interval the effective tilt of the solar magnetic dipole was sufficient to result in two clear equatorial crossings of the heliospheric current sheet per solar rotation, consistent with two fast solar wind streams and two CIR-related compressions with a  $\sim 13$  day periodicity. After March 2017 (Day  $\sim 60$ , equivalent to Day  $\sim 100$  at Saturn), however, the solar magnetic equator is generally only significantly displaced from the rotational equator once per solar rotation, consistent with only one fast stream and one CIR compression region every  $\sim 26$  days.

These model data may be compared with the  $>120$  MeV proton GCR flux measured in situ at Saturn shown in Figure 4f, where 6 hr averaged count rates shown by gray lines have been further smoothed using a seven-point running average (thus over  $\sim 2$  days) in order to reduce noise. These fluxes clearly display a  $\sim 26$  day solar rotation periodicity, though with an apparent change in phase by approximately half a solar rotation around Day  $\sim 50$  of 2017. The periodicity is particularly marked by abrupt drops in the GCR counts corresponding to Forbush decreases associated with the arrival of interplanetary shocks and large field strengths in the solar wind as outlined in section 2.2.2. Comparison of the principal drops with the model solar wind/IMF data in Figures 4d and 4e shows good consistency overall, with significant increases in the model dynamic pressure and field strength occurring near the start of each drop, generally to within a day or two in the intervals of expected model validity. During the early part of the interval to Day  $\sim 35$  of 2017 a secondary modulation of the GCR flux is also present, consisting of a marked cessation in the GCR count rate increase roughly half way between each sudden drop, followed by a further increase to peak values. These features give rise to an additional  $\sim 13$  day period in the spectral analysis of these data presented by Roussos, Jackman, et al. (2018). They are also associated with peaks in the model solar wind dynamic pressure and IMF strength in Figures 4d and 4e, during the initial interval in which the model data exhibit two compressions per solar rotation, thus with a  $\sim 13$  day periodicity.

Consideration of both the GCR and model solar wind/IMF data in Figure 4 allows us to make an initial assessment of the expected times at which solar wind compressions arrived at Saturn during this interval, indicated to within a day or two in either direction by the vertical black dashed lines. In order of relative importance, our criteria for identification of these times are (a) the times of Forbush decrease onsets in the GCR counts in Figure 4f, (b) the times of model dynamic pressure/IMF magnitude peaks in Figures 4d and 4e, (c) the times of SEPs transients in Figure 4g to be discussed below, and (d) smaller scale features in these data sets that are modulated with a solar periodicity of  $\sim 13$  or  $\sim 26$  days. These times are labeled in Figure 4g, where the letters in each label identify successive  $\sim 26$  day solar rotation periods, while numbers identify successive events within each solar rotation. Information on these times and their selection is given in Table 1. Overall, this analysis indicates the occurrence of 18 significant solar wind compressions (dynamic pressure  $> \sim 0.1$  nPa) during the  $\sim 9.5$  month study interval. Given the  $\sim 7$  day period of Cassini's F ring and proximal orbits, this corresponds approximately to one compression every other Rev in the early F ring orbit interval with  $\sim 13$  day solar recurrence, decreasing to one compression every fourth Rev in the later proximal orbit interval with  $\sim 26$  day solar recurrence.

Figure 4g also shows the count rate of LEMMS channel P2, which has been 6 hr averaged (gray line) and seven-point smoothed (black line) as for the GCR flux in Figure 4f. While designed to measure 2.3–4.5 MeV protons in the usual SEPs energy range, channel P2 is also weakly sensitive to higher energy

GCR proton fluxes. These dominate the P2 response for much of the interval, giving weak variations that mirror those in Figure 4f. However, near the end of the interval two significant enhancements are observed which deviate from the GCR behavior, classified as SEP transients by Roussos, Krupp, et al. (2018). The first starts on Day 215 of 2017, peaks on Day 228, and ends on Day 240. For this event no protons above 10 MeV were observed, such that the shock could be related to a CIR or an ICME, though Roussos, Krupp, et al. (2018) favor an ICME due to the long duration of the enhancement. The peak of the SEP counts occurs close to the time of a Forbush decrease in Figure 4f together with a dynamic pressure and IMF increase in Figures 4d and 4e, such that we consider these as the signatures of the same compression, labeled K1 (Table 1). The second SEP transient began on Day 254 of 2017, 2 days after the onset of the last observed Forbush decrease in Figure 4f labeled L1, with flux increases also being observed in LEMMS channels reaching proton energies of at least 60 MeV (Roussos, Krupp, et al., 2018). This indicates connection to a fast-approaching interplanetary shock, it being noted by Roussos, Krupp, et al. (2018) that the largest (X-class) solar flare of the previous decade occurred  $\sim 9$  days before the end of the Cassini mission, suggesting that this SEP transient was related to the ICME counterpart of this event. Due to the temporal separation from Forbush decrease L1, and since the SEP flux was still increasing at the end of the Cassini mission such that its duration and the time of peak flux remain unknown, we treat this as a separate event labeled L2, taken to be approximately contemporaneous with the end of mission.

### 3. Data Examples

We now examine three intervals illustrating aspects of the data during the F ring and proximal orbits. Each interval encompasses four full spacecraft Revs, thus spanning close to one full solar rotation, in order to examine the response of Saturn's magnetosphere to the recurrent variations in solar wind/IMF evident in Figure 4. Discussion of a further three such intervals is given in the supporting information, together encompassing over half of the overall data set. In choosing these examples, indicated by the numbered arrowed lines in Figure 4f, preference has been given to intervals where the model solar wind/IMF data lie within their regime of expected validity, and for which the generally sparse auroral imagery is optimally available.

#### 3.1. Revs 278–281: Compression Event I1

We begin by discussing data from proximal Revs 278–281, indicated by the arrowed line marked “1” in Figure 4f. These data represent a suitable starting point since they correspond to the later part of the interval when both the modeled heliospheric parameters and the GCR flux exhibit a relatively simple periodicity with one clear compression event occurring each solar rotation. Data from these four Revs are shown in Figure 5, spanning  $\sim 25.9$  days from 7.2 hr UT on Day 158 to 3.8 hr UT on Day 184 of 2017, close to the effective solar rotation period at Saturn of  $\sim 26$  days (as determined empirically from recurrent GCR fluxes by Roussos, Krupp, et al. (2019)). Figure 4 shows that these Revs span a single recurrent maximum in GCR flux, with solar wind rarefaction conditions being indicated at the start and end of the interval, and a single major compression event occurring centrally during Rev 280. This is associated with a flattening of the previously increasing GCR flux profile near the beginning of Rev 280 and the start of a Forbush decrease near its end. The approximate anticipated time of this compression, indicated as event I1 in Figure 4 and Table 1, is indicated by the vertical red arrow above the time series panels.

Figures 5a to 5e show field and plasma parameters in a time series format plotted over the interval of Revs 278–281. Figure 5a shows a RPWS spectrogram (section 2.2.3) between frequencies of 1 Hz and 2 MHz, with powers given in dB above background for each frequency band, as indicated by the color scale on the right of the panel, saturating at 40 dB. The background values were determined from the powers in each band over the full  $\sim 9.5$  month interval examined in this paper, given by the minimum 10% of values in each channel, thus providing consistency across all the RPWS spectrograms shown in the paper. The principal emissions observed are SKR at frequencies above a few kHz, and auroral hiss at frequencies below a few 100 Hz. Figure 5b shows 1 min averaged residual magnetic field data in spherical KGS coordinates, from which the Dougherty et al. (2018) Saturn internal field model has been subtracted, showing the residual radial component  $\Delta B_r$  (red), the residual colatitudinal component  $\Delta B_\theta$  (green) line, and the azimuthal component  $B_\phi$  (blue). Since the model field is exactly axisymmetric with zero azimuthal field, the azimuthal component is shown as measured. Figure 5c shows color-coded ion intensities for LEMMS channels A1–A4 spanning 35–506 keV as indicated on the right of the panel, while Figure 5d shows color-coded electron intensities for the

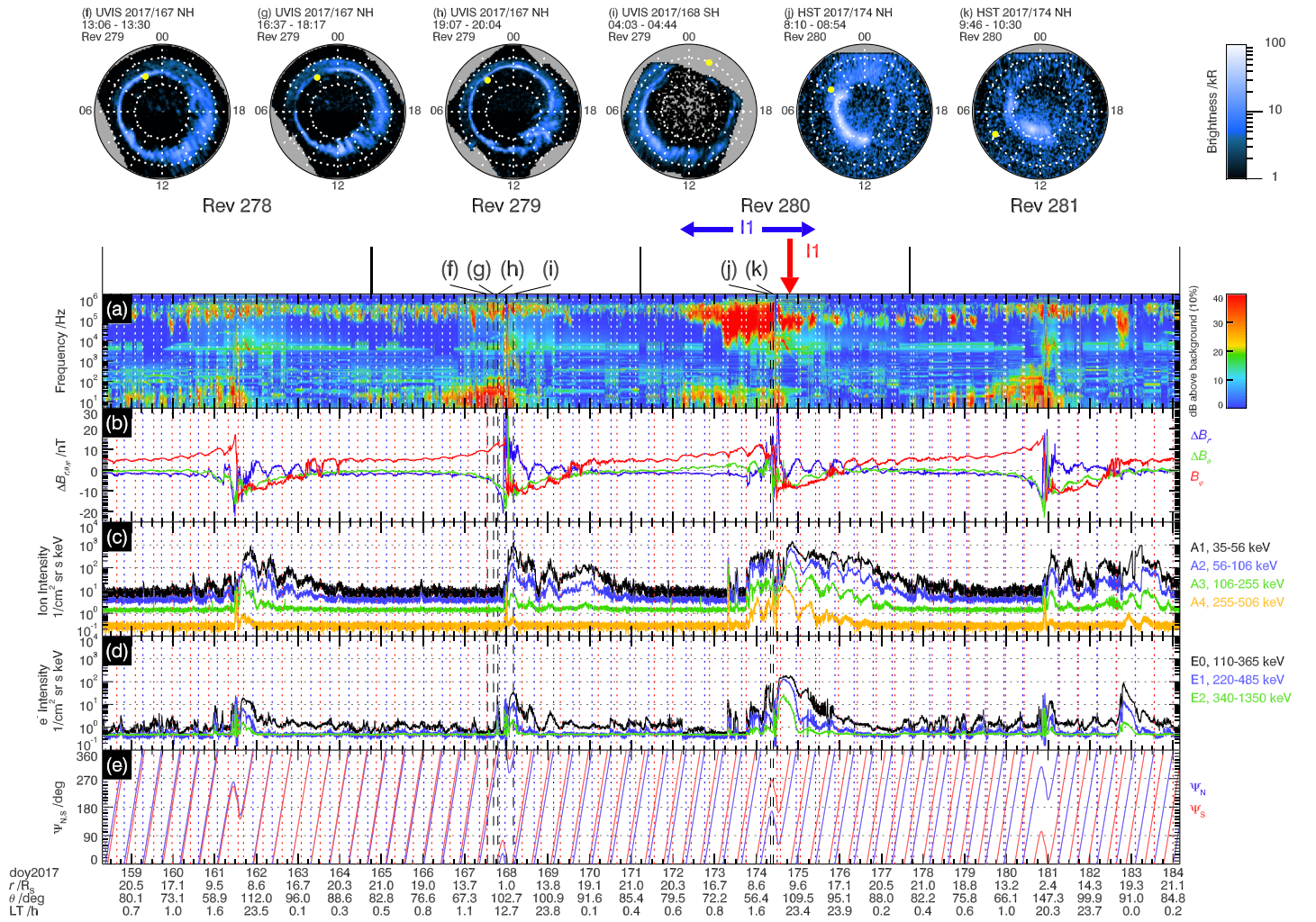


**Figure 5.** Four-orbit plot of data from Revs 278–281 spanning one solar rotation, showing the effect of solar wind compression event I1 on Rev 280. Figures 5a–5e show time series data as follows. (a) Color-coded RPWS wave-frequency spectrogram with emission powers in dB above background as indicated on the right of the panel; (b) residual magnetic field components in spherical polar coordinates referenced to the northern planetary spin/magnetic axis with the Dougherty et al. (2018) internal field model subtracted (nT),  $\Delta B_r$  red,  $\Delta B_\theta$  green, and  $B_\phi$  (as measured) blue; (c) and (d) LEMMS energetic ion and electron fluxes ( $\text{cm}^{-2} \text{sr}^{-1} \text{s}^{-1} \text{keV}^{-1}$ ) as labeled on the right of the panels; (e) local northern  $\Psi_N$  (blue) and southern  $\Psi_S$  (red) PPO phases, with vertical dotted lines showing times at which  $\Psi_N = 0^\circ$  (blue) and  $\Psi_S = 180^\circ$  (red) indicating when the local plasma sheet is thinned by each system. Time in Doy 2017 is shown at the bottom, together with spacecraft position in KGS coordinates, radial distance ( $R_S$ ), colatitude (deg), and LT (hr). The vertical black arrow at the top shows the expected time of arrival of compression I1 (Figure 4 and Table 1), while the interval during which responses were observed is indicated by the horizontal blue arrow (Table 2). Figures 5f–5k show UVIS and HST auroral images projected into the northern (NH) and southern (SH) hemispheres, together with Rev number and start and stop times. Start times are also indicated in the time series panels by the vertical black dashed lines, with correspondingly labeled ticks shown at the top of the panels. White dotted circles and radial lines show  $10^\circ$  steps of latitude and  $30^\circ$  intervals of longitude (2 hr LT), respectively. All images are oriented with midnight (00/24 hr LT) at the top and dawn (06 hr LT) to the left. Brightness is given by the logarithmic color scale on the right saturating at 100 kR, with regions for which no data are available being shaded gray. The mapped Cassini magnetic footprint is shown by the yellow circle.

LEMMS channels E0–E2 spanning 110–1,350 keV as also indicated on the right (section 2.2.2). Figure 5e shows the local northern  $\Psi_N$  (blue) and southern  $\Psi_S$  (red) PPO phases determined from the Provan et al. (2018) model (section 2.3.1), with successive rotations highlighted across the time series panels by vertical dotted lines showing the times when  $\Psi_N = 0^\circ$  (blue) and  $\Psi_S = 180^\circ$  (red), these being the phases for which the plasma sheet is expected to be thin and tail reconnection favored as discussed in section 1.3 (Figure 1). Maximally favored times for which the two systems act in concert are those for which the two PPO systems are near antiphase, thus near the times when the blue and red vertical dotted lines occur close together. The PPO data in Figure 5e show that the two PPO systems were rotating nearly in phase with each other at the start of the interval, thus with a beat phase not favorable for PPO-modulated



reconnection, moving toward antiphase conditions favorable for modulated reconnection at the end. The relative phase of the two systems was near to quadrature for Rev 280, during the anticipated compression event.

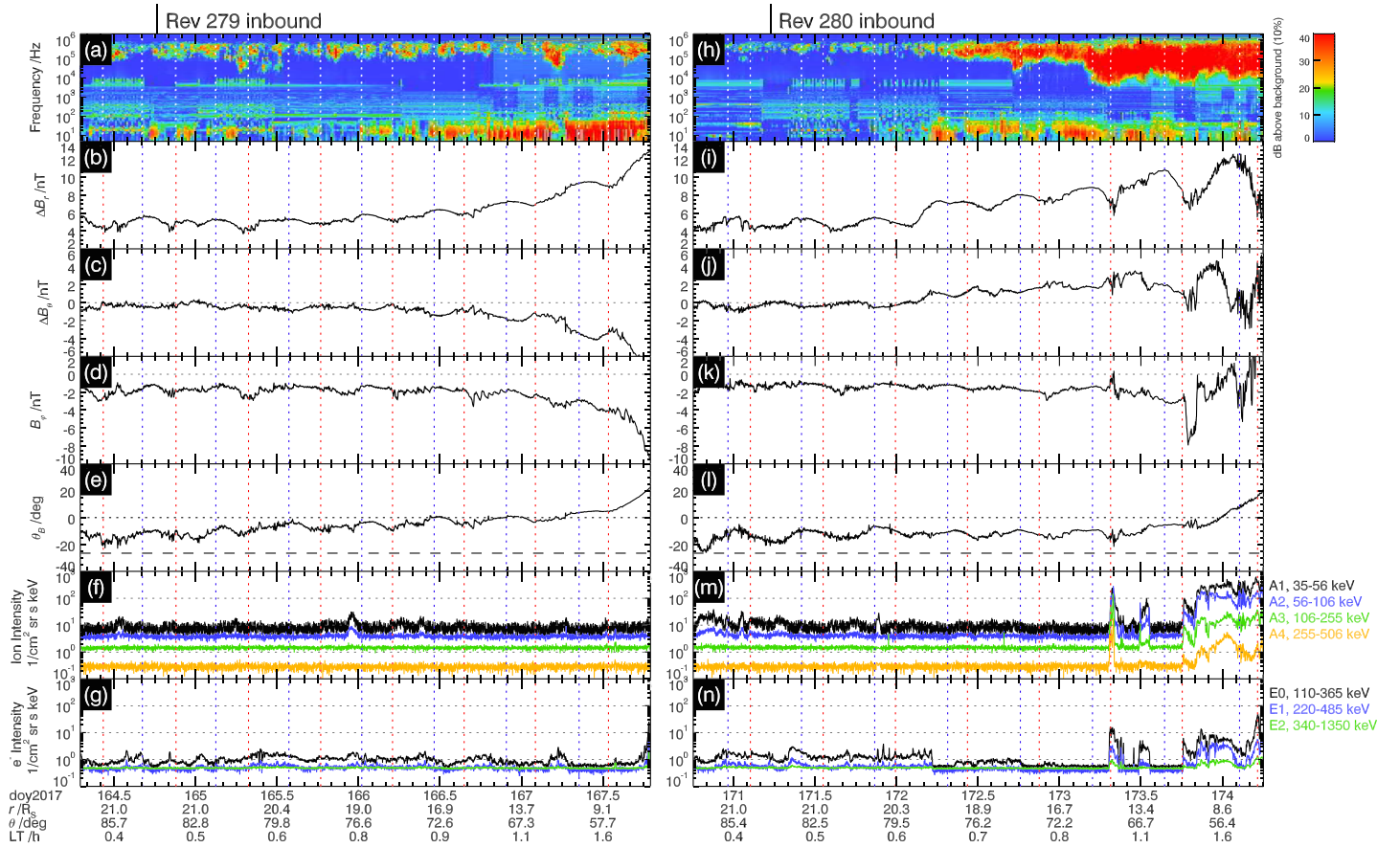
Figures 5f to 5k above the time series panels show selected Cassini UVIS and HST images of Saturn's northern hemisphere (NH) and southern hemisphere (SH) auroras projected onto the ionosphere as described in sections 2.2.4 and 2.2.5, with the start and end times of each and the Rev number being provided at the upper left of each image. The start times are also indicated by the black vertical dashed lines in the time series panels, with correspondingly labeled ticks shown at the top. In this case, images are available only for Revs 279 and 280, where we show three NH UVIS images obtained prior to periapsis on Rev 279 (Figures 5f–5h), a further SH UVIS image obtained after periapsis on Rev 279 (Figure 5i), and two HST NH images obtained near to periapsis on Rev 280 (Figures 5j and 5k). Intensities in kilo-Rayleighs (kR) are indicated by the color scale to the right of the projections, saturating white at 100 kR. The same scale is used for all the images displayed in this paper, again allowing ready cross-comparison between intervals. The footprint of the Cassini spacecraft, mapped along model field lines into the ionosphere is shown as a yellow circle. The model employed consists of the Dougherty et al. (2018) internal planetary field model plus the Bunce et al. (2007) ring current model for a subsolar magnetopause at  $22 R_S$ .

Figure 6 shows selected data on an expanded time base which we refer to below in discussion of the compression event, where the right hand panels (Figures 6h–6n) show data from the northern inbound pass of Rev 280 during the compression event, while the left hand panels (Figures 6a–6g) show data from the equivalent portion of quiet Rev 279. The intervals shown in each case are such that at the end of each plotting interval Cassini is located  $5 R_S$  from Saturn's center, with data from the preceding 3.5 days being shown. These intervals thus contain the inbound apoapses at the start of these Revs, indicated by the black tick marks at the top of the plots. Though PPO phases are not shown in the figure, blue and red vertical dotted lines show the times for local PPO phases  $\Psi_N = 0^\circ$  and  $\Psi_S = 180^\circ$ , respectively, as in Figure 5. These again thus indicate the times at which the local plasma/current sheet is expected to be thin due to the effects of the northern and southern PPO systems, respectively. Figures 6a and 6h show RPWS spectrograms using the same range and background powers as in Figure 5a. Figures 6b–6d and 6i–6k show the three residual spherical polar components of the magnetic field as in Figure 5b, plotted using a common vertical scale of 12 nT, though with the ranges adjusted to accommodate the data. Figures 6e and 6l show the tilt angle of the magnetic field vector in the meridian plane relative to the planet's equator, given by

$$\theta_B = \tan^{-1} \left( \frac{B_Z}{B_\rho} \right), \quad (4)$$

where  $B_\rho$  and  $B_Z$  are the cylindrical radial and axial field components in the meridian relative to the planet's spin/magnetic axis, respectively, and where we note that the total fields have been employed, not the residuals. In the northern hemisphere, as in Figure 6,  $\theta_B$  positive or negative indicates a field tilted away from or toward the equatorial plane, respectively. While at small radial distances the tail field is expected to be organized relative to the planetary equator as depicted in Figure 3, at larger radial distances the lobe field should deflect to become more aligned with the solar wind flow given approximately by the latitude of the Sun (Figure 2b), such that in the northern lobe under northern summer solstice conditions  $\theta_B \approx -26.5^\circ$ , as marked by the black dashed line in Figures 6e and 6l. Figures 6f, 6g, 6m, and 6n then show energetic ion and electron fluxes presented in a similar format to Figures 5c and 5d, though now over a more restricted flux range to better display the data.

We first examine the field and particle data in Figures 5b–5d to establish the physical regimes encountered, with reference to the spacecraft trajectory in the noon-midnight meridian projection in Figure 2b. The principal features in the residual radial field component (red) in Figure 5b are the successive intervals of positive and negative values, corresponding to spacecraft locations north and south of the magnetic equator, respectively. This residual field results from the combined action of the ring current dominating in the inner region and the magnetopause/tail currents at larger distances. It switches sign abruptly across the equator marking each dayside periapsis pass, and more slowly and with significant fluctuations prior to apoapsis (tick marks above the time series panels) on each nightside outbound pass. The asymmetry in duration of negative and positive values on the nightside is due to the displacement of spacecraft apoapsis north of the planetary



**Figure 6.** Plots showing data from equivalent segments of the northern inbound passes on Revs 279 (Figures 6a–6g) and 280 (Figures 6h–6n) on an expanded temporal scale compared with Figure 5. The intervals shown extend inward to a radial distance of  $5 R_S$  on each inbound pass, with the previous 3.5 days of data being plotted, encompassing apoapsis at the start of the Revs indicated by the black ticks at the top of the plot. Figures 6a and 6h show RPWS spectrograms in the same format as Figure 5. Figures 6b–6d and 6i–6k show the residual magnetic field components in spherical polar coordinates as in Figure 5b. Figures 6e and 6l show  $\theta_B$ , the tilt angle of the total (not residual) meridional magnetic field relative to Saturn's equatorial plane given by Equation 4, where the horizontal dashed line at  $-26.5^\circ$  indicates alignment with the solar wind flow radially away from the Sun. Figures 6f, 6g, 6m, and 6n show energetic ion and electron fluxes in a similar format to Figures 5c and 5d, though with a revised flux scale. Blue and red vertical dotted lines show the times of PPO phases  $\Psi_N = 0^\circ$  and  $\Psi_S = 180^\circ$ , respectively, as in Figure 5.

equator, combined with the southward displacement of the tail current sheet during northern summer conditions, as discussed in section 2.1 (Figure 2b). The residual colatitudinal field (green), also mainly due to the combined action of the ring current and magnetopause/tail currents, is small around apoapsis, but generally has significant negative values (northward field) comparable to those of the residual radial field near to periapsis. The azimuthal field (blue), principally due to magnetosphere-ionosphere coupling currents, is generally opposite in sense to the radial field and of lesser magnitude and is associated with field line sweepback due to subcorotation of the magnetospheric plasma.

As a further consequence of the north-south displacements of spacecraft apoapsis and the plasma/current sheet, outbound post-periapsis in the southern hemisphere the spacecraft is generally located on closed plasma sheet field lines where significant fluxes of energetic ions and electrons are observed. It then moves out of the plasma sheet into the northern lobe around apoapsis and during the northern inbound pass, where the energetic particle fluxes are generally reduced near to background values. The presence of hot plasma with energetic particle fluxes above background is also accompanied by short timescale fluctuations in the magnetic field, observed principally as thickening of the field value traces at the cadence shown in Figure 5 (see also Figure 6). Further effects evident in both particle and field data are the modulations near the  $\sim 10.7$  hr periodicity of the PPOs, emphasized by the sets of vertical dotted lines showing the times at which the two systems should favor thinned current sheets as described above. The perturbations

observed in the tail are those due both to north-south current sheet oscillations, favored during PPO in phase conditions early in the interval, and thickening/thinning modulations, favored during PPO antiphase conditions later in the interval, as described in section 1.3 (Figure 1).

We now examine these data for dynamical responses to the solar wind magnetospheric compression expected to occur during Rev 280, the approximate timing of which estimated from the heliospheric data in Figure 4 is shown by the vertical red arrow labeled I1 in Figure 5 (Table 1). Examining first the wave data in Figure 5a, we see there is little SKR activity during both Revs 278 and 279, and for the first few planetary/PPO rotation periods of Rev 280, apart from some short-lived PPO-modulated bursts. However, strong continuous SKR emissions are seen to begin at ~09 hr UT on Day 172 of 2017 on the inbound pass on Rev 280, following a step-like ~2 nT increase in the residual radial field in the northern lobe in Figure 5b at ~04 hr UT, and a decrease to near background in the energetic electron fluxes in Figure 5d. The residual colatitudinal field also undergoes a step-like increase from near-zero to ~1 nT positive (southward) values, unlike the behavior seen in the same region on the other three Revs in Figure 5. These features are taken to correspond to the initial magnetospheric responses to expected solar wind compression event I1, but beginning ~2.5 days before the timing estimated in Table 1.

These onset and initial responses are shown in the expanded time base plots in Figures 6h–6n. The behavior of the residual colatitudinal field (green) in Figure 5b is elucidated by examining the behavior of the meridional field tilt angle for Revs 279 and 280 in Figures 6e and 6l, respectively. In the near-apoapsis data at the start of the intervals shown  $\theta_B$  lies typically between  $-10^\circ$  and  $-20^\circ$  such that the field in the northern lobe is deflected away from the planetary equatorial plane ( $\theta_B \approx 0^\circ$ ) toward the expected direction of the solar wind flow, shown by the black dashed lines in these panels as indicated above. In the quiet-time pass on Rev 279  $\theta_B$  moves gradually toward near-zero values at smaller distances, that is, to increasing alignment with the planetary equator, before increasing rapidly to positive values in the innermost region displayed (see, e.g., Figure 3). On Rev 280, however, the increase in  $B_\theta$  following the compression results in  $\theta_B$  in Figure 6l remaining at negative values similar to those at apoapsis to smaller radial distances, before again becoming rapidly positive in the inner region. This behavior is indicative of the effect of the enhanced solar wind dynamic pressure on the tail field orientation following the onset of the compression event. In effect, the characteristic hinging distance of the current sheet,  $r_H$  in Equation 1, is reduced under these circumstances.

Examining the SKR data in Figure 5a following these initial effects, and on an expanded time base in Figure 6h, it is seen that a quasiperiodic series of LFEs, indicative of enhanced field-aligned current densities in the SKR source region, occur near ~18 UT on Day 172, ~05 UT and ~18 UT on Day 173, and ~02 UT on Day 174. The first of these is relatively short-lived, while the second is followed by a more enduring approximately three rotation frequency band expansion, until visibility of the northern hemisphere SKR source region is lost during the periapsis pass. The vertical dotted lines show that each of these LFEs occur near times when  $\Psi_N \approx 0^\circ$  and  $\Psi_S \approx 180^\circ$ , times that are relatively close together during this interval (unlike Revs 278 and 279), indicative of the presence of a thinned current sheet conducive to reconnection. Enhanced emissions continue for at least two planetary rotations on the outbound pass. The overall interval during which responses to the compression event were observed, as indicated principally by the field and SKR data, is shown by the horizontal blue arrowed line above the time series panels in Figure 5, in this case lasting for ~3.3 days or ~7.3 planetary/PPO rotations.

Neither the initial onset of continuously enhanced SKR, nor the following short-lived LFE at ~18 UT on Day 172 are associated with notable features in the field or energetic particle flux locally at the spacecraft. However, after the initial main LFE at ~05 UT on Day 173, there follows a ~1 hr burst of energetic ions and electrons, together with a rapid decrease in  $\Delta B_r$  and a simultaneous increase in  $\Delta B_\theta$ , such that the meridional field tilts further toward the planetary equator in Figure 6l. These field and particle signatures are indicative of the occurrence of a burst of tail reconnection which results in the injection of hot plasma toward the planet, resulting in an expansion of the plasma sheet and a dipolarization of the field at the spacecraft, then located ~15  $R_S$  from the planet. A positive perturbation in  $B_\phi$  is also seen in Figure 6k, indicative of an upward (relative to the ionosphere) field-aligned current flow within the perturbed region. A similar field and particle event also occurs in association with the subsequent frequency extension near ~18 UT on Day 173, though in this case with a strong negative  $B_\phi$ .



deflection indicative of a downward-directed field-aligned current. We also note the presence of a secondary  $\sim 2$  hr lower-intensity burst of energetic particles occurring between these two bursts, centered near  $\sim 13$  UT on Day 173, which in this case had no similar field or SKR signatures. This occurred near PPO phases where the plasma sheet is expected to be expanded due to the combined action of the two systems, and also possibly displaced somewhat to the north, due to the action of the dominant northern PPO system (see Figure 1). This provides further evidence for an expanded plasma sheet at this time, since no similar enhancements were observed on Rev 279 or 281. Following these bursts, the spacecraft remained within a region of enhanced energetic particle flux as the planet was approached, indicative of a hot plasma regime on the nightside which was clearly expanded poleward compared with prior and following Revs 279 and 281, on which no such regime was observed. Overall, these data provide clear evidence for the occurrence of PPO-modulated bursts of tail reconnection on Rev 280 following a CIR-related magnetospheric compression by the solar wind, resulting in hot plasma injections, expansion of the plasma sheet, dipolarization of the field, and enhanced coupling currents. As a consequence of this activity significantly enhanced fluxes of both energetic ions and electrons were observed throughout the outbound plasma sheet on Rev 280 compared with the other Revs in Figure 5, even after the cessation of significant SKR emissions. We note that the overall plasma flow within this regime is rotational with the planet, at approximately half of rigid corotation (Kane et al., 2020; Thomsen et al., 2014), such that the injected hot plasma evidently continues to circulate around the planet for at least several planetary rotations (few days) thereafter. The fluxes are generally lower on Rev 281, however, and even lower on Rev 282 (Figure S1 in the supporting information), showing that such conditions do not generally persist on week-long Rev orbit period timescales.

We now examine the auroral images in Figures 5f–5k, recalling that the first four images were acquired by UVIS around periapsis on Rev 279, while the last two were acquired by the HST just prior to periapsis on Rev 280,  $\sim 2.5$  Saturn rotations after the onset of the main LFE, but while the SKR event remained in progress. For the UVIS images on Rev 279 it can be seen that the main auroral oval was fairly steady in shape and intensity, with the nightside main emission at typical  $\sim 15$ – $16^\circ$  colatitudes in the NH and  $\sim 17$ – $18^\circ$  in the SH, with peak intensities of  $\sim 40$  kR throughout. The relatively steady nature of the emissions over a  $\sim 15$  hr interval, together with the modest intensities and typical locations is indicative of a relatively quiet interval without significant reconnection-related dynamics in the tail. The Cassini field-line mapping (yellow dot) in the inbound images places the spacecraft just poleward of the auroral region in the postmidnight sector, consistent with the northern tail lobe conditions inferred from the in situ data in Figures 5b–5d, and with the presence of near-continuous auroral hiss at frequencies below  $\sim 50$  Hz in Figure 5a. Examining the HST images obtained close to periapsis on Rev 280 (Figures 5j and 5k), however, reveals significantly changed conditions, in which the auroras were strongly contracted to  $\sim 10^\circ$  colatitude in the NH and brightened to  $\sim 100$  kR on the dawnside in the first of the images. The auroral contraction from usual  $\sim 15^\circ$  northern colatitudes prior to periapsis on Rev 179 to  $\sim 10^\circ$  colatitudes near periapsis on Rev 280, is indicative of the net closure of  $\sim 25$  GWb of open flux in the LFE event on Rev 280, representing a significant fraction of the usual open flux in the system. The mapped spacecraft location correspondingly lies well equatorward of the contracted auroral region, consistent with a location on newly closed field lines within a poleward expanded plasma sheet containing hot energized plasma. Auroral hiss emissions in Figures 5a and 6h are also more sporadic, and generally anticorrelated in intensity with the energetic particle fluxes.

The data in Figure 4 suggest that heliospheric conditions over the following solar rotation spanning the next four spacecraft Revs 282–285 was similar to that during the interval discussed above, leading to the expectation of a similar single compression event (J1) taking place on Rev 284 (Table 1). However, examination of these data, presented in Figure S1 in the supporting information, and related text, shows a much more muted response observed on the outbound pass of Rev 284. While for individual events such differences could result from variations in heliospheric conditions, here only indirectly determined, consideration of the responses to all the compression events in section 4 shows that the nature of the response is modulated by the PPO beat phase, with “major” responses as in the present example generally occurring for beat phases lying in the  $\sim 180^\circ$  sector centered on antiphase, conducive to the occurrence of tail reconnection, but with more “minor” responses occurring for beat phases lying in the  $\sim 180^\circ$  sector centered on in phase conditions. We note here that the beat phase for present example I1 was near quadrature moving toward antiphase, while that for event J1 under similar heliospheric conditions was close to in phase.

### 3.2. Revs 257–260: Compression Events C1 and C2

Our second example considers the four-F ring orbit interval Revs 257–260 during which heliospheric conditions in Figure 4 are different from those on Revs 278–281 (section 3.1), with the occurrence of two compression events. These Revs spanned  $\sim 28.7$  days, now slightly longer than a solar rotation, from 23.5 hr UT on Day 12 to 15.8 hr UT on Day 41 of 2017 shown by the arrow marked “2” in Figure 4f. This interval again encompassed a full cycle of GCR variation with the flux increasing from minimum values at the start of Rev 257 back to similar conditions at the end of Rev 260, via a Forbush decrease starting at the end of Rev 259. The model solar wind and IMF data correspondingly indicate rarefaction conditions on starting and ending Revs 257 and 260, with two compression events between, separated by an interval of weaker dynamic pressure and IMF magnitudes. The first compression event (C1) began near the start of Rev 258 and was accompanied by a flattening in the rise of the GCR flux lasting throughout that Rev, while the second (C2) occurred more uncertainly on Rev 259 and is taken to be associated with the Forbush decrease. Data from these Revs are shown in Figure 7 in the same format as Figure 5, with the times of anticipated compressions C1 and C2 (Table 1) again indicated by arrows at the top of the time series panels. We note from Figure 7e that the PPO beat phase was close to antiphase near the start of the interval, conducive to PPO-modulated tail reconnection, moving toward in phase conditions toward the end. Figure 8 examines the response to compression C1 on an expanded time base, showing the inbound portions of Revs 257 and 258 in the same format as Figure 6. The plots for both Revs again end at a radial distance  $5 R_S$  from the planet on the inbound pass, with the previous 3.5 days being shown, again encompassing apoapsis indicated by the black tick marks at the top of the plots.

Figure 2 shows that the main distinction of the F ring orbits lies in their lesser eccentricity compared with the proximal orbits, resulting in the trajectory being displaced to greater distances north-south from the center of the plasma sheet on both the inbound and outbound passes, while traversing the central tail plasma/current sheet region outbound at similar  $\sim 17.5 R_S$  radial distances. As a consequence, unlike during the proximal orbits, the spacecraft often exited the plasma sheet into the southern lobe for some interval postperiapsis on the outbound passes, as evidenced both by the absence of energetic particles and the presence of auroral hiss. In addition, significantly greater thickening is required to enter the plasma sheet from northern lobe conditions on the inbound passes.

Examining the data in Figure 7 we first see that, apart from the passage through the radiation belts at periapsis, the energetic ion and electron fluxes were low throughout starting and ending Revs 257 and 260 when extended solar wind rarefaction conditions are anticipated. On the outbound passes PPO-modulated transitions between the outer plasma sheet and southern tail lobe are observed on both Revs, as indicated by the modulated weak energetic particle fluxes and auroral hiss, with entry to the plasma sheet occurring in both cases near phases when the plasma/current sheet is overall deflected toward the south with the dominant northern system (blue vertical dotted lines). In both cases, energetic particle fluxes were near background with strong auroral hiss for much of the inbound passes as expected. However, PPO-modulated short-lived bursts of intense SKR were observed for much of Rev 257 (similar to Rev 283 in Figure S1 in the supporting information), likely indicative of Vasyliunas cycle activity under PPO antiphase beat phase conditions. As shown in greater detail in Figure 8a, these SKR bursts typically peak about a quarter cycle after optimum thin plasma sheet conditions occurred (vertical dotted lines) under local phase conditions  $\Psi_N \sim 90^\circ / \Psi_S \sim 270^\circ$  at the spacecraft, possibly associated with rotation of the injected hot plasma into the dawn sector where the field-aligned currents and SKR emissions maximize (e.g., Mitchell et al., 2009). If such injections did occur, however, the effects do not reach sufficiently far north to produce signatures in the inbound in situ Cassini data, with only steady PPO-related oscillations being present in the magnetic field data, and with energetic particle fluxes being near background essentially throughout (Figures 8b–8g). Only weak sporadic SKR emissions were observed during Rev 260 (after the end of the active interval initiated on Rev 259 discussed below), under in phase PPO beat phase conditions, together with very weak energetic particle fluxes throughout. We note that the SH UVIS auroral image in Figure 7f obtained outbound on Rev 257 during the interval of SKR bursts shows an expanded oval with weak emissions, not indicative of major tail dynamics. No images are available for Rev 260.

Very different conditions are observed in Figures 7 and 8h–8n on Rev 258, which took place under PPO beat phase conditions approaching quadrature from antiphase. The onset of the response to compression C1

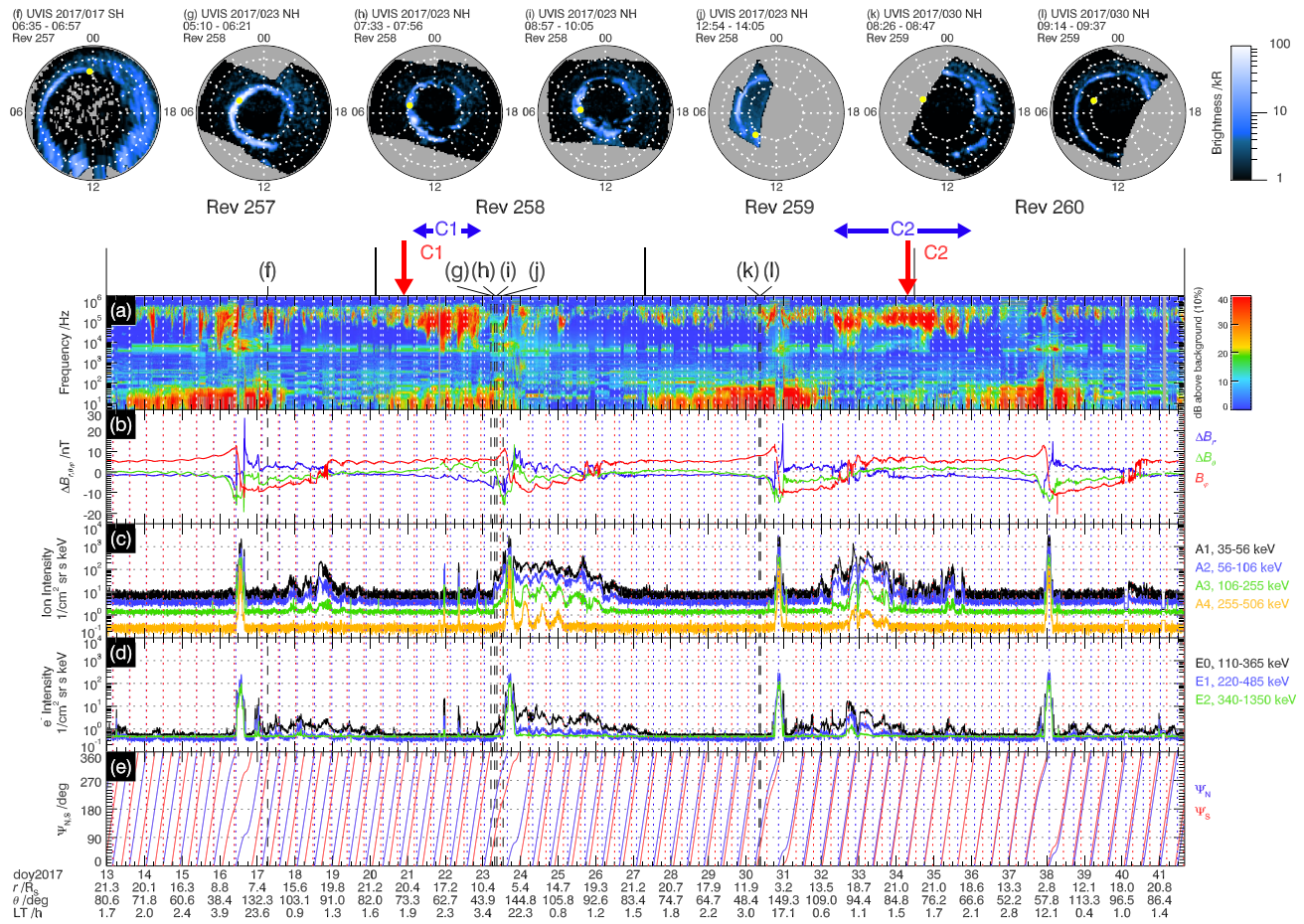


**Figure 7.** Data from Cassini F ring Revs 257–260 plotted in the same format as Figure 5. The approximate anticipated times of compression events C1 and C2 shown in Figure 4 and Table 1 are indicated by the labeled vertical red arrows above the panels.

began at ~03 hr UT on Day 21, shortly after the anticipated time (Table 1), with a relatively rapid ~1.5 nT increase in the residual radial field and a more gradual increase from near zero to ~1–2 nT positive values in the residual colatitudinal field (Figures 7b, 8i, and 8j). As for compression event I1 in Figure 6, these changes result in the meridional field remaining more aligned with the solar wind flow inward to smaller radial distances than for Rev 257, as can be seen by comparing Figure 8l with Figure 8e. For Rev 258 the field angle starts to increase toward positive values only near the beginning of Day 22, compared with the more gradual rise on Rev 257. In both cases, however, the positive values attained by the end of the interval are larger than those for the proximal orbit in Figure 6, due to the more northward displacement of the F ring trajectories at 5  $R_S$  radial distance (Figures 2 and 3).

Following the initiation of these field changes, an interval of continuously enhanced SKR emission occurred (blue arrow C1), lasting for four planetary/PPO rotations (Figures 7a and 8h). This began at ~06 hr UT on Day 21, close to the time of optimally thinned plasma sheet conditions following the onset of the compression, though no LFE or particle event is observed near this time. However, a PPO-modulated extension of the SKR spectrum to lower frequencies peaked near to  $\Psi_N \sim 180^\circ / \Psi_S \sim 90^\circ$  conditions on each of these planetary/PPO rotations, with the last three accompanied by short-lived bursts of energetic particles of diminishing intensity (Figures 8m and 8n) and sharp changes in the residual radial and colatitudinal fields indicative of brief entries into the plasma sheet (Figures 8i and 8j). While these periodic particle and field effects may well be related to PPO-modulated reconnection bursts and consequent particle injections, the phase conditions under which they are observed correspond to those for which the plasma sheet is expected to be near maximum thickness, and displaced northward from its averaged southward seasonally displaced position due to the net action of the northern PPO system (Figures 1d and 2b). This is approximately opposite



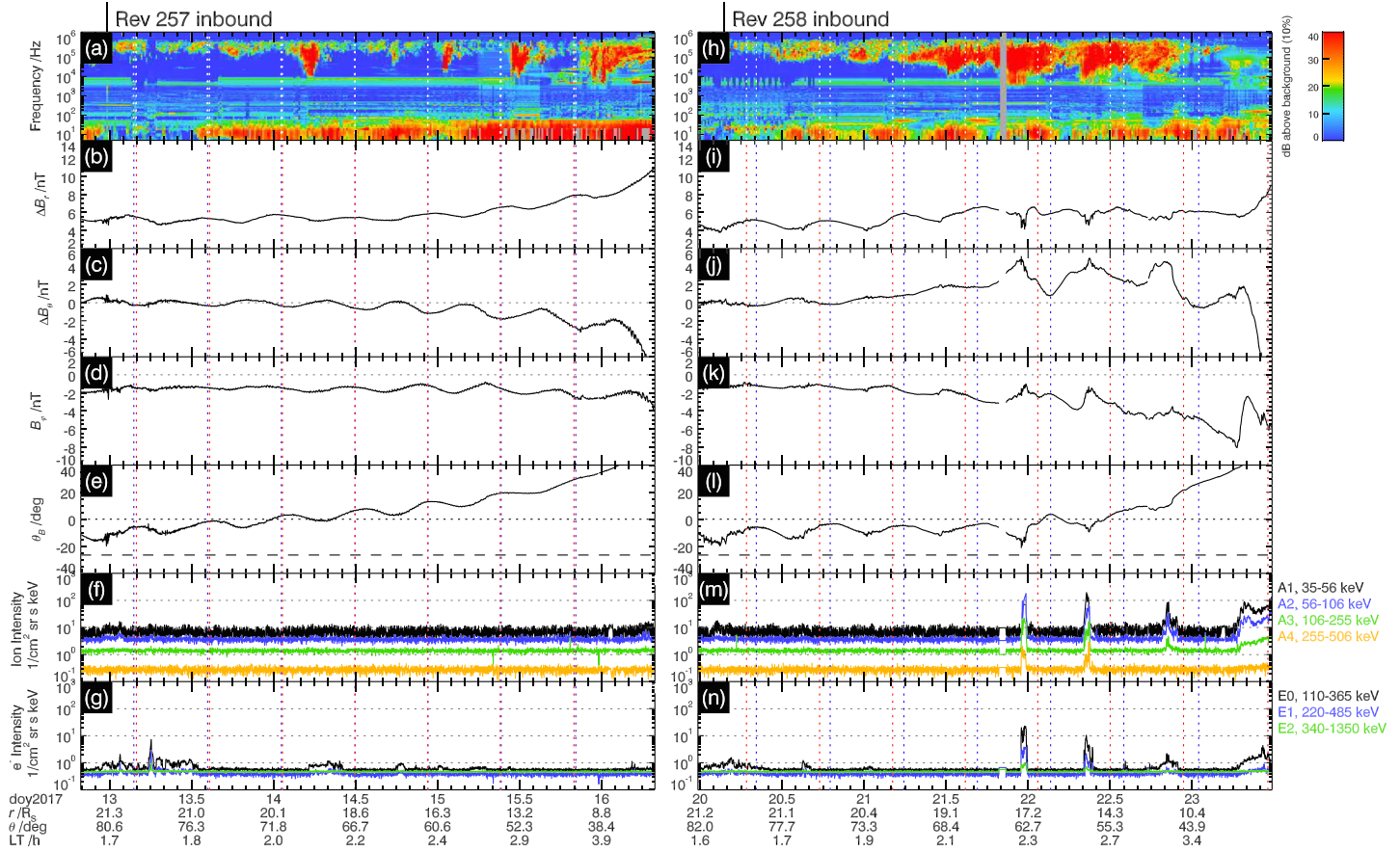


**Figure 8.** Data from Cassini F ring Revs 257 and 258 plotted in the same format as Figure 6.

to the behavior in the storm-related LFEs occurring during the proximal orbit interval described in section 3.1 above (see also section S2 of the supporting information for discussion of an additional proximal orbit example), which instead occur near optimally thinned plasma sheet conditions  $\sim 180^\circ$  away in phase. Given the F ring orbit azimuth at  $\sim 2\text{--}3$  hr LT in the postmidnight sector (Figure 2a), we note that  $\Psi_N \sim 180^\circ$  corresponds to the condition that the center of the upward field-aligned current region of the northern PPO system at  $\Psi_N = 90^\circ$  (Figure 1b) lies in the postdawn sector in the northern hemisphere where the most intense SKR sources are usually located (e.g., Lamy et al., 2009). We also note from section 2.2.3 that the SKR data are likely primarily responding to northern sources for at least the inner part of the F ring orbit northern inbound passes. The SKR PPO modulations peaking near  $\Psi_N \sim 180^\circ$  in Figure 8h, not uncommon during the F ring orbit storm responses, may thus result from better visibility of the PPO-modulated stronger dawn sources from postmidnight LTs on the F ring orbits than from nearer midnight on the proximal orbits (Figure 2a).

Following the three brief particle bursts mentioned above, each observed under  $\Psi_N \sim 180^\circ$  conditions while the SKR event was in progress, a more enduring enhancement in energetic particle fluxes was observed at smaller radial distances at the end of the inbound pass of Rev 258 (Figures 8m and 8n), which is not present in the equivalent segment of Rev 257 data (Figures 8f and 8g). This is again indicative of an expanded night-side region of hot injected plasma that remained present during the planetary rotation following the end of the storm interval as indicated by the SKR data (Figure 8h). Similar regions of injected hot plasma were also observed on the inbound passes of F ring Revs 251, 261, and 263 resulting from the responses to compressions A1, D1, and D2 (Figure 4 and Table 1), but not in general otherwise. On the outbound pass of Rev 258 the energetic particle fluxes were considerably enhanced compared with prior Rev 257 and subsequent Rev 260, with no transition to lobe field lines postperiapsis or prior to apoapsis, as also indicated by the

consistent lack of auroral hiss. These observations are thus also consistent with the presence of a thick hot plasma sheet in the inner part of the nightside tail throughout the outbound pass.

Four NH UVIS auroral images obtained preperiapsis on Rev 258 spanning ~8 hr during the planetary rotation after the end of the main SKR burst (vertical black dashed lines) are shown in Figures 7g–7j. Importantly, the first three images confirm the occurrence of a global contraction of the auroras to a bright oval at ~10° northern colatitude, indicative of the closure of a substantial fraction of the open tail flux during the prior interval of compression-induced activity. The mapped position of the spacecraft, shown by the yellow dot in the images, is colocated with the contracted oval, consistent with the simultaneously observed energetic particle fluxes. However, we also note that in the final image obtained on Rev 258 shown in Figure 7j, in which only the dawn auroras were observed, the oval had expanded somewhat to more usual colatitudes, consistent with the cessation of rapid closure of open flux in the tail, combined with an interval of rapid opening of flux at the magnetopause.

A somewhat less pronounced response to compression C2 commenced at ~08 hr UT on Day 32, ~2 days prior to the anticipated time (Table 1), under near in-phase PPO conditions on the outbound pass of Rev 259. Prior to this time the field and particle data, together with the auroral images in Figures 7k and 7l, indicate the occurrence of quiet conditions on this Rev, similar to those occurring under rarefaction conditions on Revs 257 and 260. The responses include enhanced SKR emissions which lasted intermittently for approximately seven planetary rotations extending to the end of Day 35 on the inbound pass of Rev 260 (blue arrow C2), but without significant LFEs indicative of intervals of more intense field-aligned currents. Enhanced residual radial fields were also observed in the northern hemisphere following the current sheet crossing on Day 32 indicative of compressed conditions, together with a small positive residual colatitudinal field, though reducing in intensity on Day 34. Strong fluxes of energetic particles were observed within the outbound plasma sheet on Days 32 and 33, with weaker bursts continuing to Day 35 on the inbound pass of Rev 260. Similar more muted responses to compression event J1 observed under near in phase conditions outbound on proximal Rev 283 are discussed in Text S1 in the supporting information, while stronger responses to compression event H2 observed under near-antiphase conditions near apoapsis between proximal Revs 275 and 276 are discussed in Text S2. In addition, in Text S3 we discuss observations on the four-orbit F ring Revs 253–256 which immediately precede those discussed here, on which heliospheric conditions were similar, but beat phase conditions were near-opposite, with near-in-phase conditions earlier in the interval, moving toward antiphase at the end. This led to more minor responses being observed to the first compression, B1, and more major to the second, B2, opposite to that occurring for compressions C1 and C2 discussed here. Overall, this ensemble of results again provides illustration of the role of PPO beat phase in response to solar wind compressions of the magnetosphere, being strong and often involving repeated PPO-modulated LFE and particle events indicative of tail reconnection bursts when the beat phase lies between antiphase and quadrature favorable for PPO-related current sheet thickness modulation, but with more muted responses occurring under less favorable circumstances when the beat phase lies between in phase and quadrature.

### 3.3. Revs 290–293: Compression Events L1 and L2

Our third example returns to the proximal orbit interval to examine data from Revs 290–293, the final four Revs of the Cassini mission consisting of three and a half orbits before the end of mission in Saturn's atmosphere during the periapsis pass of Rev 293. The data from these Revs span a ~22.6 day interval from 20.9 hr UT on Day 235 to 10.6 hr UT on Day 258 of 2017, as indicated by the arrow marked "3" in Figure 4f. The model solar wind/IMF data from both Stereo-A (blue) and OMNI (red) sources lie within their regimes of approximate validity during the later part of this interval, as shown in Figure 4, but exhibit little correspondence during the rather disturbed conditions then prevailing. The GCR fluxes, however, show minimum values during Rev 290 indicative of rarefaction conditions on this Rev (agreeing with the model data sourced from OMNI), followed by a rapid uninterrupted rise to peak values during the first half of Rev 292, and then a Forbush decrease continuing to the end of mission. Compression event L1 in Figure 4 and Table 1 associated with the Forbush decrease is thus anticipated to have occurred somewhat prior to periapsis on Rev 292. As discussed in section 2.4, however, 2 days after the Forbush decrease onset a SEP event of rising intensity began (Figure 4g), indicative of an approaching ICME, possibly associated with an X-class solar flare that occurred ~9 days earlier

(Roussos, Krupp, et al., 2018). Since this event continued to the end of mission, a second shock-associated compression event of uncertain timing is anticipated, labeled L2 in Figure 4. The data from these Revs are shown in Figure 9 in the same format as Figure 5 with the anticipated times of compressions L1 and L2 indicated by arrows, where we see that the PPO beat phase conditions were near in phase at the start of the interval, not conducive to PPO-modulated tail reconnection, but moved toward quadrature and antiphase conditions toward the end. In Figure 10 we examine data for Revs 292 and 293 in the same format as Figure 6, showing on an expanded time base the responses to both compressions L1 and L2 on the inbound passes of these Revs. The plots for both Revs again end at a radial distance  $5 R_S$  from the planet on the northern inbound passes, with the previous 3.5 days of data encompassing spacecraft apoapsis (black tick mark at the top of the plot) being shown. A quiet time proximal orbit comparator plot can be found for Rev 279 in Figures 6a–6g.

We first note that during the anticipated rarefaction conditions on Rev 290 the SKR emissions were very weak and sporadic throughout, and the energetic particle fluxes low, similar to the observations under corresponding heliospheric conditions during starting proximal Revs 273, 278, and 282 in Figures S2, 5, and S1, respectively. The UVIS SH auroral image obtained close to periapsis on this Rev shown in Figure 9f also exhibits a typical quiet oval with weak emissions. During following Rev 291 the SKR emissions and energetic particle fluxes remained relatively weak with little evidence of major tail dynamics, though somewhat larger than on Rev 290. Low-amplitude PPO-related particle flux modulations were observed on the northern inbound pass, with peaks occurring at times when the plasma sheet is expected to be tilted maximally to the north under PPO in phase conditions (red dotted lines, see Figure 1), and larger fluxes on the southern outbound pass similar to those occurring, for example, on Rev 279 in Figure 5. The SH UVIS auroral image obtained during the outbound pass in Figure 9g again shows the presence of a relatively quiet auroral oval, though a little more contracted than that for Rev 290.

On following Rev 292 the residual radial field became elevated at  $\sim 02$  hr UT on Day 249 shortly after apoapsis (again compared with Revs 290 and 291), while the residual colatitudinal field became simultaneously displaced from near zero to small positive values (Figures 9b, 10b, and 10c), these being taken to be a response to compression L1, though occurring  $\sim 2.5$  days prior to expectation. The field tilt angle in the meridian in Figure 10e maintains relatively steady negative values until the middle of Day 250. Modestly enhanced (compared with Revs 290 and 291) PPO-modulated SKR emissions are also present from near apoapsis on the inbound pass (end of Day 248), but do not suggest the occurrence of marked dynamics at this time under relatively unfavorable PPO beat phase conditions lying between in phase and quadrature. Instead, over the next three planetary (PPO) rotations to the middle of Day 250 the inbound spacecraft moved periodically between the northern tail lobe and the outermost northern plasma sheet, as indicated by the brief sporadic enhancements in energetic particle flux, related field perturbations, and modulated auroral hiss (Figures 10b–10g). Entries into the outer plasma sheet occurred at PPO phases when the plasma sheet is expected to be tilted northward toward the spacecraft. Midway through Day 250 on the inbound pass, however, with beat phase conditions nearer to quadrature, the SKR emissions intensified with the abrupt onset of a LFE which began (like those in Figures 5 and S1) at PPO phases close to where the tail plasma/current sheet is expected to be thinnest, more specifically near the vertical blue dotted line where  $\Psi_N = 0^\circ$ . Intense emissions with a lower-frequency component were only maintained for two planetary rotation periods, however, and declined to much smaller values on the final rotation prior to the periapsis pass on Rev 292 (blue arrow L1). Following the LFE, PPO-modulated bursts of energetic ions and electrons were observed on all three preperiapsis rotation periods at phases where the plasma sheet is expected to be thicker and moderately tilted to the north (between the pairs of blue and red dotted lines). During the second of these bursts a sharp negative deflection was observed in the azimuthal field component (Figure 10d), indicative of crossing a sheet of current directed downward into the northern ionosphere. Enhanced particle fluxes compared with Revs 290 and 291 were also observed throughout the outbound pass (Figure 9c and 9d). These features are all indicative of flux closure and hot plasma injection in response to compression L1, late in an event taking place under relatively unfavorable PPO beat phase conditions. We also note that the SH UVIS auroral image obtained somewhat after the end of the LFE event near periapsis on this Rev, shown in Figure 9h, indicates the presence of a rather dim oval similar to those observed on Revs 290 and 291, but again one that appears slightly contracted on the nightside relative to both these.



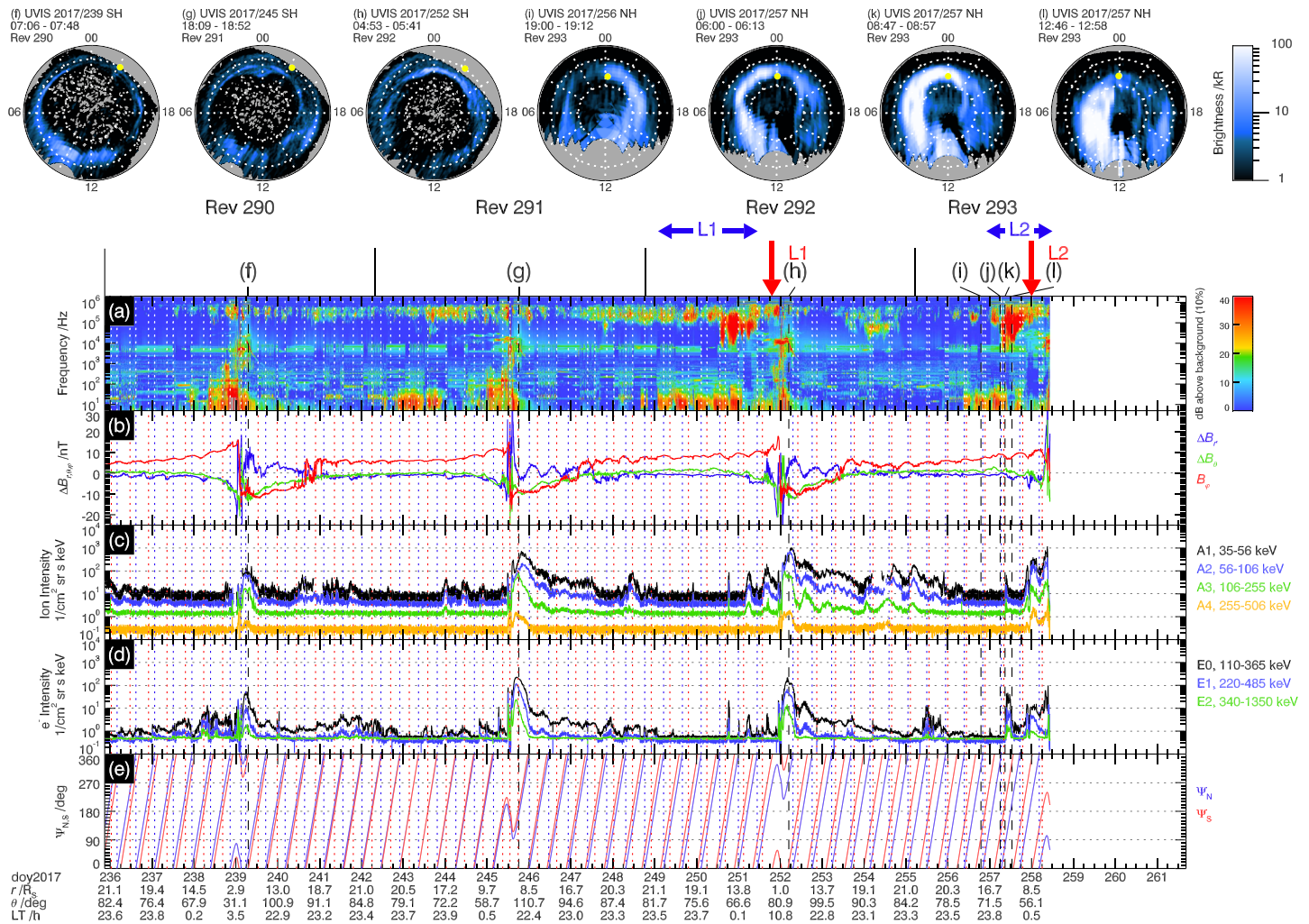


**Figure 9.** Data from Cassini proximal Revs 290–293 plotted in the same format as Figure 5. The approximate anticipated times of compression events L1 and L2 shown in Figure 4 and Table 1 are indicated by the labeled vertical red arrows above the panels. The Cassini mission ended in Saturn's atmosphere on the periapsis pass of Rev 293.

We finally consider data from the inbound pass of Rev 293, on which the impact of an ICME shock is anticipated on the basis of the SEP data shown in Figure 4g, compression event L2, though at an uncertain time. PPO beat phase conditions lay between quadrature and antiphase during this interval, relatively conducive to modulated plasma sheet thinning and reconnection bursts. Quiet conditions were observed on this pass until the second half of Day 256, though the plasma sheet is evidently still in an expanded state following the activity on Rev 292, with enhanced ion and electron fluxes persisting until ~10 UT on Day 256. After this time the spacecraft was located in the northern tail lobe as also seen in the loss of high-frequency fluctuations in the magnetic field components, and the onset of auroral hiss emissions. An enhancement in the residual radial field component, together with an increase in the residual colatitudinal component to small positive values, took place at ~22 hr UT on Day 256, indicative of tail compression (Figures 10i and 10j). At ~06 UT on Day 257 a major SKR intensification began with a rapidly developing LFE, again initiated close to the time of expected maximally thinned tail plasma sheet (vertical blue and red dotted lines) following the compression as indicated in the field data (Figures 9a and 9h). These field and SKR features are taken to correspond to the initial responses to ICME-related compression event (blue arrow L2). Following the LFE onset the radial field rapidly declined while the colatitudinal field rapidly increased indicative of a field dipolarization, culminating in the occurrence of an energetic particle burst, particularly intense in energetic electrons, which began at ~08.5 UT on Day 257 approximately a quarter PPO cycle after the LFE onset

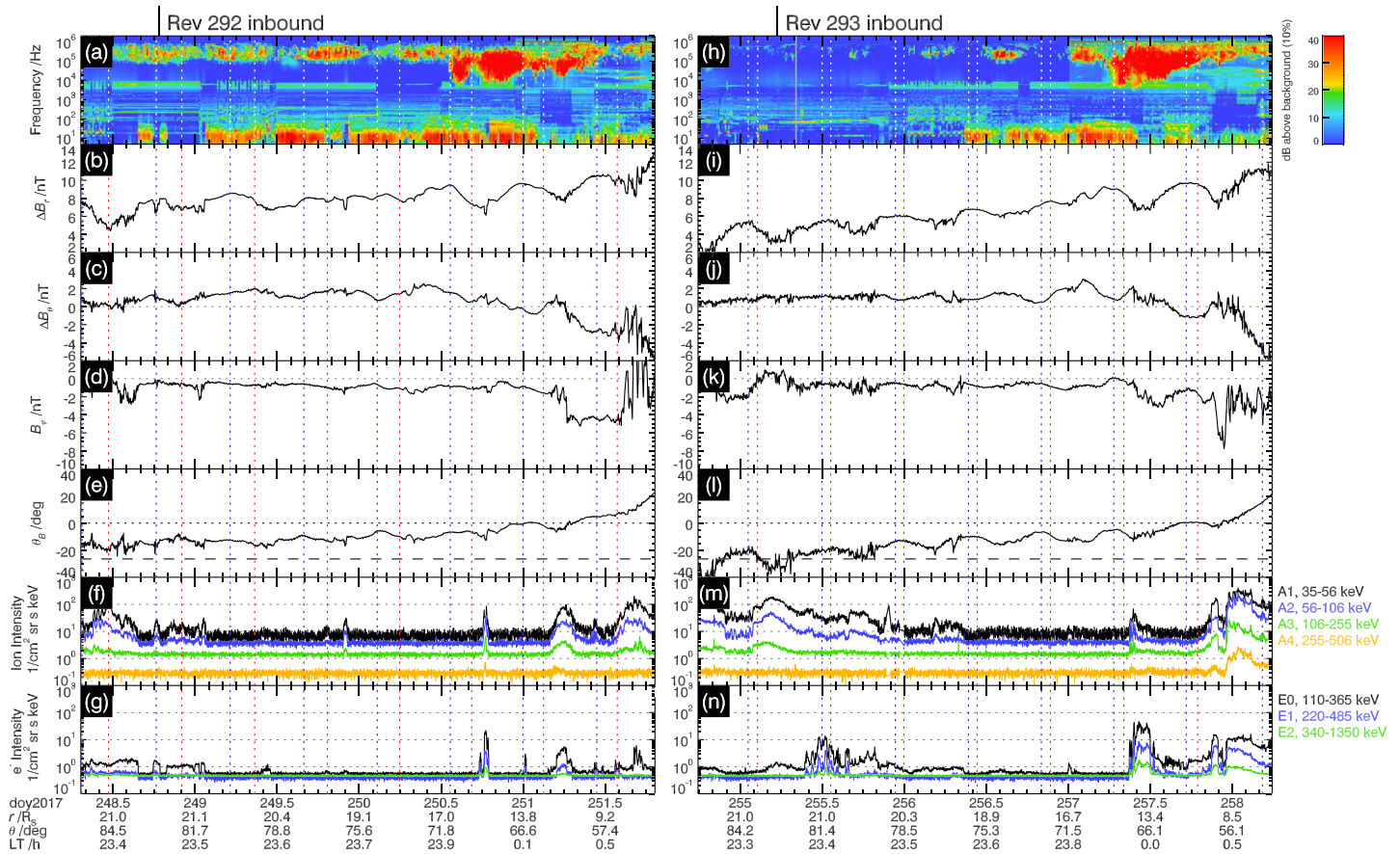


**Figure 10.** Data from Cassini Revs 292 and 293 plotted in the same format as Figure 6.

(Figures 10i–10n). The intense SKR emissions for this event lasted for essentially one planetary/PPO rotation before declining in intensity and frequency band during the subsequent rotation prior to periapsis. The energetic electron fluxes following the initial burst remained weaker but above background until increasing again together with the energetic ions under expectedly thickened plasma sheet conditions on the next PPO cycle, and remained so elevated until close to periapsis. We note the close similarity of these observations to those observed previously in the storm intervals on Rev 276 in Figures S3h–S3n in response to compression H2, and Rev 280 in Figures 6h–6n in response to compression I1. In addition to Rev 292, similar significant plasma injection effects associated with a contracted oval were also observed on proximal Revs 272 following compression G1 occurring toward the end of Rev 271, and on Rev 288 in response to compression K1\* (see section 4), i.e., about one every fourth orbit, but not otherwise.

Selected NH auroral images obtained by UVIS on Rev 293 with unusually good cadence on this final inbound pass, previously discussed by Palmaerts et al. (2018), are displayed in Figures 9i–9l and show the evolution of a large auroral storm associated with the LFE and plasma injection event. The first image in the sequence shown in Figure 9i, obtained prior to the LFE (first vertical black dashed line during Rev 293 in the time series panel) shows only weak oval emissions stronger at dusk than at dawn, similar to the images from Revs 290–292 shown in Figures 9f–9h. The Cassini footprint is located just poleward of the emission close to midnight, consistent with the quiet northern lobe conditions observed at this time in the time series panels. The second image displayed, in Figure 9j), is contemporaneous with the intensification of the SKR emission and onset of the LFE, and is the first image in the UVIS sequence to show storm-related features, with a brightening of the auroras throughout the dawn sector to peak intensities of ~140 kR. The Cassini footprint at noon lies just to the west of the brightened region and is again just poleward of the auroral region, consistent with the tail lobe location indicated in the in situ data at this time

**Table 2**  
*Properties of the Compression Events Observed During the Cassini F Ring and Proximal Orbit Interval*

Event/revs major/minor	Event start H:DoY/Year location/parameters <sup>a</sup>	Event stop H:DoY/Year location/parameters	Duration	Injections Inbound <sup>b</sup>	EP plasma sheet out <sup>c</sup>	Auroral <sup>d</sup> contraction	SKR LFE <sup>e</sup> /duration interval H:DoY/Year	SKR LFE <sup>f</sup> N/S phase <sup>f</sup>	Beat phase <sup>g</sup> deg mod 360°
A1/250–251 Major	16:335/2016 <sup>h</sup> Apoapsis/SKR/AB/EP	~00:339/2016 <sup>h</sup> Inbound/SKR	3.3 days 7.5 PR <sup>i</sup>	Yes	Yes	Moderate; Dawn max	Yes/1.7 days/3.8 PR 08:336–00:338/2016	0°/180°	190–164° 177°
A2/252 Minor	~00:345/2016 Inbound/AB/SKR	~00:348/2016 Outbound/SKR	~3 days ~7 PR	No	Yes	- <sup>j</sup>	No	-	115–90° 102°
B1/254–255 Minor	09:362/2016 Outbound/SKR/EP	~00:368/2016 Inbound/SKR	~5.6 days ~8.1 PR	Yes	Yes	-	No	-	328–279° 303°
B2/256 Major	18:06/2017 Inbound/AB/SKR	~00:10/2017 Outbound/SKR	3.3 days 7.3 PR	No	Yes	-	Yes/0.8 days/1.7 PR 04:09–22:09/2017	0°/180°	242–217° 229°
C1/258 Major	03:21/2017 Inbound/AB/SKR	23:22/2017 Inbound/SKR	1.9 days 4.2 PR	Yes	Yes	Strong; Dawn max	Yes/1.4 days/3.1 PR 12:21–21:22/2017	180°/270°	125–109° 117°
C2/259–260 Minor	08:32/2017 Outbound/SKR/EP/AB	~00:36/2017 Inbound/SKR/EP	3.7 days 8.2 PR	Yes	Yes	-	No	-	29–358° 13°
D1/261 Major	04:44/2017 Inbound/AB/SKR	22:45/2017 Outbound/SKR	1.8 days 3.9 PR	No	Yes	Moderate; Dawn max	Yes/1.8 days/3.9 PR 04:44–22:45/2017	0°/90°	289–274° 282°
D2/263 Major	12:56/2017 Inbound/AB/SKR	21:58/2017 Inbound/SKR/AB	2.4 days 5.3 PR	Yes	Yes	Moderate; Dawn max	Yes/1.4 days/3.2 PR 09:57–21:58/2017	Mixed	184–163° 173°
E1/264–265 Minor	~00:70/2017 Apoapsis/SKR/EP/AB	~00:73/2017 Inbound/SKR/AB	~3 days ~7 PR	Yes	Yes	Moderate; Dawn max	No	-	67–42° 55°
F1/268 Minor	10:93/2017 Inbound/AB/SKR	~09:95/2017 Periapsis/SKR	2.0 days 4.4 PR	No	Yes	Moderate; Postdawn max	Yes/0.3 days/0.7 PR 12:94–20:94/2017	0°/180°	231–214° 222°
F1*/269 Minor	04:100/2017 Inbound/AB/SKR	~13:103/2017 Outbound/SKR	~3.4 days ~7.6 PR	No	Yes	Slight; Midnight-dawn max	No	-	175–147° 161°
G1/271–272 Minor	08:118/2017 Outbound/SKR/AB/EP	09:121/2017 Inbound/SKR/AB	3.0 days 6.8 PR	Yes	Yes	Moderate; Dawn max	No	-	21–355° 8°
H1/274 Major	23:134/2017 Inbound/SKR/AB	18:136/2017 Outbound/SKR	1.8 days 4.0 PR	No	Yes	-	Yes/~0.7 days/1.6 PR 23:134 to ~16:135	0°/180°	236–220° 228°
H2/275–276 Major	02:145/2017 Apoapsis/AB/SKR/EP	03:148/2017 Inbound/SKR	3.0 days 6.6 PR	Yes	Yes	-	Yes/1.0 & 0.5 days/2.2 and 1.1 PR 06:145–06:146/2017 12:147–23:147/2017	0°/180°	150–125° 138°
I1/280 Major	04:172/2017 Inbound/AB/SKR	10:175/2017 Outbound/SKR	3.3 days 7.3 PR	Yes	Yes	Strong; Postdawn max	Yes/1.8 days/4.1 PR 05:173–01:175/2017	0°/180°	280–252° 266°
J1/284–285 Minor	20:201/2017 Outbound/SKR/AB/EP	~18:203/2017 Apoapsis/AB/SKR/EP	1.9 days 4.3 PR	Yes	Yes	-	No	-	19–1° 10°
K1*/287–288 Major	15:222/2017 Apoapsis/AB/EP/SKR	18:226/2017 Outbound/SKR	4.1 days 9.3 PR	Yes	Yes	Strong; Predawn max	Yes/1.2 days/2.7 PR 11:225 to ~16:226/2017	90°/270°	192–155° 174°
K1/289 Major	13:231/2017 Inbound/AB/SKR	17:233/2017 Outbound/SKR	2.2 days 4.7 PR	No	Yes	Slight; Wide dawn max	Yes/0.3 and 1.0 days/0.7 and 2.3 PR 16:231–00:232/2017	0°/270°	112–92° 102°
L1/292 Minor	02:249/2017 Apoapsis/AB	11:251/2017 Inbound/SKR	2.4 days 5.3 PR	Yes	Yes	Moderate; Midnight max	16:232–17:233/2017 Yes/0.5 days/1.0 PR	0°/90°	302–278° 290°
L2/293 Major	22:256/2017 Inbound/AB/SKR	Probably after end of mission	>1.5 days >3.4 PR	Yes	<sup>k</sup>	Strong; Dawn max	13:250–00:251/2017 Yes/0.5 days/1.0 PR 06:257–17:257/2017	0°/180°	225–247° 236°

<sup>a</sup>Parameters indicated in order of clarity/prominence; SKR indicates emission enhancement,  $\Delta B$  indicates changes in residual  $B_r$  and  $B_\theta$  as discussed in the text, EP indicates associated energetic particle bursts. <sup>b</sup>This indicates energetic particle bursts observed inbound and/or expanded layer observed preperiapsis. <sup>c</sup>This indicates enhancement of energetic particle flux in the outbound plasma sheet above typical quiet time values. <sup>d</sup>This indicates whether contracted auroral oval was observed during/after the event and the LT segment of peak brightness. <sup>e</sup>LFE indicates occurrence of low-frequency extension down to ~10 kHz. <sup>f</sup>Approximate local PPO phasing at the spacecraft of onset/modulated SKR LFE emission to within ~90° quadrant. <sup>g</sup>PPO beat phase range of event interval and mean value. <sup>h</sup>Times considered accurate to typically plus/minus quarter of a planetary/PPO rotation; ~ indicates greater uncertainty typically plus/minus half a planetary/PPO rotation. <sup>i</sup>PR means units of planetary/PPO rotations taken to have a nominal value of 10.7 hr. <sup>j</sup>A dash indicates the lack of relevant auroral imagery concerning the event. <sup>k</sup>No outbound pass at end of Cassini mission.



(Figures 10i–10n). Three hours later, contemporaneous with the onset of the hot plasma injection event at Cassini, Figure 9k shows the image with the brightest emissions peaking at  $\sim 600$  kR, together with broadening of the region of bright dawn emissions and expansion into the premidnight sector. The Cassini footprint then lay in the poleward part of the brightened oval near midnight. The final UVIS image, in Figure 9l, obtained directly after the initial energetic electron burst, shows that the bright emissions at this time, peaking at  $\sim 310$  kR, had rotated into the postmidnight to noon sector, and had also expanded significantly poleward, consistent with the closure of a significant fraction of the open tail flux during this event. The Cassini footprint at that time lay in the equatorward portion of the contracted and dimmed oval emissions near noon.

#### 4. Data Overview

In section 3 we showed that the solar wind compression events anticipated in section 2 from examination of the model solar wind/IMF and GCR flux data in Figure 4, as tabulated in Table 1, generally produce clearly identifiable dynamical effects in Saturn's magnetosphere as observed in Cassini remote sensing and in situ data on the F ring and proximal orbits, augmented by HST auroral imagery. While five of these events were discussed in some detail in section 3, augmented by a further five in the supporting information, an overview of the effects observed during all 18 intervals is given in Table 2, to which we have added two further “unanticipated” similar events, F1\* and K1\*. Event F1\* was observed principally in field signatures on the inbound pass of Rev 269 (similar to Rev 280 in Figure 6), occurring on the Rev directly after anticipated event F1. Whereas event F1 is associated with the start of a Forbush decrease in the GCR flux in Figure 4f, event F1\* is associated with a further sharp decline in flux toward minimum values during the solar rotation concerned. Unlike event F1, no clear signatures were associated with F1\* in the modeled solar wind and IMF data in Figures 4d and 4e, however, though we note that the model values sourced from both OMNI and Stereo-A lay outside of their expected regime of validity during this interval. Event K1\* was observed in field, particle, and SKR signatures near to apoapsis between Revs 287 and 288, prior to anticipated event K1 on Rev 289. As shown in Figure 4g, this interval is associated with a SEP event indicating the approach and impact of an interplanetary shock. The SEP flux rose prominently during Rev 287 and peaked during Rev 288, prior to the Forbush decrease observed in the GCR flux in Figure 4f that is associated with compression event K1 on Rev 289 (see also discussion in Roussos, Krupp, et al. (2018)). This sequence of heliospheric events then led to two separate compression-related intervals, K1\* followed by K1. Overall, Table 2 thus documents 20 compression events in total over the  $\sim 300$  day F ring and proximal orbit interval.

Column 1 of Table 2 gives the event identifier and Rev number. Columns 2 and 3 give information on the start and stop times of the observed compression-related effects, together with an indication of the parameters employed to identify the onset/cessation of the event, and the orbit regimes in which the effects were observed. The effects include the meridional residual field components as discussed in section 3 ( $\Delta B$ ), enhancements in the SKR emission, and bursts of energetic particles (EP). These are the intervals marked by the horizontal blue arrows in the four-Rev data plots discussed in section 3 and the supporting information. Onset/cessation timings are considered well-determined generally to within  $\sim \pm 2$  hr, corresponding to an overall window a little less than half a planetary/PPO rotation period, taken for definiteness to be 10.75 hr in Table 2. Events of greater timing uncertainty due to less distinct effects are indicated by a “ $\sim$ ” sign. Column 4 gives the overall duration of the event in days and equivalent planetary/PPO rotation (PR) periods. Events have durations typically lying between  $\sim 2$  and  $\sim 3.5$  days ( $\sim 4.5$ –8 PR), with an overall average value for well-determined intervals of 2.7 days (6.0 PR). Such an interval corresponds to  $\sim 40\%$  of a Cassini F ring/proximal orbit period, such that the events typically occupy a significant fraction of the Rev(s) on which they occur. It also corresponds to  $\sim 10\%$  of an effective solar rotation period at Saturn, such that the events are present for  $\sim 10\%$  of the time if there is one compression event per solar rotation, appropriate to five of the solar rotation periods encompassed here (E, F, G, I, and J in Figure 4), and to  $\sim 20\%$  of the time if there are two events per solar rotation appropriate to the remaining seven solar rotation intervals.

Columns 5–7 of Table 2 provide a summary of the physical effects observed during the Revs on which each compression interval occurs. Specifically, Column 5 concerns energetic particle bursts or poleward expanded layers observed on the inbound passes otherwise located on northern tail lobe field lines, while Column 6 concerns enhancements in energetic particle fluxes within the plasma sheet outbound, relative to quiet

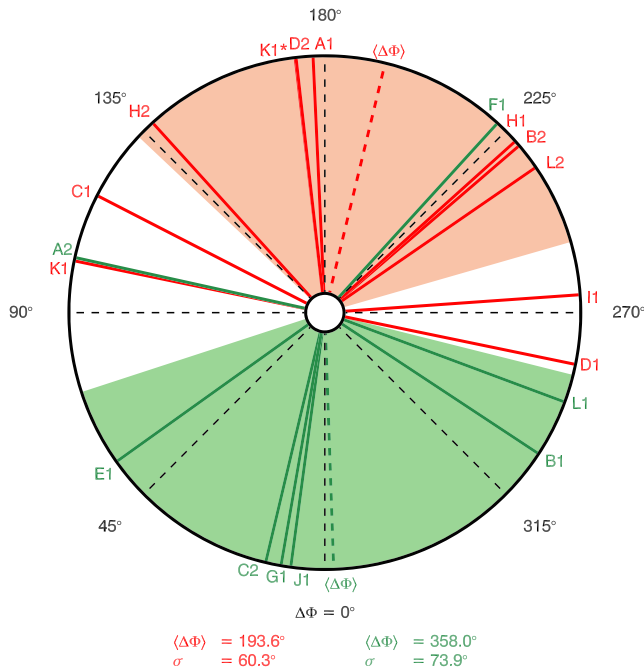


**Figure 11.** Averaged PPO beat phases for the compression events in Table 2 (column 10) are shown plotted on a phase wheel, with in phase conditions at the bottom and antiphase conditions at the top. The phases of major events as defined in section 4 are shown in red, while those of minor events are shown in green (event F1\* being excluded due to its rather different character). The phase values are labeled with the corresponding event identifier (see Tables 1 and 2). The red and green dashed lines indicate the directional means of these two sets of values (Equation 5), with the paler-red- and green-shaded regions displaying the circular standard deviations about these respective means (Equation 6).

pass values (see below), observed during the event interval or on the outbound pass directly after. Bursts of energetic particles are observed inbound in a majority (~70%) of these events, while an enhancement above quiet time fluxes in the outbound plasma sheet is seen in all cases. Column 7 gives an indication of the auroral conditions observed, if there is relevant imagery, meaning imagery providing an indication of conditions during or directly after the event interval (if not, a dash is shown). Specifically, we indicate whether the auroral oval appears contracted relative to its usual location, and the LT sector of any notable enhancement in intensity. A contraction may be indicated either through examination of a temporal sequence of relevant images if such exists, or by comparison with the median averaged oval position determined by Bader, Badman, Kinrade, et al. (2019) if not. A “moderate” contraction in Table 2 indicates a poleward contraction of ~2–3° (larger than the PPO-related oscillation of  $\sim \pm 1^\circ$  about the median) in some broad sector, while a “strong” contraction indicates a contraction  $> \sim 4^\circ$ . In most cases where such imagery is available, a moderate or strong contraction is apparent, with a prominent enhancement in intensity in the dawn sector. The dawn enhancement is a significant indicator of the occurrence of tail activity (e.g., Bader, Badman, Kinrade, et al., 2019; Cowley et al., 2005), while the contracted nature of the oval, sometimes strongly so such as on Revs 258, 280, and 293 as discussed in section 3 (Figures 5, 7, and 9), shows that a significant quantity of open tail flux is closed during such events, leading to poleward contraction of the outer boundary of the oval and the associated hot plasma regime.

Column 8 of Table 2 gives information on whether a SKR LFE was observed during the event, specifically meaning an interval of intense emission extending down in frequency to at least ~10–20 kHz, taken to be indicative of the development of intense field-aligned currents

in the auroral SKR source regions observed. If so, the interval of observation is given, together with its duration in days and PR. Thirteen out of 20 events (65%) show at least one such interval (sometimes two separated intervals as for Revs 275–276 in Figure S2 in the supporting information), with an averaged total duration for well-determined intervals of 1.2 days (2.7 PR). Thus, compression-related LFE intervals typically endure for two to three planetary/PPO rotation periods, corresponding to somewhat less than half the overall duration of each event. For those events that contain LFE intervals, Column 9 also gives an indication of the local north and south PPO system phases at the spacecraft,  $\Psi_{N,S}$ , associated with LFE onsets and/or PPO-modulated intensifications, to within the nearest 90° phase quadrant. The phase difference between the two systems during the event, the beat phase defined by Equation 3, is given in column 10, both as a range over each compression event, and as a mean value. In accordance with the discussion in section 3, most of the events with LFEs occur within the beat phase range between ~90° and ~270° spanning antiphase, that is, when the two PPO systems act in concert to thin and thicken the plasma sheet rather than to oppose each other. Even so, the values in Column 9 indicate that it is the moderately dominant northern system that principally governs the timing of onset/intensification of LFEs, with 10 out of 13 LFE cases (~75%) having onsets/intensifications timed near northern PPO phases of ~0°/360° associated with a thinned plasma sheet, as in numerous examples discussed in section 3. Although in seven of these cases the southern PPO phase is near ~180°, also associated with a thinned plasma sheet, thus indicating maximally thinned conditions under the dual action of the two systems, in three cases where the beat phase is nearer to quadrature, the onsets/intensifications occur near northern PPO phases 0°/360°, while the southern phases have more neutral values around ~90° or ~270°. Overall, however, these findings are consistent with the LFE events being associated with the onset or enhancement of tail reconnection rate associated with PPO-modulated thinning of the plasma sheet, which in turn modulates the intensity of the auroral field-aligned magnetosphere-ionosphere coupling currents.



On the basis of these results we have divided the events into two groups termed “major” and “minor,” as indicated in the first column of Table 2. Major events are those with LFE intervals with durations greater than one planetary/PPO rotation (11 out of 20 events, or 55%), while minor events either have no LFE interval as defined above (7 out of 20 events, or 35%), or one whose duration is one planetary/PPO rotation period or less (2 out of 20 events, or 10%). While this division is somewhat arbitrary, it does appear to separate events into two reasonably distinct types of response as discussed further below, with major events being roughly commensurate with the “long duration LFE” event category discussed by Reed et al. (2018), having LFE durations exceeding 20 hr. The major events here have an average LFE duration of ~32.5 hr (1.4 days or 3.0 PR), representing an interval of approximately half the overall duration of these events (2.7 days or 6.0 PR).

It is evident from this discussion that the major events defined above occur preferentially during PPO beat phase antiphase conditions, while the minor events occur preferentially under beat phase in phase conditions. The extent of this division is indicated in Figure 11, which shows the average beat phase of each event (Column 10 of Table 2) plotted in a beat phase circle which has in phase conditions ( $\Delta\Phi = 0^\circ$ ) at the bottom, northern leading quadrature ( $\Delta\Phi = 90^\circ$ ) on the left, antiphase ( $\Delta\Phi = 180^\circ$ ) at the top, and southern leading quadrature ( $\Delta\Phi = 270^\circ$ ) on the right. Event F1\* has been excluded since the conditions under which it occurs, directly following anticipated event F1 as discussed above, are rather different from those of the other events. The phases of major events are shown as solid red lines, while those of minor events are shown as solid green lines, each labeled with the corresponding event identifier. With a few exceptions, the major events with extended LFEs principally populate the upper half circle about antiphase, while the minor events without extended LFEs principally populate the lower half circle about in phase. For a set of  $K$  such phase angles,  $\Delta\Phi_k$ , where  $k = 1, 2, \dots, K$ , the directional mean  $\langle\Delta\Phi\rangle$  and circular standard deviation  $\sigma$  of these phase values are given by

$$Re^{i\langle\Delta\Phi\rangle} = \frac{1}{K} \sum_{k=1}^K e^{i\Delta\Phi_k}, \quad (5)$$

where real quantity  $R$  satisfying  $0 \leq R \leq 1$  is the mean resultant length of the data (the mean length of the combined phase vector in the Argand plane), and

$$\sigma = \sqrt{\ln\left(\frac{1}{R^2}\right)}, \quad (6)$$

for example, Mardia and Jupp (2000). We note in particular that the circular standard deviation (given in radians by Equation 6) relates to the width of the angular distribution and not to the accuracy to which the directional mean is determined. For the major events we find a directional mean  $\langle\Delta\Phi\rangle = 193.6^\circ$ , shown in the diagram as a red dashed line, with a circular standard deviation of  $\sigma = 60.3^\circ$ , while for the minor events we find  $\langle\Delta\Phi\rangle = 358.0^\circ$ , shown in the diagram as a green dashed line, with  $\sigma = 73.9^\circ$ . These phase intervals are further indicated by the pale red and green sectors in Figure 11, showing that there is a clear preference for the major events to occur during near antiphase conditions, while the minor events occur during near in phase conditions. Thus, while the compressed magnetospheric conditions required for such events to occur is set by the solar wind, the response to those conditions, whether resulting in strong PPO-modulated tail reconnection and flux closure or not, is significantly affected by the PPO beat phase. When the thickness of the plasma sheet is strongly modulated by the dual action of the two PPO systems, of comparable amplitude during the interval in question, that is, for PPO antiphase conditions, a strong response with extended generally PPO-modulated LFEs is observed, while when the plasma sheet is more weakly modulated due to the two systems acting in opposition to each other, that is, for PPO in phase conditions, a weaker response without extended LFEs is observed. Of course, the strength of the solar wind compression should also play some role, not readily accessible to study here given the availability only of model and proxy data on the concurrent state of the solar wind conditions upstream of Saturn's magnetosphere. Thus, on the one hand, it may be possible for compressions of sufficient strength to excite a “major” event irrespective of the PPO conditions prevailing, while on the other, sufficiently weak compressions should fail to produce such an event even under the most favorable beat phase conditions. In section 3.2 we noted an example where the magnetosphere appears to be in an entirely quiet expanded

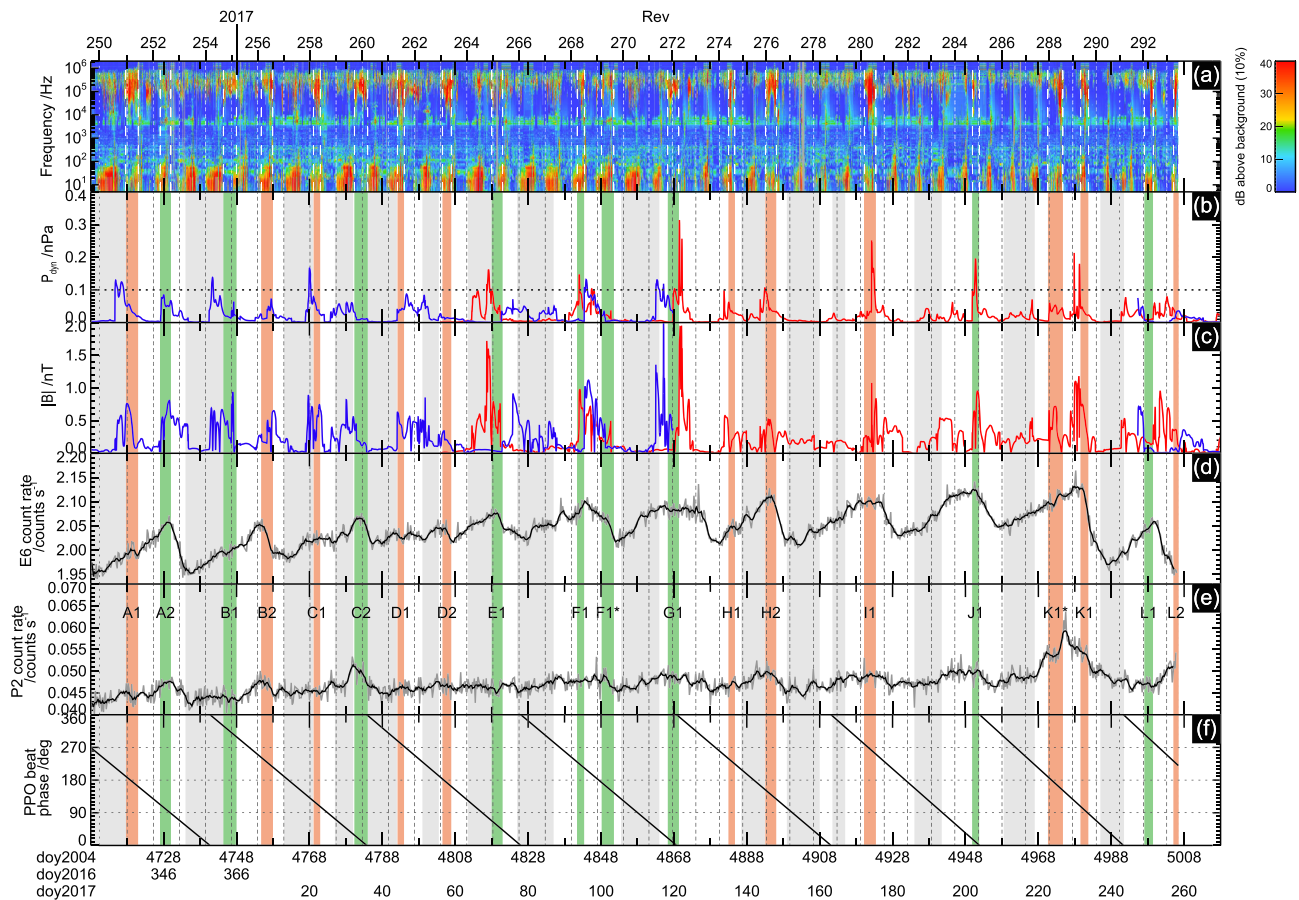


**Figure 12.** Overview of whole-interval results in a plot having a similar format to Figure 4. Figure 12a shows a RPWS spectrogram with the same frequency range and color scale as employed in Figures 5–10. Figures 12b–12e show model solar wind dynamic pressure (nPa), IMF strength (nT), LEMMS channel E6 count rate (GCR flux of >120 MeV protons), and LEMMS channel P2 count rate (GCR flux as well as SEP flux of 2.3–4.5 MeV protons), shown in the same format as Figures 4d–4g. Figure 12f shows the PPO beat phase (deg modulo 360°) defined by Equation 3. The superposed red- and green-shaded vertical bands (white dashed lines in Figure 12a) show intervals of magnetospheric compression defined by the times in Table 2, labeled as in Figure 4 and Tables 1 and 2. Red corresponds to major events with an extended LFE interval (longer than one planetary rotation) and green to minor events without such an extended LFE interval. The superposed gray-shaded vertical bands show intervals of relative magnetospheric quiet when energetic particle fluxes were at near-minimum values.

state under closely antiphase beat phase conditions (Figure 7, see also Figure S1). However, the results obtained here show that under typical conditions, the consequences of solar wind compression depend significantly on PPO beat phase.

Figure 12 provides an overview of results in a plot having a similar format to Figure 4. Figure 12a shows a RPWS spectrogram with the same frequency range and spectral power color scale as employed in Figures 5–10, though shown here with a greatly compressed timescale. Major SKR LFE events are evident as emission bursts (red) extending down to frequencies  $\sim 10$  kHz and below. Intervals of auroral hiss emission below  $\sim 100$  Hz near periapsis on each Rev are seen to be much longer on the F ring orbits than on the proximal orbits (beginning at Rev 271), this simply being due to the difference in orbit trajectories, with more time spent in the polar open field region of downward currents (relative to the ionosphere) on the F ring orbits than on the proximal orbits (see Figure 2). Figures 12b–12e show model solar wind dynamic pressure, IMF strength, LEMMS E6 count rate responding to the GCR flux (>120 MeV protons), and LEMMS P2 count rate responding weakly to the GCR flux as well as to the SEP flux (2.3–4.5 MeV protons), as shown previously in Figures 4d–4g. Figure 12f shows the PPO beat phase (modulo 360°) as given by Equation 3. The red and green shaded vertical bands superposed on these panels (white dashed lines in Figure 12a) show the compressed magnetosphere intervals defined by the start and stop times of each of the 20 events in Table 2, red for the major events and green for the minor events. These are labeled as in Figure 4, and in

Tables 1 and 2. The correspondence with the compression events anticipated using the model solar wind/IMF and GCR flux data in Table 1, described in section 2.4 and plotted using vertical dashed lines in Figure 4, is seen generally to be good, clearly corresponding with the Forbush decreases and related effects in the GCR flux profile, and with the model peaks in dynamic pressure/IMF strength. Comparing the timing of the observed events in Table 2 with the predicted times shown in Figure 4 and Table 1 based mainly on a judicious combination of model solar wind/IMF and GCR flux considerations, shows that the event center times agree well with expectation, with the center time minus the predicted time having a mean and SD of  $0.2 \pm 1.6$  days (ICME-related event L2 being excluded). Given the averaged 2.7 day event duration, this means that the event onsets typically occur somewhat before our predicted times, by a mean value and SD of  $\sim -1.1 \pm 1.6$  days. However, this difference seems hardly significant given the typical  $\sim \pm 1.5$  day timing uncertainties in the model SW/IMF data, combined with the 1.75 day smoothing in the GCR flux profiles. The majority of the events in this interval are clearly related to semirecurrent CIRs propagating in the heliosphere, though varying over the interval between one and two significant compressions per solar rotation. Two of the events, however, namely K1\* and final event L2, are associated with the impact of an interplanetary shock with an associated SEP signature, which certainly in the case of event L2 on Rev 293 is not CIR-related and may instead be associated with an X-class solar flare observed  $\sim 9$  days earlier (Roussos, Krupp, et al., 2018). Events F1 and F1\* are also of somewhat different nature, with event F1 occurring near a peak in GCR flux with following rather weak Forbush decrease onset, similar to many other events, while subsequent event F1\* relates to a further sharp increase in the rate of decline of the GCR flux occurring  $\sim 5$  days later. The relationship between the nature of the responses, whether major or minor, with the PPO beat phase is also evident in Figure 12f, with the major events mainly occurring within the intervals when the beat phase lies between  $90^\circ$  and  $270^\circ$  via  $180^\circ$  in the center of the panel, and the minor events occurring when the event lies outside that range, within the top and bottom segments of the panel.

Our examination of the Cassini data reveals not only the solar-modulated semirecurrent intervals of high activity related to magnetospheric compressions, however, but also the similarly semirecurrent intervals of magnetospheric quiet related to extended intervals of solar wind rarefaction. These intervals are marked by continuously low values of energetic particle fluxes throughout significant fractions of a week-long Rev (apart from the periapsis traversals of the inner radiation belts), indicative of cooler plasma in the nightside plasma sheet. Such conditions are exemplified by F ring Revs 253, 257, and 260 shown in Figures S4, 7, and 8, respectively, and by proximal Revs 275, 282, and 290 shown Figures S2, S1, and 9, respectively. These and other related intervals are indicated by the gray vertical bands in Figure 12, which show that they relate overall to rarefaction conditions in the model solar wind/IMF data, and usually to intervals in which the GCR flux is slowly increasing from minimum values following a Forbush decrease. Since such low-flux GCR conditions are typically observed on Revs directly following more active intervals during or following Forbush decreases when the plasma sheet energetic particle fluxes may be an order of magnitude higher, it is evident that the energetic ions and electrons associated with hot plasma are lost from the near-planet plasma sheet over Cassini orbital period intervals of  $\sim 1$  week (i.e., over  $\sim 15$  PR). This despite the fact that the overall plasma motion is dominated by rotation around the planet in this region of the plasma sheet out to  $\sim 20 R_S$  (e.g., Kane et al., 2020; Thomsen et al., 2014). It is also clear from the discussion of individual Revs in section 3, however, that following injection episodes observed, for example, on the inbound pass of a given Rev, such particles are retained within the plasma sheet in this region for at least several subsequent planetary rotations during outbound passes. We further note that while extended SKR LFEs do not occur under such rarefaction conditions, it should not be concluded that the SKR emissions are invariably weak during such intervals. In fact, initial examination indicates that PPO-modulated short-lived bursts of SKR with LFEs (e.g., Reed et al., 2019), possibly indicative of Vasyliunas-cycle activity, may be favored under such circumstances, such as can be seen during Rev 253 in Figure S4 and Rev 257 in Figures 7 and 8.

Finally, we note that on intervening Revs between compression intervals and quiet intervals associated with extended rarefactions, magnetospheric conditions are generally intermediate between minor storm and quiet time in nature, typically with sporadic PPO-modulated SKR emissions of moderate intensity, and intermediate levels of energetic particle fluxes. Short-interval PPO-modulated LFEs may occur, but extended LFEs are again absent. Examples may be found, for example, in Revs 279 and 281 in Figure 5, Revs 283 and 285 in Figure S1, and Rev 291 in Figure 9.

## 5. Summary

We have examined Cassini remote sensing and in situ data from the set of F ring and proximal orbits at the end of mission, augmented by HST auroral observations and model solar wind data, to investigate the state of Saturn's magnetosphere and its relation to concurrent heliospheric conditions. The nature of the study and its principal findings are summarized as follows.

- a. The Cassini F ring and proximal orbits explored the nightside tail to distances of  $\sim 21 R_S$  in the postmidnight to midnight sector, passing inbound from apoapsis through the northern outer plasma sheet/tail lobe region, and outbound through the southern and central plasma sheet region, via a variably close periapsis on the dayside. The very close similarity of both the sequence of twenty F ring orbits and the subsequent sequence of 22 and a half proximal orbits, is such that the Rev-to-Rev variations in observed parameters may be attributed dominantly to variations in the physical conditions prevailing, rather than to differences in orbit geometry. The spacecraft orbital period also corresponded quite closely to one quarter of the effective solar rotation period at Saturn of  $\sim 26$  days, such that four-Rev sequences of repetitive heliospheric conditions represent a first approximation, with  $\sim 11.5$  such sequences being observed over the  $\sim 10$  month interval of study. Heliospheric conditions inferred from model solar wind/IMF and Cassini GCR flux data evolved from the occurrence of two CIRs per solar rotation during the earlier F ring orbits to one CIR per rotation during the later F ring and proximal orbits (with one exception), this reflecting the late declining phase of the solar cycle. An ICME-related shock is also anticipated to have impacted on the final Rev, based on concurrent Cassini SEP flux data.
- b. Overall results demonstrate a very clear correspondence between in situ magnetospheric magnetic field and energetic particle data, together with remote sensing observations of SKR, auroral hiss, and auroral UV emissions, with the inferred simultaneous heliospheric conditions. A combination of model solar wind/IMF and GCR data thus provide an appropriate basis on which to develop such studies. Active intervals with, for example, strong SKR emissions and large energetic particle fluxes, are principally associated with CIR-related compression events, with one occurring every other Rev during the earlier F ring orbits when two such events occurred each solar rotation, and one every fourth Rev on the later F ring orbits and proximal orbits when one occurred each solar rotation (with one exception not including the ICME event).
- c. A clear response to anticipated compression events is almost invariably observed in the in situ and remote sensing data, which generally involve enhancements in the power and continuity of SKR emissions, compression and field deflection signatures in the residual meridional field components, and bursts or longer-lived enhancements in energetic particle fluxes, with anticorrelated variations in auroral hiss observed on polar tail lobe field lines. Individual compression-related disturbance intervals last on average for  $\sim 2.7$  days (typically  $\sim 2\text{--}3.5$  days), thus corresponding to approximately six Saturn planetary/PPO rotation periods, as well as to  $\sim 40\%$  of a Cassini orbital period and  $\sim 10\%$  of a solar rotation. Compression events are centered close to the times predicted from a combination principally of model solar wind/IMF and GCR flux considerations, with the center time minus the predicted time having a mean and SD of  $0.2 \pm 1.6$  days, such that the onsets occur on average  $\sim -1.2 \pm 1.6$  days before our predicted times. This difference is not considered significant, given the typical  $\sim \pm 1.5$  day uncertainties in the model SW/IMF data, and the  $\sim 2$  day smoothing of the GCR flux data. The detailed response in the in situ data depends, of course, on the orbit segment on which the compression event occurs. In particular, enhancements in energetic particle flux indicative of plasma heating within the near-tail plasma sheet are observed on the nearer-equatorial outbound passes, while PPO-modulated particle bursts and injections concurrent with field dipolarizations are typical on higher-latitude inbound passes.
- d. SKR effects vary considerably from event to event, sometimes involving only an enhancement in power and continuity relative to quiet intervals while maintaining a relatively narrow frequency band (e.g., Revs 254, Figure S4; 259, Figure 7; and 284, Figure S1), while on others also exhibiting major enhancements in power with LFEs indicative of significant strengthening of the associated field-aligned current densities (e.g., Revs 258, Figure 7; 274 and 276, Figure S2; 280, Figure 5; and 293, Figure 9). LFE events last on average for 1.2 days, corresponding to 2.7 planetary/PPO rotations (typically 2–3 planetary/PPO rotations), thus usually corresponding to a little less than half the overall duration of a compression event. Examination of responses observed on corresponding Revs on adjacent solar rotations with similar anticipated heliospheric conditions (e.g., Revs 278–281 with Revs



282–285 during the proximal orbit interval, Figures 5 and S1; and Revs 253–256 with Revs 257–260 during the F ring orbits, Figures 7 and S4) indicates that the PPO beat phase plays a role in determining the nature of the responses to a compression event. Defining “major” events to be those exhibiting an LFE interval lasting longer than one nominal planetary/PPO rotation period of 10.75 hr and minor events to be those without an LFE interval or having one lasting for one PPO period or less, we find a strong preference for major events to occur when the PPO beat phase lies within  $\sim 90^\circ$  of antiphase conditions, while minor events preferentially occur when the beat phase lies within  $\sim 90^\circ$  of in phase.

- e. Previous studies of tail field data (e.g., Cowley & Provan, 2017; Provan et al., 2012; Thomsen et al., 2017) have shown that the principal distinction between these two conditions is that for antiphase conditions the two PPO systems work in concert to maximally thin and thicken the tail plasma/current sheet during each PPO rotation cycle, destabilizing the sheet when it is thin, while for in phase conditions the thickening and thinning effects of the two systems are opposed in sense, and will approximately cancel given that the two PPO systems are of roughly equal amplitude during the interval of study. The onset of tail reconnection is thus favored for antiphase beat phase conditions at specific times in the PPO cycle when the plasma/current sheet is expected to be thin. In most cases we correspondingly find that SKR intensifications and LFE events begin close to the time in the PPO cycle when the north/south PPO phases are indicative of thin plasma sheet conditions, more specifically being governed by the phase of the moderately dominant northern PPO system under beat phase conditions nearer to quadrature (see Table 2). In some cases, but not all, the LFE onset directly follows a compression onset observed in the magnetic field data at the subsequent point in the PPO cycle favoring thin plasma sheet conditions (e.g., Revs 276, Figure S2; 280, Figure 5; 292 and 293, Figures 9 and 10).
- f. While UV auroral images are only sporadically available from UVIS and the HST during these Revs, examination shows that both major and minor compression events are generally associated with a contraction of the auroral oval (see Table 2). A few well observed major events, in particular, show a strongly contracted oval with a dawn maximum in brightness, indicating closure by tail reconnection of a significant fraction of preexisting open lobe flux. This shows that these events are associated with a response to solar wind conditions which is of global scale and consequences within the magnetosphere. Well-observed examples include those associated with Revs 258 (Figure 7), 280 (Figure 5), and 293 (Figure 9), the latter comprising a major auroral storm associated with the ICME shock impact on the final inbound pass. Additional less well-observed examples occur within the wider data set, such as on Revs 261 and 271/272.
- g. Under several-day solar wind rarefaction conditions, usually following Forbush decrease minima in GCR flux, in situ and remote sensing data indicate the presence of a quiet magnetosphere without major tail dynamics of the above nature. These conditions typically occur over several day (approximately one Cassini Rev) intervals generally once or twice per solar rotation, thus every other or every fourth Rev. Plasma sheet energetic particle fluxes are usually the weakest of those observed on the F ring and proximal Revs, indicative of the presence of cooler plasma (e.g., Revs 253, Figure S4; 282, Figure S1; and 290, Figure 9). Auroral images generally indicate the presence of an auroral oval of usual relatively expanded size, with relatively weak emissions often without a maximum in the dawn sector. SKR emissions are also generally weak and more sporadic, without extended LFEs, but usually with vestiges of PPO-related modulations. In some cases, however, prominent short-lived PPO-modulated multiple LFEs may occur on these Revs (e.g., Revs 250, 253, Figure S4; and 257, Figures 7 and 8), indicative of the occurrence under these conditions of PPO-modulated Vasyliunas-cycle activity.

## Data Availability Statements

The UV observations were obtained from the ESA/NASA Hubble Space Telescope GO program 14811. The original data can be retrieved from the MAST archive at <https://archive.stsci.edu/access-mast-data>, and the processed data from the APIS service (<http://apis.obspm.fr>). The Cassini/RPWS and MAG original data are accessible through the PDS archive (<https://pds.nasa.gov/>). Calibrated data from the Cassini mission are available from the NASA Planetary Data System at the Jet Propulsion Laboratory (<https://pds.jpl.nasa.gov/>).



## Acknowledgments

Work at Leicester was supported by STFC Consolidated Grant ST/N000749/1. T. J. B. was supported by STFC Quota Studentship ST/N504117/1, and E. J. B. by a Royal Society Wolfson Research Merit Award. L. L. was supported by CNES and PNP/PNST programs of CNRS/INSU. M. K. D. and G. J. H. were supported by UKRI/STFC Grant ST/N000692/1.

## References

- Agiwal, O., Hunt, G. J., Dougherty, M. K., Cowley, S. W. H., & Provan, G. (2020). Modeling the temporal variability in Saturn's magnetotail current sheet from the Cassini F ring orbits. *Journal of Geophysical Research: Space Physics*, 125, e2019JA027371. <https://doi.org/10.1002/2019JA027371>
- Andrews, D. J., Coates, A. J., Cowley, S. W. H., Dougherty, M. K., Lamy, L., Provan, G., & Zarka, P. (2010). Magnetospheric period oscillations at Saturn: Comparison of equatorial and high-latitude magnetic field periods with north and south SKR periods. *Journal of Geophysical Research*, 115, A12252. <https://doi.org/10.1029/2010JA015666>
- Armstrong, T. P., Taherion, S., Manweiler, J., Krimigis, S., Paranicas, C., Mitchell, D., & Krupp, N. (2009). Energetic ions trapped in Saturn's inner magnetosphere. *Planetary and Space Science*, 57, 1723–1731. <https://doi.org/10.1016/j.pss.2009.03.008>
- Arridge, C. S., André, N., Khurana, K. K., Russell, C. T., Cowley, S. W. H., Provan, G., et al. (2011). Periodic motion of Saturn's nightside plasma sheet. *Journal of Geophysical Research*, 116, A11205. <https://doi.org/10.1029/2011JA016827>
- Arridge, C. S., Khurana, K. K., Russell, C. T., Southwood, D. J., Achilleos, N., Dougherty, M. K., et al. (2008). Warping of Saturn's magnetospheric and magnetotail current sheets. *Journal of Geophysical Research*, 113, A08217. <https://doi.org/10.1029/2007JA012963>
- Azari, A. R., Jia, X., Liemohn, M. W., Hospodarsky, G. B., Provan, G., Ye, S. Y., et al. (2019). Are Saturn's interchange injections organized by rotational longitude? *Journal of Geophysical Research: Space Physics*, 124, 1806–1822. <https://doi.org/10.1002/2018JA026196>
- Bader, A., Badman, S. V., Cowley, S. W. H., Yao, Z. H., Ray, L. C., Kinrade, J., et al. (2019). The dynamics of Saturn's main auroras. *Geophysical Research Letters*, 46, 10,283–10,294. <https://doi.org/10.1029/2019GL084620>
- Bader, A., Badman, S. V., Kinrade, J., Cowley, S. W. H., Provan, G., & Pryor, W. R. (2019). Modulations of Saturn's UV auroral oval location by planetary period oscillations. *Journal of Geophysical Research: Space Physics*, 124, 952–970. <https://doi.org/10.1002/2018JA026117>
- Bader, A., Badman, S. V., Yao, Z. H., Kinrade, J., & Pryor, W. R. (2019). Observations of continuous quasiperiodic auroral pulsations on Saturn in high time-resolution UV auroral imagery. *Journal of Geophysical Research: Space Physics*, 124, 2451–2465. <https://doi.org/10.1029/2018JA026320>
- Badman, S. V., Bunce, E. J., Clarke, J. T., Cowley, S. W. H., Gérard, J.-C., Grodent, D., & Milan, S. E. (2005). Open flux estimates in Saturn's magnetosphere during the January 2004 Cassini-HST campaign, and implications for reconnection rates. *Journal of Geophysical Research*, 110, A11216. <https://doi.org/10.1029/2005JA011240>
- Badman, S. V., & Cowley, S. W. H. (2007). Significance of Dungey cycle flows in Jupiter's and Saturn's magnetospheres, and their identification on closed equatorial field lines. *Annales Geophysicae*, 25, 941–951.
- Badman, S. V., Cowley, S. W. H., Cecconi, B., Lamy, L., & Zarka, P. (2008). Relationship between solar wind corotating interaction regions and the phasing and intensity of Saturn kilometric radiation bursts. *Annales Geophysicae*, 26, 3641–3651.
- Badman, S. V., Jackman, C. M., Nichols, J. D., Clarke, J. T., & Gérard, J.-C. (2014). Open flux in Saturn's magnetosphere. *Icarus*, 231, 137–145. <https://doi.org/10.1016/j.icarus.2013.12.004>
- Badman, S. V., Masters, A., Hasegawa, H., Fujimoto, M., Radioti, A., Grodent, D., et al. (2013). Bursty magnetic reconnection at Saturn's magnetopause. *Geophysical Research Letters*, 40, 1027–1031. <https://doi.org/10.1002/grl.50199>
- Badman, S. V., Provan, G., Bunce, E. J., Mitchell, D. G., Melin, H., Cowley, S. W. H., et al. (2016). Saturn's auroral morphology and field-aligned currents during a solar wind compression. *Icarus*, 263, 83–93. <https://doi.org/10.1016/j.icarus.2014.11.014>
- Bagenal, F., & Delamere, P. A. (2011). Flow of mass and energy in the magnetospheres of Jupiter and Saturn. *Journal of Geophysical Research*, 116, A05209. <https://doi.org/10.1029/2010JA016294>
- Boudouridis, A., Zesta, E., Lyons, L. R., Anderson, P. C., & Lummerzheim, D. (2004). Magnetospheric reconnection driven by solar wind pressure fronts. *Annales Geophysicae*, 22, 1367–1378.
- Bradley, T. J., Cowley, S. W. H., Bunce, E. J., Smith, A. W., Jackman, C. M., & Provan, G. (2018). Planetary period modulation of reconnection bursts in Saturn's magnetotail. *Journal of Geophysical Research: Space Physics*, 123, 9476–9507. <https://doi.org/10.1029/2018JA025932>
- Bunce, E. J., Cowley, S. W. H., Alexeev, I. I., Arridge, C. S., Dougherty, M. K., Nichols, J. D., & Russell, C. T. (2007). Cassini observations of the variation of Saturn's ring current parameters with system size. *Journal of Geophysical Research*, 112, A10202. <https://doi.org/10.1029/2007JA012275>
- Bunce, E. J., Cowley, S. W. H., Jackman, C. M., Clarke, J. T., Cray, F. J., & Dougherty, M. K. (2006). Cassini observations of the interplanetary medium upstream of Saturn and their relation to Hubble Space Telescope auroral data. *Advances in Space Research*, 38, 806–814. <https://doi.org/10.1016/j.asr.2005.08.005>
- Bunce, E. J., Cowley, S. W. H., Talboys, D. L., Dougherty, M. K., Lamy, L., Kurth, W. S., et al. (2010). Extraordinary field-aligned current signatures in Saturn's high-latitude magnetosphere: Analysis of Cassini data during Revolution 89. *Journal of Geophysical Research*, 115, A10238. <https://doi.org/10.1029/2010JA015612>
- Bunce, E. J., Cowley, S. W. H., Wright, D. M., Coates, A. J., Dougherty, M. K., Krupp, N., et al. (2005). In situ observations of a solar wind compression-induced hot plasma injection in Saturn's tail. *Geophysical Research Letters*, 32, L20S04. <https://doi.org/10.1029/2005GL022888>
- Cane, H. V., Reames, D. V., & von Rosenvinge, T. T. (1988). The role of interplanetary shocks in the longitude distribution of solar energetic particles. *Journal of Geophysical Research*, 93, 9555–9567. <https://doi.org/10.1029/JA093iA09p09555>
- Carbary, J., Hedman, M., Hill, T., Jia, X., Kurth, W., Lamy, L., & Provan, G. (2018). The mysterious periodicities of Saturn: Clues to the rotation rate of the planet, Saturn in the 21st Century. In Baines, K., Flasar, F., Krupp, N., & Stallard, T. (Eds.), *Cambridge Planetary Science* (pp. 97–125). Cambridge: Cambridge University Press. <https://doi.org/10.1017/9781316227220.005>
- Carbary, J. F., Mitchell, D. G., Brandt, P., Roelof, E. C., & Krimigis, S. M. (2008). Periodic tilting of Saturn's plasma sheet. *Geophysical Research Letters*, 35, L24101. <https://doi.org/10.1029/2008GL036339>
- Carbary, J. F., Sergis, N., Mitchell, D. G., & Krupp, N. (2015). Saturn's hinge parameter from Cassini magnetotail passes in 2013–2014. *Journal of Geophysical Research: Space Physics*, 120, 4438–4445. <https://doi.org/10.1002/2015JA021152>
- Chen, Y., Hill, T. W., Rymer, A. M., & Wilson, R. J. (2010). Rate of radial transport of plasma in Saturn's inner magnetosphere. *Journal of Geophysical Research*, 115, A10211. <https://doi.org/10.1029/2010JA015412>
- Clarke, J. T., Gérard, J.-C., Grodent, D., Wannawichian, S., Gustin, J., Connerney, J., et al. (2005). Morphological differences between Saturn's ultraviolet auroras and those of Earth and Jupiter. *Nature*, 433, 717–719.
- Clarke, J. T., Nichols, J. D., Gérard, J.-C., Grodent, D., Hansen, K. C., Kurth, W. S., et al. (2009). The response of Jupiter's and Saturn's auroral activity to the solar wind. *Journal of Geophysical Research*, 114, A05210. <https://doi.org/10.1029/2008JA013694>

- Cowley, S. W. H., Badman, S. V., Bunce, E. J., Clarke, J. T., Gérard, J.-C., Grodent, D., et al. (2005). Reconnection in a rotation-dominated magnetosphere and its relation to Saturn's auroral dynamics. *Journal of Geophysical Research*, 110, A02201. <https://doi.org/10.1029/2004JA010796>
- Cowley, S. W. H., Bunce, E. J., & Prangé, R. (2004). Saturn's polar ionospheric flows and their relation to the main auroral oval. *Annales Geophysicae*, 22, 1379–1394.
- Cowley, S. W. H., Nichols, J. D., & Jackman, C. M. (2015). Down-tail mass loss by plasmoids in Jupiter's and Saturn's magnetospheres. *Journal of Geophysical Research: Space Physics*, 120, 6347–6356. <https://doi.org/10.1002/2015JA021500>
- Cowley, S. W. H., & Provan, G. (2017). Planetary period modulations of Saturn's magnetotail current sheet during northern spring: Observations and modeling. *Journal of Geophysical Research: Space Physics*, 122, 6049–6077. <https://doi.org/10.1002/2017JA023993>
- Cowley, S. W. H., Provan, G., Hunt, G. J., & Jackman, C. M. (2017). Planetary period modulations of Saturn's magnetotail current sheet: A simple illustrative mathematical model. *Journal of Geophysical Research: Space Physics*, 122, 258–279. <https://doi.org/10.1002/2016JA023367>
- Desch, M. D. (1982). Evidence for solar wind control of Saturn's radio emission. *Journal of Geophysical Research*, 87, 4549–4554.
- Desch, M. D., & Rucker, H. O. (1983). The relationship between Saturn kilometric radiation and the solar wind. *Journal of Geophysical Research*, 88, 8999–9006.
- Dougherty, M. K., Kellock, S., Southwood, D. J., Balogh, A., Smith, E. J., Tsurutani, B. T., et al. (2004). The Cassini magnetic field investigation. *Space Science Reviews*, 114, 331–383. [https://doi.org/10.1007/978-1-4020-2774-1\\_4](https://doi.org/10.1007/978-1-4020-2774-1_4)
- Dungey, J. W. (1961). Interplanetary field and the auroral zones. *Physical Review Letters*, 6, 47–48.
- Fuselier, S. A., Frahm, R., Lewis, W. S., Masters, A., Mukherjee, J., Petrinec, S. M., & Sillanpää, I. J. (2014). The location of magnetic reconnection at Saturn's magnetopause: A comparison with Earth. *Journal of Geophysical Research: Space Physics*, 119, 2563–2578. <https://doi.org/10.1002/2013JA019684>
- Gérard, J.-C., Bonfond, B., Gustin, J., Grodent, D., Clarke, J. T., Bisikalo, D., & Shematovich, V. (2009). Altitude of Saturn's aurora and its implications for the characteristic energy of precipitated electrons. *Geophysical Research Letters*, 36, L02202. <https://doi.org/10.1029/2008GL036554>
- Grodent, D., Gérard, J.-C., Cowley, S. W. H., Bunce, E. J., & Clarke, J. T. (2005). Variable morphology of Saturn's southern ultraviolet aurora. *Journal of Geophysical Research*, 110, A07215. <https://doi.org/10.1029/2004JA010983>
- Gurnett, D. A., Kurth, W. S., Kirchner, D. L., Hospodarsky, G. B., Averkamp, T. F., Zarka, P., et al. (2004). The Cassini radio and plasma wave investigation. *Space Sci Rev*, 114(1–4), 395–463. <https://doi.org/10.1007/s11214-004-1434-0>
- Gurnett, D. A., Lecacheux, A., Kurth, W. S., Persoon, A. M., Groene, J. B., Lamy, L., et al. (2009). Discovery of a north-south asymmetry in Saturn's radio rotation period. *Geophysical Research Letters*, 36, L16102. <https://doi.org/10.1029/2009GL039621>
- Gurnett, D. A., Persoon, A. M., Kopf, A. J., Kurth, W. S., Morooka, M. W., Wahlund, J.-E., et al. (2010). A plasmopause-like density boundary at high latitudes in Saturn's magnetosphere. *Geophysical Research Letters*, 37, L16806. <https://doi.org/10.1029/2010GL044466>
- Gustin, J., Grodent, D., Radioti, A., Pryor, W., Lamy, L., & Ajello, J. (2017). Statistical study of Saturn's auroral electron properties with Cassini/UVIS FUV spectral images. *Icarus*, 284, 264–283. <https://doi.org/10.1016/j.icarus.2016.11.017>
- Gustin, J., Grodent, D., Ray, L., Bonfond, B., Bunce, E., Nichols, J., & Ozak, N. (2016). Characteristics of north Jovian aurora from STIS FUV spectral images. *Icarus*, 268, 215–241. <https://doi.org/10.1016/j.icarus.2015.12.048>
- Hill, T. W., Thomsen, M. F., Henderson, M. G., Tokar, R. L., Coates, A. J., McAndrews, H. J., et al. (2008). Plasmoids in Saturn's magnetotail. *Journal of Geophysical Research*, 113, A01214. <https://doi.org/10.1029/2007JA012626>
- Hunt, G. J., Cowley, S. W. H., Provan, G., Bunce, E. J., Alexeev, I. I., Belenkaya, E. S., et al. (2014). Field-aligned currents in Saturn's southern nightside magnetosphere: Subcorotation and planetary period oscillation components. *Journal of Geophysical Research: Space Physics*, 119, 9847–9899. <https://doi.org/10.1002/2014JA020506>
- Hunt, G. J., Cowley, S. W. H., Provan, G., Bunce, E. J., Alexeev, I. I., Belenkaya, E. S., et al. (2015). Field-aligned currents in Saturn's northern nightside magnetosphere: Evidence for inter-hemispheric current flow associated with planetary period oscillations. *Journal of Geophysical Research: Space Physics*, 120, 7552–7584. <https://doi.org/10.1002/2014JA021454>
- Hunt, G. J., Provan, G., Cowley, S. W. H., Dougherty, M. K., & Southwood, D. J. (2018). Saturn's planetary period oscillations during the closest approach of Cassini's ring-grazing orbits. *Geophysical Research Letters*, 45, 4692–4700. <https://doi.org/10.1029/2018GL077925>
- Jackman, C. J., Arridge, C. S., Krupp, N., Bunce, E. J., Mitchell, D. G., McAndrews, H. J., et al. (2008). A multi-instrument view of tail reconnection at Saturn. *Journal of Geophysical Research*, 113, A11213. <https://doi.org/10.1029/2008JA013592>
- Jackman, C. J., Slavin, J. A., & Cowley, S. W. H. (2011). Cassini observations of plasmoid structure and dynamics: Implications for the role of magnetic reconnection in magnetospheric circulation at Saturn. *Journal of Geophysical Research*, 116, A10212. <https://doi.org/10.1029/2011JA016682>
- Jackman, C. J., Slavin, J. A., Kivelson, M. G., Southwood, D. J., Achilleos, N., Thomsen, M. F., et al. (2014). Saturn's dynamic magnetotail: A comprehensive magnetic field and plasma survey of plasmoids and traveling compression regions and their role in global magnetospheric dynamics. *Journal of Geophysical Research: Space Physics*, 119, 5465–5494. <https://doi.org/10.1002/2013JA019388>
- Jackman, C. J., Thomsen, M. F., Mitchell, D. G., Sergis, N., Arridge, C. S., Felici, M., et al. (2015). Field dipolarization in Saturn's magnetotail with planetward ion flows and energetic particle flow bursts: Evidence of quasi-steady reconnection. *Journal of Geophysical Research: Space Physics*, 120, 3603–3617. <https://doi.org/10.1002/2015JA020995>
- Jackman, C. M., Achilleos, N., Bunce, E. J., Cecconi, B., Clarke, J. T., Cowley, S. W. H., et al. (2005). Interplanetary conditions and magnetospheric dynamics during the Cassini orbit insertion fly-through of Saturn's magnetosphere. *Journal of Geophysical Research*, 110, A10212. <https://doi.org/10.1029/2005JA011054>
- Jackman, C. M., Achilleos, N., Bunce, E. J., Cowley, S. W. H., Dougherty, M. K., Jones, G. H., et al. (2004). Interplanetary magnetic field at <9 AU during the declining phase of the solar cycle and its implications for Saturn's magnetospheric dynamics. *Journal of Geophysical Research*, 109, A11203. <https://doi.org/10.1029/2004JA010614>
- Jackman, C. M., Achilleos, N., Cowley, S. W. H., Bunce, E. J., Radioti, A., Grodent, D., et al. (2013). Auroral counterpart of magnetic field dipolarizations in Saturn's tail. *Planetary and Space Science*, 82, 34–42.
- Jackman, C. M., Lamy, L., Freeman, M. P., Zarka, P., Cecconi, B., Kurth, W. S., et al. (2009). On the character and distribution of lower-frequency radio emissions at Saturn and their relationship to substorm-like events. *Journal of Geophysical Research*, 114, A08211. <https://doi.org/10.1029/2008JA013997>
- Jackman, C. M., Provan, G., & Cowley, S. W. H. (2016). Reconnection events in Saturn's magnetotail: Dependence of plasmoid occurrence on planetary period oscillation phase. *Journal of Geophysical Research: Space Physics*, 121, 2922–2934. <https://doi.org/10.1002/2015JA021985>

- Jasinski, J. M., Arridge, C. S., Bader, A., Smith, A., Felici, M., Kinrade, J., et al. (2019). Saturn's open-closed field line boundary: A Cassini electron survey at Saturn's magnetosphere. *Journal of Geophysical Research: Space Physics*, 124, 10,018–10,035. <https://doi.org/10.1029/2019JA027090>
- Jasinski, J. M., Arridge, C. S., Lamy, L., Leisner, J. S., Thomsen, M. F., Mitchell, D. G., et al. (2014). Cusp observation at Saturn's high-latitude magnetosphere by the Cassini spacecraft. *Geophysical Research Letters*, 41, 1382–1388. <https://doi.org/10.1002/2014GL059319>
- Jasinski, J. M., Slavin, J. A., Arridge, C. S., Poh, G., Jia, X., Sergis, N., et al. (2016). Flux transfer event observation at Saturn's dayside magnetopause by the Cassini spacecraft. *Geophysical Research Letters*, 43, 6713–6723. <https://doi.org/10.1002/2016GL069260>
- Jia, X., Kivelson, M. G., & Gombosi, T. I. (2012). Driving Saturn's magnetospheric periodicities from the upper atmosphere/ionosphere. *Journal of Geophysical Research*, 117, A04215. <https://doi.org/10.1029/2011JA017367>
- Jinks, S. L., Bunce, E. J., Cowley, S. W. H., Provan, G., Yeoman, T. K., Arridge, C. S., et al. (2014). Cassini multi-instrument assessment of Saturn's polar cap boundary. *Journal of Geophysical Research*, 119, 8161–8177. <https://doi.org/10.1029/2013JA020367>
- Kaiser, M. L., & Desch, M. D. (1984). Radio emissions from the planets Earth, Jupiter, and Saturn. *Reviews of Geophysics*, 22, 373–384. <https://doi.org/10.1029/RG022i004p00373>
- Kane, M., Mitchell, D. G., Carbary, J. F., Dyalynas, K., Hill, M. E., & Krimigis, S. M. (2020). Convection in the magnetosphere of Saturn during the Cassini mission derived from MIMI INCA and CHEMS measurements. *Journal of Geophysical Research: Space Physics*, 125, in press. <https://doi.org/10.1002/2019JA027534>
- Kellett, S., Arridge, C. S., Bunce, E. J., Coates, A. J., Cowley, S. W. H., Dougherty, M. K., et al. (2011). Saturn's ring current: Local time dependence and temporal variability. *Journal of Geophysical Research*, 116, A05220. <https://doi.org/10.1029/2010JA016216>
- Kinrade, J., Badman, S. V., Paranicas, C., Mitchell, D. G., Arridge, C. S., Gray, R. L., et al. (2020). Tracking counterpart signatures in Saturn's auroras and ENA imagery during large-scale plasma injection events. *Journal of Geophysical Research: Space Physics*, 125, e2019JA027542. <https://doi.org/10.1002/2019JA027542>
- Kivelson, M. G., & Southwood, D. J. (2005). Dynamical consequences of two modes of centrifugal instability in Jupiter's outer magnetosphere. *Journal of Geophysical Research*, 110, A12209. <https://doi.org/10.1029/2005JA011176>
- Kopf, A. J., Gurnett, D. A., Menietti, J. D., Schippers, P., Arridge, C. S., Hospodarski, G. B., et al. (2010). Electron beams as the source of whistler-mode auroral hiss at Saturn. *Geophysical Research Letters*, 37, L09102. <https://doi.org/10.1029/2010GL042980>
- Kotova, A., Roussos, E., Krupp, N., & Dandouras, I. (2015). Modeling of the energetic ion observations in the vicinity of Rhea and Dione. *Icarus*, 258, 402–417. <https://doi.org/10.1016/j.icarus.2015.06.031>
- Krimigis, S. M., Mitchell, D. G., Hamilton, D. C., Livi, S., Dandouras, J., Jaskulek, S., et al. (2004). Magnetosphere Imaging Instrument (MIMI) on the Cassini Mission to Saturn/Titan. *Space Science Reviews*, 114, 233–329. <https://doi.org/10.1029/10.1007/s11214-004-1410-8>
- Kurth, W. S., Gurnett, D. A., Clarke, J. T., Zarka, P., Desch, M. D., Kaiser, M. L., et al. (2005). An Earth-like correspondence between Saturn's auroral features and radio emissions. *Nature*, 433, 722–725.
- Kurth, W. S., Hospodarsky, G. B., Gurnett, D. A., Lamy, L., Dougherty, M. K., Nichols, J., et al. (2015). Saturn kilometric radiation intensities during the Saturn auroral campaign of 2013. *Icarus*, 263, 2–9. <https://doi.org/10.1016/j.icarus.2015.01.003>
- Lamy, L. (2017). The Saturnian kilometric radiation before the Cassini Grand Finale. In Fischer, G., et al. (Eds.), *Planetary radio emissions, VI* (pp. 171–190). Vienna: Austrian Academy of Sciences Press.
- Lamy, L., Cecconi, B., Prangé, R., Zarka, P., Nichols, J. D., & Clarke, J. T. (2009). An auroral oval at the footprint of Saturn's kilometric radio sources, colocated with the UV aurorae. *Journal of Geophysical Research*, 114, A10212. <https://doi.org/10.1029/2009JA014401>
- Lamy, L., Cecconi, B., Zarka, P., Canu, P., Schippers, P., Kurth, W. S., et al. (2011). Emission and propagation of Saturn kilometric radiation: Magnetoionic modes, beaming pattern, and polarization state. *Journal of Geophysical Research*, 116(A4), A04212. <https://doi.org/10.1029/2010JA016195>
- Lamy, L., Prangé, R., Pryor, W., Gustin, J., Badman, S. V., Melin, H., et al. (2013). Multispectral diagnosis of Saturn's auroras throughout a planetary rotation. *Journal of Geophysical Research: Space Physics*, 118, 4817–4843. <https://doi.org/10.1002/jgra.50404>
- Lamy, L., Prangé, R., Tao, C., Kim, T., Badman, S. V., Zarka, P., et al. (2018). Saturn's northern auroras at solstice from HST observations coordinated with Cassini's grand finale. *Geophysical Research Letters*, 45, 9353–9362. <https://doi.org/10.1029/2018GL078211>
- Lamy, L., Schippers, P., Zarka, P., Cecconi, B., Arridge, C. S., Dougherty, M. K., et al. (2010). Properties of Saturn kilometric radiation measured within its source region. *Geophysical Research Letters*, 37, L12104. <https://doi.org/10.1029/2010GL043415>
- Liu, X., & Hill, T. W. (2012). Effects of finite pressure on centrifugally driven convection in Saturn's inner magnetosphere. *Journal of Geophysical Research*, 117, A07216. <https://doi.org/10.1029/2012JA017827>
- Liu, X., Hill, T. W., Wolf, R. A., Sazykin, S., Spiro, R. W., & Wu, H. (2010). Numerical simulation of plasma transport in Saturn's inner magnetosphere using the Rice Convection Model. *Journal of Geophysical Research*, 115, A12254. <https://doi.org/10.1029/2010JA015859>
- Lockwood, J. A. (1971). Forbush decreases in the cosmic radiation. *Space Science Reviews*, 12, 658–715. <https://doi.org/10.1007/BF00173346>
- Mardia, K. V., & Jupp, P. E. (2000). *Directional Statistics*. Chichester, UK: J. Wiley and Sons Ltd.
- Menietti, J. D., Palmaerts, B., Zaslava, J., Averkamp, T. F., Groene, J. B., & Kurth, W. S. (2020). Quasiperiodic Saturn auroral hiss observed during a Cassini proximal orbit. *Journal of Geophysical Research: Space Physics*, 125, e2019JA027338. <https://doi.org/10.1029/2019JA027338>
- Meredith, C. J., Alexeev, I. I., Badman, S. V., Belenkaya, E. S., Cowley, S. W. H., Dougherty, M. K., et al. (2014). Saturn's dayside UV auroras: Evidence for morphological dependence on the direction of the upstream interplanetary magnetic field. *Journal of Geophysical Research: Space Physics*, 119, 1994–2008. <https://doi.org/10.1002/2013JA019598>
- Meredith, C. J., Cowley, S. W. H., & Nichols, J. D. (2014). Survey of Saturn auroral storms observed by the Hubble Space Telescope: Implications for storm time scales. *Journal of Geophysical Research: Space Physics*, 119, 9624–9642. <https://doi.org/10.1002/2014JA020601>
- Mitchell, D. G., Brandt, P. C., Roelof, E. C., Dandouras, J., Krimigis, S. M., Mauk, B. H., et al. (2005). Energetic ion acceleration in Saturn's magnetotail: Substorms at Saturn? *Geophysical Research Letters*, 32, L20S01. <https://doi.org/10.1029/2005GL022647>
- Mitchell, D. G., Krimigis, S. M., Paranicas, C. P., Brandt, P. C., Carbary, J. F., Roelof, E. C., et al. (2009). Recurrent energization of plasma in the midnight-to-dawn quadrant of Saturn's magnetosphere, and its relationship ion to auroral UV and radio. *Planetary and Space Science*, 57, 1732–1742. <https://doi.org/10.1016/j.pss.2009.04.002>
- Morooka, M. W., Modolo, R., Wahlund, J.-E., André, M., Eriksson, A. I., Persoon, A. M., et al. (2009). The electron density of Saturn's magnetosphere. *Annales Geophysicae*, 27, 2971–2991.
- Nakamura, Y., Kasaba, Y., Kimura, T., Lamy, L., Cecconi, B., Fischer, G., et al. (2019). Seasonal variation of north-south asymmetry in the intensity of Saturn kilometric radiation from 2004 to 2017. *Planetary and Space Science*, 178, 104711. <https://doi.org/10.1016/j.pss.2019.104711>



- Nichols, J. D., Badman, S. V., Baines, K. H., Brown, R. H., Bunce, E. J., Clarke, J. T., et al. (2014). Dynamic auroral storms on Saturn as observed by the Hubble Space Telescope. *Geophysical Research Letters*, *41*, 3323–3330. <https://doi.org/10.1002/2014GL060186>
- Palmaerts, B., Radioti, A., Grodent, D., Yao, Z. H., Bradley, T. J., Roussos, E., et al. (2018). Auroral storm and polar arcs at Saturn—Final Cassini/UVIS auroral observations. *Geophysical Research Letters*, *45*, 6832–6842. <https://doi.org/10.1002/2018GL078094>
- Prangé, R., Pallier, L., Hansen, K. C., Howard, R., Vourladis, A., Courtin, R., & Parkinson, C. (2004). An interplanetary shock traced by planetary auroral storms from the Sun to Saturn. *Nature*, *432*, 78–81. <https://doi.org/10.1038/nature02986>
- Provan, G., Andrews, D. J., Arridge, C. S., Coates, A. J., Cowley, S. W. H., Cox, G., et al. (2012). Dual periodicities in planetary-period magnetic field oscillations in Saturn's tail. *Journal of Geophysical Research*, *117*, A01209. <https://doi.org/10.1029/2011JA017104>
- Provan, G., Cowley, S. W. H., Bradley, T. J., Bunce, E. J., Hunt, G. J., Cao, H., & Dougherty, M. K. (2019). Magnetic field observations on Cassini's proximal periapsis passes: Planetary period oscillations and mean residual fields. *Journal of Geophysical Research: Space Physics*, *124*, 8814–8864. <https://doi.org/10.1002/2019JA026800>
- Provan, G., Cowley, S. W. H., Bradley, T. J., Bunce, E. J., Hunt, G. J., & Dougherty, M. K. (2018). Planetary period oscillations in Saturn's magnetosphere: Cassini magnetic field observations over the northern summer solstice interval. *Journal of Geophysical Research: Space Physics*, *123*, 3859–3899. <https://doi.org/10.1029/2018JA025237>
- Provan, G., Lamy, L., Cowley, S. W. H., & Bunce, E. J. (2019). Planetary period oscillations in Saturn's magnetosphere: Comparison of magnetic and SKR modulation periods and phases during northern summer to the end of the Cassini mission. *Journal of Geophysical Research: Space Physics*, *124*, 1157–1172. <https://doi.org/10.1029/2018JA026079>
- Radioti, A., Grodent, D., Gérard, J.-C., Milan, S. E., Bonfond, B., Gustin, J., & Pryor, W. (2011). Bifurcations of the main auroral ring at Saturn: Ionospheric signatures of consecutive reconnection events at the magnetopause. *Journal of Geophysical Research*, *116*, A11209. <https://doi.org/10.1029/2011JA016661>
- Radioti, A., Grodent, D., Jia, X., Gérard, J.-C., Bonfond, B., Pryor, W., et al. (2016). A multi-scale magnetotail reconnection event at Saturn and associated flows: Cassini/UVIS observations. *Icarus*, *263*, 75–82. <https://doi.org/10.1016/j.icarus.2014.12.016>
- Reed, J. J., Jackman, C. M., Lamy, L., Kurth, W. S., & Whiter, D. K. (2018). Low-frequency extensions of the Saturn kilometric radiation as a proxy for magnetospheric dynamics. *Journal of Geophysical Research: Space Physics*, *123*, 443–463. <https://doi.org/10.1002/2017JA024499>
- Roussos, E., Jackman, C. M., Thomsen, M. F., Kurth, W. S., Badman, S. V., Paranicas, C., et al. (2018). Solar energetic particles (SEP) and galactic cosmic rays (GCR) as tracers of solar wind conditions near Saturn: Event lists and applications. *Icarus*, *300*, 47–71. <https://doi.org/10.1016/j.icarus.2017.08.040>
- Roussos, E., Krupp, N., Dialynas, K., Kollmann, P., Paranicas, C., Echer, E., et al. (2019). Jovian cosmic-ray protons in the heliosphere: Constraints by Cassini observations. *The Astrophysical Journal*, *871*, 223. <https://doi.org/10.3847/1538-4357/aafb2f>
- Roussos, E., Krupp, N., Paranicas, C., Kollmann, P., Mitchell, D. G., Krimigis, S. M., et al. (2018). Heliospheric conditions at Saturn during Cassini's ring-grazing and proximal orbits. *Geophysical Research Letters*, *45*, 10,812–10,818. <https://doi.org/10.1029/2018GL078093>
- Sawyer, R. P., Fuselier, S. A., Mukherjee, J., & Petrinen, S. M. (2019). An investigation of flow shear and diamagnetic drift effects on magnetic reconnection at Saturn's dawnside magnetopause. *Journal of Geophysical Research: Space Physics*, *124*, 8457–8473. <https://doi.org/10.1002/2015JA026696>
- Smith, A. W., Jackman, C. M., & Thomsen, M. F. (2016). Magnetic reconnection in Saturn's magnetotail: A comprehensive magnetic field survey. *Journal of Geophysical Research: Space Physics*, *121*, 2984–3005. <https://doi.org/10.1002/2015JA022005>
- Smith, A. W., Jackman, C. M., Thomsen, M. F., Sergis, N., Mitchell, D. G., & Roussos, E. (2018). Dipolarization fronts with associated energized electrons in Saturn's magnetotail. *Journal of Geophysical Research: Space Physics*, *123*, 2714–2735. <https://doi.org/10.1002/2017JA024904>
- Tao, C., Kataoka, R., Fukunishi, H., Takahashi, Y., & Yokoyama, T. (2005). Magnetic field variations in the Jovian magnetotail induced by solar wind dynamic pressure enhancements. *Journal of Geophysical Research*, *110*, A11208. <https://doi.org/10.1029/2004JA010959>
- Thomsen, M. F., & Coates, A. J. (2019). Saturn's plasmopause: Signature of magnetospheric dynamics. *Journal of Geophysical Research: Space Physics*, *124*, 8804–8813. <https://doi.org/10.1002/2015JA027075>
- Thomsen, M. F., Jackman, C. M., Cowley, S. W. H., Jia, X., Kivelson, M. G., & Provan, G. (2017). Evidence for periodic variations in the thickness of Saturn's nightside plasma sheet. *Journal of Geophysical Research: Space Physics*, *122*, 280–292. <https://doi.org/10.1029/2016JA023368>
- Thomsen, M. F., Jackman, C. M., Mitchell, D. G., Hospodarsky, G., Kurth, W. S., & Hansen, K. C. (2015). Sustained lobe reconnection in Saturn's magnetotail. *Journal of Geophysical Research: Space Physics*, *120*, 10,257–10,274. <https://doi.org/10.1002/2015JA021768>
- Thomsen, M. F., Jackman, C. M., Tokar, R. L., & Wilson, R. J. (2014). Plasma flows Saturn's nightside magnetosphere. *Journal of Geophysical Research: Space Physics*, *119*, 4521–4535. <https://doi.org/10.1002/2014JA019912>
- Thomsen, M. F., Wilson, R. J., Tokar, R. L., Reisenfeld, D. B., & Jackman, C. M. (2013). Cassini/CAPS observations of duskside tail dynamics at Saturn. *Journal of Geophysical Research: Space Physics*, *118*, 5767–5781. <https://doi.org/10.1002/jgra.50552>
- Treumann, R. A. (2006). The electron-cyclotron maser for astrophysical application. *The Astronomy and Astrophysics Review*, *13*, 229–315. <https://doi.org/10.1007/s00159-006-0001-y>
- Vasyliunas, V. M. (1983). Plasma distribution and flow. In Dessler, A. J. (Ed.), *Physics of the Jovian Magnetosphere* (pp. 395–453). New York: Cambridge University Press.
- Yao, Z. H., Grodent, D., Ray, L. C., Rae, I. J., Coates, A. J., Pu, Z. Y., et al. (2017). Two fundamentally different drivers of dipolarizations at Saturn. *Journal of Geophysical Research: Space Physics*, *122*, 4348–4356. <https://doi.org/10.1002/2017JA024060>
- Zieger, B., & Hansen, K. C. (2008). Statistical validation of a solar wind propagation model from 1 to 10 AU. *Journal of Geophysical Research*, *113*, A08107. <https://doi.org/10.1029/2008JA013046>